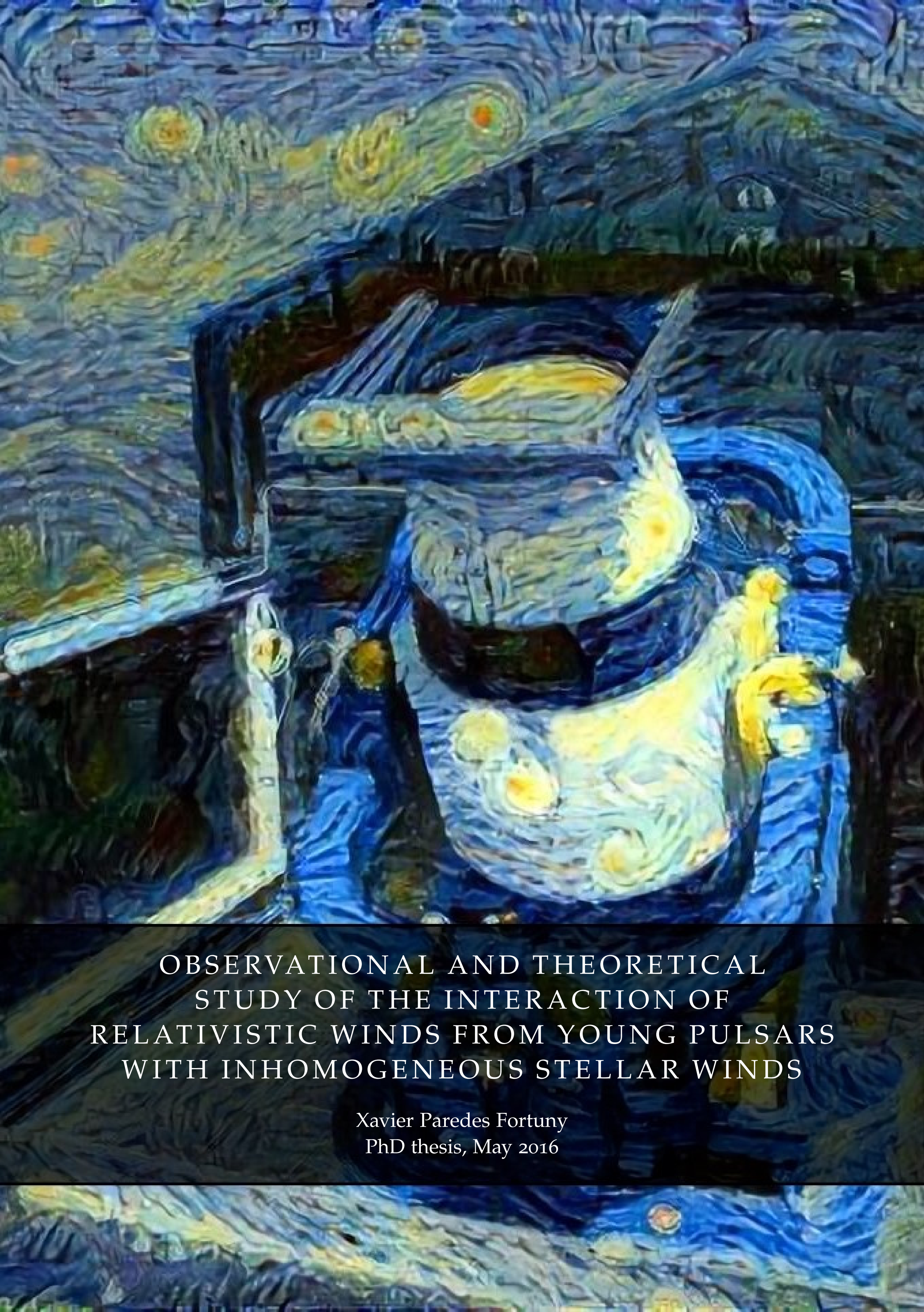

OBSERVATIONAL AND THEORETICAL STUDY OF THE INTERACTION OF RELATIVISTIC WINDS FROM YOUNG PULSARS WITH INHOMOGENEOUS STELLAR WINDS

Xavier Paredes Fortuny
PhD thesis, May 2016

UNIVERSITAT DE
BARCELONA

OBSERVATIONAL AND THEORETICAL STUDY OF THE INTERACTION OF RELATIVISTIC WINDS FROM YOUNG PULSARS WITH INHOMOGENEOUS STELLAR WINDS

XAVIER PAREDES FORTUNY

PhD thesis

Barcelona, May 2016

PROGRAMA DE DOCTORAT EN FÍSICA
LÍNIA DE RECERCA EN ASTRONOMIA I ASTROFÍSICA
2012–2016

Tesi doctoral presentada per **Xavier Paredes Fortuny**
per optar al títol de doctor per la Universitat de Barcelona

DIRECTORS
Dr. Marc Ribó Gomis
Dr. Valentí Bosch Ramon

TUTOR
Dr. Marc Ribó Gomis

Xavier Paredes Fortuny: *Observational and theoretical study of the interaction of relativistic winds from young pulsars with inhomogeneous stellar winds*, PhD thesis, May 2016

Front cover illustration: Deep Dream image generated by `https://dreamscopeapp.com` using an image of the Vincent van Gogh painting *The Starry Night*, and an picture of the Telescope Fabra-ROA Montsec (TFRM; from `http://www.am.ub.edu/bnc/`). The TFRM is the telescoped used to conduct the photometric observations presented in this thesis.

Back cover illustration: Deep Dream image created using an image of the Vincent van Gogh painting *The Starry Night*, and a photograph of the Heart and Soul nebulas made by Leonardo Orazi (from `http://apod.nasa.gov/apod/ap140211.html`). The gamma-ray binary LS I +61 303 studied in this thesis is located in the same field of view.

Als meus pares i a Miriam

AGRAÏMENTS

Primer de tot voldria agrair als meus directors de tesi, els doctors Marc Ribó Gomis i Valentí Bosch Ramon, el seu esforç, dedicació i tracte personal en la direcció de la present tesi doctoral. A més, el seu raonament científic i pensament crític han contribuït tant en el meu creixement professional com personal, sent molt valuosos i aplicables en molts àmbits.

També voldria agrair als col·laboradors Dr. Manel Perucho Pla i al Dr. Dmitry Khangulyan el seu ensenyament durant les estades de recerca, i sobretot, la càlida acollida. Així mateix, voldria agrair a tot l'equip que opera el TFRM, en especial al Daniel del Ser, tot el treball realitzat per a poder dur a terme les observacions i la seva gran ajuda. Tanmateix voldria agrair la molt bona feina feta per la secretaria del DAM, en especial al J.R., sense vosaltres tot hauria estat molt més difícil.

També, voldria agrair a tots aquells que m'han donat suport i han fet d'aquest camí, un camí molt agradable. Destacant, a tots els companys i amics del DAM per tots els bons moments que hem passat junts. Als amics de tota la vida, en especial al Sergio, per totes les experiències compartides. I a la Marisol i al Pepe pel seu suport i per fer-me un més de la família, mostrant-me la seva meravellosa forma de ser.

També, voldria agrair als meus pares, a qui els hi dedico la tesi, el fet haver-m'ho donat tot, sense la vostra estima, educació, paciència i suport no seria la mateixa persona que sóc ara i mai hagués arribat fins aquí. Tampoc res d'això hauria estat possible, si no fos pels meus germans, David i Laura, qui han estat un referent i una peça molt important a la meva vida.

Finalment, però no menys important, voldria agrair a Miriam, el meu amor des de fa més de 8 anys i a qui també dedico aquesta tesi, la seva paciència i el seu suport incondicional i qui amb la seva alegria em recorda cada dia quines són les coses importants de la vida.

A tots i totes, gràcies.

RESUM

L'astrofísica d'altes energies estudia els processos més energètics que es donen a l'Univers, els quals originen els raigs gamma (>500 keV). Els raigs gamma plantegen un repte observacional, ja que aquests són absorbits per l'atmosfera i només els més energètics de tots poden ser observats directament des de la Terra, la resta cal observar-los o bé indirectament amb els anomenats telescopis Cherenkov o bé directament mitjançant satèl·lits espacials. Hi ha molts objectes astronòmics diferents que emeten raigs gamma, per exemple: romanents de supernova, nebuloses de vent de púlsar, galàxies de nucli actiu i estrelles binàries de raigs gamma. La present tesi doctoral estudia aquesta darrera classe.

Les estrelles binàries de raigs gamma són sistemes binaris que contenen un objecte compacte que orbita a una estrella, on el seu màxim d'emissió no tèrmic està situat als raigs gamma. Actualment coneixem 5 binàries de raigs gamma: PSR B1259−63, LS I +61 303, LS 5039, HESS J0632+057 i 1FGL J1018.6−5856. Totes elles contenen una estrella de tipus primerenc i un objecte compacte de natura desconeguda, ja sigui un forat negre o una estrella de neutrons, excepte per la binària PSR B1259−63, on s'han detectat pulsacions ràdio. Les binàries de raigs gamma constitueixen laboratoris únics per estudiar els processos de més alta energia, ja que en ser sistemes binaris, moltes de les seves propietats es troben modulades amb el període orbital. Aquesta periodicitat permet abordar l'estudi d'aquests objectes de manera sistemàtica, realitzant-ne per exemple, campanyes multi-longitud d'ona. A més, les binàries de raigs gamma, no només són objectes enigmàtics amb moltes preguntes sense resposta, sinó que també mostren esdeveniments inesperats per la comunitat científica que fan del seu estudi un repte molt interessant.

En el context de les estrelles binàries de raigs gamma, la present tesi doctoral estudia la interacció de vents relativistes, provinents de púlsars,

amb entorns estel·lars. Aquests estudis s'han dut a terme tant de manera observacional com de manera teòrica.

Els estudis observacionals presentats en aquesta tesi s'han fet a través d'observacions òptiques. Aquestes inclouen observacions fotomètriques i l'estudi de mesures de l'amplada equivalent de la línia Hα. L'emissió òptica del sistema binari és produïda per l'estrella massiva i pel seu entorn estel·lar. Si l'estrella massiva és una estrella del tipus Be, llavors aquesta presenta un disc equatorial (fruit de la seva ràpida velocitat de rotació), sent la mida d'aquest traçada per l'amplada equivalent de la línia Hα. Simulacions numèriques d'estrelles binàries de raigs gamma on l'estrella massiva és del tipus Be, mostren com el disc equatorial és destruït durant el pas pel periastre de l'objecte compacte, ja sigui per la seva atracció gravitatòria i/o pel seu vent relativista (si l'objecte compacte fos un púlsar). S'estima que per la binària de raigs gamma LS I +61 303 la contribució del disc equatorial a l'emissió fotomètrica de l'estrella representa 1/3 de l'emissió total. Per tant, sota la hipòtesi que el disc és òpticament gruixut, el flux fotomètric és proporcional a l'àrea projectada del disc. Així doncs, qualsevol variabilitat orbital observada en les corbes de llum òptiques, pot ser atribuïda a canvis en el disc equatorial de l'estrella. En la present tesi doctoral hem realitzat observacions òptiques de l'estrella binària de raigs gamma LS I +61 303.

LS I +61 303 és una estrella binària de raigs gamma situada a la nostra Galàxia i a una distància de $\sim$ 2 kpc. El sistema binari està format per una estrella òptica ($V \sim 10.7$ mag) del tipus Be i un objecte compacte, el qual pot ser una estrella de neutrons o un forat negre. Tot i que actualment, l'escenari físic més acceptat per aquest sistema binari conté un púlsar. Independentment de l'escenari físic, l'objecte compacte es troba orbitant en una òrbita molt excèntrica amb un període orbital de $\sim$ 26 dies. La modulació del flux, sincrontizada amb el període orbital, ha estat detectada des de radio fins a raigs gamma molt energètics. A més de la variabilitat orbital, el sistema binari LS I +61 303 presenta una variabilitat a llarg termini en l'amplitud i la fase orbital del màxim d'emissió en ràdio. Aquesta variabilitat és periòdica, amb un període de $\sim$ 4.6 anys i és coneguda com a variabilitat super-orbital. La variabilitat super-orbital ha estat detectada en totes les longituds d'ona. La detecció d'aquesta variabilitat en mesures de l'amplada equivalent de la línia Hα indiquen que aquesta podria estar relacionada amb canvis de les propietats del disc equatorial de l'estrella, afectant així l'emissió òpica del sistema. En la present tesi doctoral hem fet un seguiment òptic de la binària de raigs gamma LS I +61 303 per tal d'estudiar-ne la seva variabilitat orbital i super-orbital. Les observacions fotomètriques s'han realitzat amb el Telescopi Fabra-ROA Montsec (TFRM) i les observacions espectroscòpiques amb el telescopi Liverpool.

Els resultats que hem obtingut de les observacions òptiques mostren el descobriment de la variabilitat super-orbital en la fase orbital del màxim de l'emissió òptica, sent aquest una evidència de l'acoblament dels processos d'emissió tèrmics i no tèrmics a l'estrella binària LS I +61 303. L'observació de la variabilitat super-orbital de la fase orbital del màxim permet, donada una fase super-orbital, realitzar una comparació multilongitud de la fase del màxim d'emissió. També s'ha mostrat per primera vegada la variabilitat super-orbital del flux fotomètric compatible amb el període de $\sim$ 4.6 anys. I s'ha confirmat el mateix efecte, ja conegut, per l'amplada equivalent de la línia Hα. Per primer vegada, s'ha realitzat un estudi de la variabilitat super-orbital de l'emissió òptica per diferents rangs de fase orbital. Aquest estudi ha mostrat que hi ha rangs de fase orbital on no s'observa la variabilitat super-orbital o bé aquesta és atenuada. Les observacions òptiques semblen requerir un disc estès i coplanar amb el pla de l'òrbita. A més, recolzen el model d'ona de densitat per explicar la variabilitat super-orbital en l'òptic i fan poc plausible un model de precessió del disc.

Els estudis teòrics de binàries de raigs gamma presentats en aquesta tesi s'han realitzat a través de simulacions hidrodinàmiques relativistes. Les estrelles binàries de raigs gamma que contenen un púlsar jove i una estrella massiva, presenten una interacció molt forta entre el vent relativista del púlsar i el vent de l'estrella companya. Aquesta interacció produeix acceleració de partícules i radiació no tèrmica, des d'ones de ràdio fins a raigs gamma. A més, la regió on es produeix aquesta interacció es pot veure afectada per l'impacte d'un vent estel·lar heterogeni. Aquest impacte altera la dinàmica del sistema i la radiació produïda. En la present tesi doctoral hem realitzat simulacions hidrodinàmiques relativistes axisimètriques de la interacció de vents relativistes provinents de púlsars joves amb vents estel·lars heterogenis, centrant-nos en la regió més interna del sistema binari. El vent heterogeni s'ha caracteritzat per una regió circular amb una determinada densitat i situada a l'eix que uneix les dues estrelles. S'ha estudiat l'impacte per diferents graus d'heterogeneïtat a través de diferents radis i densitats.

Els resultats de les simulacions mostren que l'arribada d'aquest vent heterogeni té un gran impacte sobre tota la regió d'interacció. Per tant, s'espera que aquesta pertorbació afecti a l'emissió no tèrmica del sistema. Els resultat confirmen la sensibilitat de la regió d'interacció sota l'impacte d'un vent heterogeni. A més, els resultats mostren que aquest vent causa fortes inestabilitats del tipus Rayleigh-Taylor/Kelvin-Helmholtz, provocant canvis ràpids en el vent xocat del púlsar. Els resultats també mostren l'efecte de l'impacte per diferent graus d'heterogeneïtat del vent estel·lar (en termes de mida i densitat). Els resultats obtinguts podrien explicar la variabilitat observada en les corbes de llum d'algunes binàries de raigs gamma.

CONTENTS

1 INTRODUCTION 1
1.1 Gamma-ray astrophysics 1
1.2 Gamma-ray binaries 3
1.3 Motivation and overview of this thesis 7

I OPTICAL OBSERVATIONS OF GAMMA-RAY BINARIES 11

2 OBSERVATIONAL TECHNIQUES AND INSTRUMENTATION 13
2.1 Photometric observations 13
2.2 $EW_{\mathrm{H}\alpha}$ observations 16

3 A DATA REDUCTION AND ANALYSIS PIPELINE FOR DIFFERENTIAL PHOTOMETRY 19
3.1 Image calibration 19
3.2 Photometric calibration 23
3.3 Plotting 26

4 LONG-TERM OPTICAL OBSERVATIONS OF THE GAMMA-RAY BINARY LS I +61 303 29
4.1 Introduction 29
4.2 Observations and data reduction 31
4.3 Results 33
4.4 Discussion 48
  4.4.1 On the orbital variability 49
  4.4.2 On the superorbital variability 50
4.5 Conclusions 57

II RELATIVISTIC HYDRODYNAMICS 61

5 RELATIVISTIC HYDRODYNAMICAL SIMULATIONS 63
5.1 Fluid Dynamics 63
5.2 Relativistic Fluid Dynamics 65
5.3 The numerical code 67

6 SIMULATIONS OF THE INTERACTION OF RELATIVISTIC PULSAR WINDS WITH INHOMOGENEOUS STELLAR WINDS 69
- 6.1 Introduction 69
- 6.2 Physical framework 72
- 6.3 Numerical simulations 75
  - 6.3.1 Numerical set-up 75
  - 6.3.2 Results 79
- 6.4 Discussion 95
  - 6.4.1 Numerical results vs analytical estimates 96
  - 6.4.2 Clump effects on the global structure and radiation 97
  - 6.4.3 Future work 99
- 6.5 Conclusions 99

7 HYDRODYNAMICAL STREAMLINE COMPUTATION 101
- 7.1 Streamline calculation 102
- 7.2 Streamlines of the interaction of relativistic pulsar winds with inhomogeneous stellar winds 103

III CONCLUDING REMARKS 107

8 CONCLUDING REMARKS OF THE THESIS 109
- 8.1 Concluding remarks of Part I 109
- 8.2 Concluding remarks of Part II 111

IV APPENDIX 113

A OTHER OBSERVATIONAL RESULTS 115
- A.1 MWC 656 115
- A.2 MWC 148 117
- A.3 TYC 4051-1277-1 and TYC 3594-2269-1 118
- A.4 PSR J1023+0038 120

B SIMULATIONS OF A RELATIVISTIC JET 121
- B.1 Simulations of a jet-stellar wind interaction 121
  - B.1.1 Numerical set-up 121
  - B.1.2 Streamline calculations 123
  - B.1.3 Results 124
- B.2 Simulations of a jet-obstacle interaction 126

B.2.1 Numerical set-up 126
B.2.2 Streamline calculations 127
B.2.3 Results 127

PUBLICATIONS 129

LIST OF FIGURES 131

LIST OF TABLES 135

ACRONYMS 137

BIBLIOGRAPHY 139

1

INTRODUCTION

This PhD thesis is focused on the field of gamma-ray astrophysics, particularly on the study of the interaction of pulsar winds with stellar environments in gamma-ray binaries. This is conducted through optical observations and numerical simulations.

In this chapter we shortly introduce gamma-ray astrophysics (Section 1.1), gamma-ray binaries (Section 1.2), and finally, at the end of this chapter, we provide the motivation and overview of this thesis (Section 1.3).

1.1 GAMMA-RAY ASTROPHYSICS

Gamma-ray astrophysics studies the physical properties of astronomical objects that display gamma-ray emission, the most energetic part of the electromagnetic spectrum with photon energies greater than 500 keV ($\lambda \leqslant 0.002$ nm). Gamma-ray emission does not have a thermal origin, therefore requires of particle acceleration and non-thermal processes. Gamma-ray observations are very challenging due to the absorption/scattering of the high-energy photons by the atmosphere. Therefore, the direct observation is done with space satellites, whereas the indirect observations are conducted by ground based telescopes/detectors (see, e.g., Longair 2011).

Currently, there are two active space satellites sensitive to High Energy (HE) gamma rays (above 100 MeV): the *Fermi Gamma-ray Space Telescope* (*Fermi*), and the *Astro-Rivelatore Gamma a Immagini LEggero* (*AGILE*). The

Fermi satellite was launched in 2008 with the main instrument onboard called Large Area Telescope (LAT), which is an imaging pair conversion gamma-ray telescope working in the energy range between 20 MeV and 300 GeV that scans the whole sky every 3 hours. The instrument has an angular resolution of 3.5° at 100 MeV and $< 0.15°$ above 10 GeV (see Atwood et al. 2009). The *AGILE* satellite was launched in 2007 carrying a gamma-ray detector sensitive to photons with energies between 30 MeV and 50 GeV. The angular resolution is better than 0.5° for energies above 1 GeV (see Tavani et al. 2009). The main drawback of space satellites is the small collecting area, resulting in a very small photon flux for Very High Energy (VHE) gamma rays (> 100 GeV).

The most energetic high-energy photons initiate electromagnetic cascades at the upper layers of the atmosphere, known as extensive air showers, due to electron-positron pair production. The particles produced in these extensive air showers can be observed at ground level with detectors like The High-Altitude Water Cherenkov Observatory (HAWC), while the Cherenkov light produced in the cascade can be observed with Imaging Atmospheric Cherenkov Telescopes (IACTs), like the High Energy Stereoscopic System (H.E.S.S.), the Major Atmospheric Gamma Imaging Cherenkov Telescopes (MAGIC), and the Very Energetic Radiation Imaging Telescope Array System (VERITAS), or the forthcoming Cherenkov Telescope Array (CTA). HAWC is designed to perform a survey of the sky for gamma rays and cosmic rays at energies between 100 GeV and 100 TeV, due to the large collecting area and its big Field of View (FOV), which covers a 15% of the sky (Abeysekara et al. 2013). On the other hand, IACTs are used to study specific sources due to their pointing capabilities. The current IACTs facilities work in an energy range from ~ 50 GeV to ~ 50 TeV and have an angular resolution of ~ 0.1 deg (e.g., Rieger et al. 2013).

There are many classes of gamma-ray sources, like Supernova Remnants (SNR), Pulsar Wind Nebulae (PWN), Active Galactic Nuclei (AGN), gamma-ray binaries, etcetera. In this work we will focus on gamma-ray binaries. In Fig. 1.1 we show an all-sky image for energies above 1 GeV based on five years of data from *Fermi*-LAT, and in Fig. 1.2

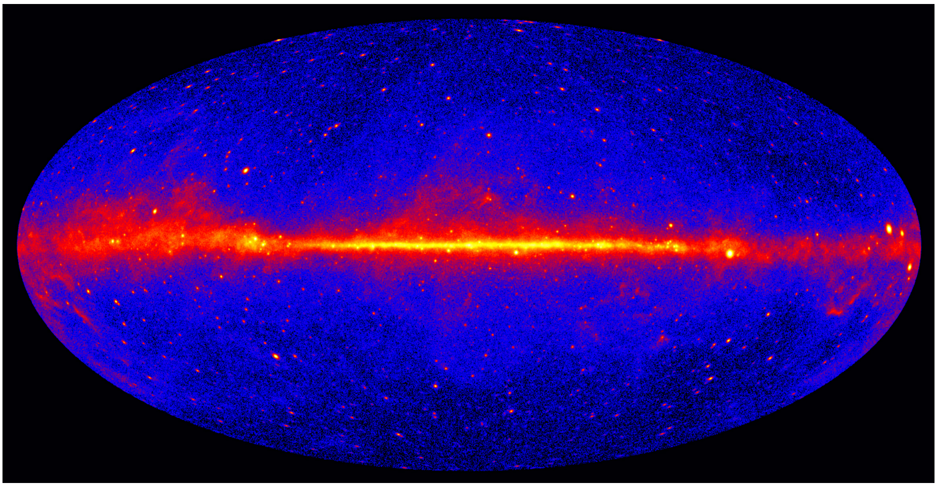

Figure 1.1: All-sky image based on five years of data from the *Fermi*-LAT at energies greater than 1 GeV. Image credit: NASA/DOE/*Fermi* LAT Collaboration.

we show an all-sky image with the current catalog of VHE sources detected by IACTs.

1.2 GAMMA-RAY BINARIES

Gamma-ray binaries are systems that comprise a compact object orbiting a companion star and have the maximum of the non-thermal Spectral Energy Distribution in gamma rays. Currently we know five gamma-ray binaries: PSR B1259−63, LS I +61 303, LS 5039, HESS J0632+057, and 1FGL J1018.6−5856 (see Dubus 2013 and references therein). All of them host an early type star and a compact object of unknown nature, either a black hole or a neutron star, except for the binary system PSR B1259−63, where radio pulsations have been detected. VLBI observations show extended, and elongated, cometary tail-like morphologies in some of these objects, hinting that the compact object might be a pulsar (Moldón 2012). LS 5039 and 1FGL J1018.6−5856 host an O6 star, while LS I +61 303, HESS J0632+057, and PSR B1259−63 host a Be star.

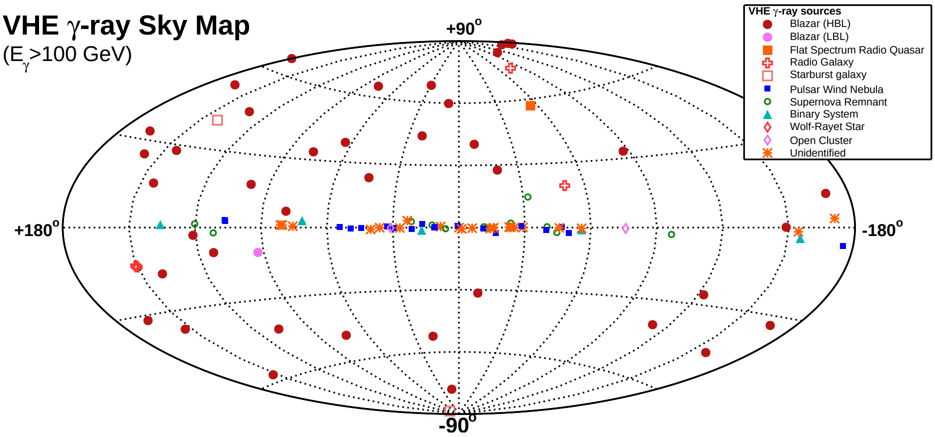
VHE γ-ray Sky Map
(E_γ>100 GeV)
+90°
-90°
+180°
-180°
VHE γ-ray sources
Blazar (HBL)
Blazar (LBL)
Flat Spectrum Radio Quasar
Radio Galaxy
Starburst galaxy
Pulsar Wind Nebula
Supernova Remnant
Binary System
Wolf-Rayet Star
Open Cluster
Unidentified

Figure 1.2: All-sky map of VHE sources detected by IACTs. Obtained from: `https://www.mppmu.mpg.de/~rwagner/sources/`.

Be stars are non-supergiant fast-rotating early type stars that at some point have shown emission lines (see Rivinius et al. 2013 and references therein). The five gamma-ray binaries are located at distances between 1.5 and 5 kpc. The orbital periods range from ~ 4 days for the binary LS 5039 up to ~ 3.4 years for the system PSR B1259−63, and the eccentricities range from 0.35 up to 0.87, respectively, resulting in very different periastron-apastron distance ratios. The X-ray, GeV, and TeV fluxes are modulated with the orbital period. The physical properties of the five gamma-ray binaries are summarized in Table 1.1; see also Dubus (2013); Paredes et al. (2013); and references therein.

Currently, there are two proposed physical scenarios to explain the multi-wavelength emission from gamma-ray binaries: the microquasar scenario and the pulsar wind scenario (Mirabel 2012). In the microquasar scenario, the compact object is either a black hole or a neutron star accreting matter from the companion star and displaying relativistic jets. In the pulsar-wind scenario, the compact object is a young non-accreting pulsar that presents a powerful relativistic wind. In both scenarios, the massive stellar companion provides a huge optical/UV photon field, and we find the proper environment for particle acceleration (magnetized plas-

Table 1.1: System parameters of gamma-ray binaries. Adapted from Dubus (2013). Parameters marked with * are from Casares et al. (2005).

	PSR B1259−63	LS 5039	LS I +61 303	HESS J0632+057	1FGL J1018.6−5856
P_{orb} (days)	1236.72432(2)	3.90603(8)	26.496(3)	315(5)	16.58(2)
e	0.8698872(9)	0.35(3)	0.72^*	0.83(8)	-
ω (°)	$138.6659(1)^\sharp$	212(5)	21^*	129(17)	-
i (°)	19–31	13–64	10–60	47–80	-
d (kpc)	2.3(4)	2.9(8)	2.0(2)	1.6(2)	5.4
spectral type	O9.5Ve	O6.5V((f))	B0Ve	B0Vpe	O6V((f))
$M_\star$ ($M_\odot$)	31	23	12	16	31
$R_\star$ ($R_\odot$)	9.2	9.3	10	8	10.1
$T_\star$ (K)	33500	39000	22500	30000	38900
$d_{periastron}$ (AU)	0.94	0.09	0.19	0.40	(0.41)
$d_{apastron}$ (AU)	13.4	0.19	0.64	4.35	(0.41)
$\phi_{periastron}$	0	0	0.23^*	0.967	-
$\phi_{sup.\ conj.}$	0.995	0.080	0.16^*	0.063	-
$\phi_{inf.\ conj.}$	0.048	0.769	0.26^*	0.961	-

mas, high density contrast, relativistic motion, shocks, and turbulence), and non-thermal processes (synchrotron and Inverse Compton -IC- for electrons, and mostly proton-proton interactions for hadrons); see Bosch-Ramon & Khangulyan (2009); Dubus (2013); and references therein.

The radio emission of gamma-ray binaries is produced by synchrotron radiation of low-energy electrons, which in all cases except LS 5039 is orbitally modulated. Free-free absorption prevents the detection of radio emission from the inner parts of the binary system. Therefore, the radio emission traces the non-thermal emission from regions outside the binary system.

The X-ray emission of gamma-ray binaries (Anderhub et al. 2009; Takahashi et al. 2009; Zabalza et al. 2011) is generally thought to be produced by synchrotron radiation of high-energy and very high-energy electrons, and in all cases is orbitally modulated. This variability can be interpreted as due to a variable particle injection rate and/or radiative and non-radiative energy losses. X-rays trace the non-thermal emission from the inner regions of the binary system.

The HE and VHE emission of gamma-ray binaries is modulated with the orbital period. However, the HE and VHE emission maxima do not occur at the same orbital phase. The orbital modulation in both energy bands can be understood to first order by anisotropic IC scattering of stellar optical/UV photons by relativistic electrons, and $\gamma\gamma$ absorption of gamma rays in the photon field of the stellar companion. The luminosity associated with the scattered photons by IC depends on the angle between the original optical/UV photon and electron directions of motion, being this luminosity maximum for head-on collisions. Therefore, assuming that there are accelerated electrons close to the compact object, the maximum in the IC emission is expected around superior conjunction of the compact object. The $\gamma\gamma$ absorption occurs when a gamma-ray photon interacts with a stellar photon and produces an electron-positron pair. Considering the spectral energy distribution of massive stars, in gamma-ray binaries $\gamma\gamma$ absorption takes place basically for VHE photons. This absorption is stronger for a larger stellar photon density (i.e., at those phases where the pulsar is close to the star) and for photon-photon head-on collisions (i.e., at superior conjunction). This mechanism suppresses the VHE emission around the superior conjunction if the orbital inclination is significant, provided that IC cascading is not important. The combination of these two processes, anisotropic IC and $\gamma\gamma$ absorption, together with the particularities of each system (e.g., orbit configuration), have a strong impact on the HE and VHE light curves of gamma-ray binaries (see Bosch-Ramon & Khangulyan 2009; Dubus 2013 and references therein). For instance, in the gamma-ray binary LS 5039, the HE and VHE modulations are anti-correlated, being the maxima of the HE and the VHE emission at the superior and inferior conjunctions, respectively. However, in the case of LS I +61 303, the anisotropic IC and $\gamma\gamma$ absorption are not sufficient to explain the HE and VHE light curves. It is worth noting that these mechanisms characterizing the gamma-ray emission in gamma-ray binaries are independent of the nature of the compact object and the related possible emission scenarios.

In this thesis we study gamma-ray binaries through optical observations and numerical simulations in the pulsar-wind scenario context.

1.3 MOTIVATION AND OVERVIEW OF THIS THESIS

High-energy astrophysics studies the most energetic and interesting[1] processes in the Universe. Despite the violent interactions present in high-energy sources, sometimes the results from these interactions do not evolve on human time-scales, being the corresponding astronomical observations a (scientifically worthy) snap-shot from a (human)-static event. Or the opposite, the events occur so fast that one can not observe them properly, or worse, the phenomenon is not only rapid but also unique and one can not conduct systematic studies on that. However, gamma-ray binaries constitute unique laboratories; with some of their properties modulated with the orbital period (on human time-scales), they allow a systematic multi-wavelength observational approach. Of course, gamma-ray binaries also present unique (and unexpected) phenomena, and lots of open questions. All of these make the study of gamma-ray binaries a very challenging and interesting scientific case.

---

[1] Personal opinion from the author.

The current knowledge of gamma-ray binaries is incomplete, and many open questions remain. There are general questions: For example, which is the physical scenario of these systems? Do all gamma-ray binaries share the same physical scenario, or can the observed gamma-ray emission arise from different types of objects? There are also source-dependent questions, such as: What is the origin of the observed multi-wavelength superorbital variability in the gamma-ray binary LS I +61 303? What causes the unexpected periodic gamma-ray flare in the gamma-ray binary PSR B1259−63? What causes the fast flares seen in the X-ray light curves of some gamma-ray binaries? What are the physical parameters of these systems? In this thesis, we address some of these questions, both observationally and theoretically, and extend the current scientific knowledge of these systems.

The observational studies of gamma-ray binaries presented in this thesis have been conducted through optical observations. The optical emission received from gamma-ray binaries is produced by the optical star and its environment. If the optical star is a Be star, then it presents a circumstellar decretion disk, being its size traced by the Equivalent Width of the Hα line ($EW_{\mathrm{H}\alpha}$) (e.g., Negueruela et al. 1998). Numerical simulations of gamma-ray binaries hosting a Be star (Takata et al. 2012; Okazaki et al. 2011) suggest that the circumstellar decretion disk is perturbed/disrupted during the periastron passage of the compact object by the tidal forces and/or the putative pulsar wind. The circumstellar disk contribution to the optical photometry is a significant fraction of the total optical emission ($\sim 1/3$ for the gamma-ray binary LS I +61 303, according to Casares et al. 2005). Under the assumption that the circumstellar disk is optically thick, the observed optical photometric flux from it will be proportional to the projected area of the corresponding emitting region of the disk. Therefore, any orbital variability in the optical light curves can be associated to changes in the circumstellar disk (e.g., Zamanov et al. 2014). We conducted long-term optical (photometric and $EW_{\mathrm{H}\alpha}$) observations of the gamma-ray binary LS I +61 303, aimed to unveil the optical superorbital variability seen at other wavelengths, and interpret the results in the pulsar-wind scenario context.

The optical observations are presented in Part I (Chapters 2, 3, and 4). In Chapter 2 we provide a short introduction on the observational techniques, the photometry (Section 2.1), and the $EW_{\mathrm{H}\alpha}$ (Section 2.2), and optical facilities used in this thesis. In Chapter 3 we describe the pipeline developed to reduce and analyze, in an efficient and systematic fashion, the thousands of images produced by long-term optical photometric campaigns. Finally, in Chapter 4 we present the long-term optical observations of the gamma-ray binary LS I +61 303. In Appendix A we present other observational results obtained in the context of this thesis. It is worth to mention that we have initiated many observational campaigns apart from the monitoring of the gamma-ray binary LS I +61 303.

The theoretical studies of gamma-ray binaries presented in this thesis have been conducted through Relativistic Hydrodynamics (RHD) simulations. Gamma-ray binaries hosting a massive star and a young non-accreting pulsar present strong interaction between the relativistic pulsar wind, and the wind of the stellar companion, resulting in efficient particle acceleration and in the production of non-thermal radiation, from radio to gamma rays. The study of the dynamical interaction between the winds can be conducted through numerical simulations, allowing a qualitative analysis of the radiative output of the system (e.g., Romero et al. 2007; Okazaki et al. 2011; Bosch-Ramon et al. 2012; more details on previous numerical works can be found in Chapter 6). Furthermore, the two-wind interaction region might suffer the impact of an inhomogeneous stellar wind, making its dynamics and hence its radiative output more complex. We conducted RHD simulations of the interaction of relativistic winds from young pulsars with inhomogeneous stellar winds aimed to provide a plausible framework for the high-energy variability observed in gamma-ray binaries.

The RHD simulations are presented in Part II (Chapters 5, 6, and 7). In Chapter 5 we provide a short theoretical background on the equations solved in the RHD simulations. In Chapter 6 we present the RHD simulations of the interaction of pulsar relativistic winds with inhomogeneous stellar winds. Finally, in Chapter 7 we describe how to extract the hydrodynamical information (i.e., streamline computation) to compute a more detailed account of the radiative output of the system. In

Appendix B we present the streamline calculations of the collision of the jet of an AGN with a stellar wind.

The concluding remarks of both parts of the thesis are presented in Part III (Chapter 8).

Part I

OPTICAL OBSERVATIONS OF GAMMA-RAY BINARIES

2

OBSERVATIONAL TECHNIQUES AND INSTRUMENTATION

The observational studies of gamma-ray binaries presented in this thesis, have been conducted through optical observations (see Chapter 4 and Appendix A). The main objective of this chapter is to provide a short introduction on the observational techniques and the optical facilities used in this thesis.

In Section 2.1 we explain the optical photometry technique, and the facility used to conduct the photometric observations, the Telescope Fabra-ROA Montsec (TFRM). In Section 2.2 we present a short summary on $EW_{\mathrm{H}\alpha}$ measurements, and the employed facility, the Liverpool Telescope (LT).

2.1 PHOTOMETRIC OBSERVATIONS

Optical telescopes collect the light, within a certain energy range, and focus it to the focal plane, where an instrument sensitive to the optical light is installed. Optical photometry is an observational technique aimed to measure the amount of light emitted from an astronomical source and received by the instrument within a certain energy range.

Currently, the most widely used instrument for high precision photometric measurements is the Charge-Coupled Device (CCD). The CCD is a two-dimensional detector which uses the photoelectric effect to convert the incident light into an electronic charge that can be measured. The number of counts measured at each pixel is proportional to the received amount of light (known as linearity effect). CCDs are very powerful because of their high sensitivity to the optical light, and their possibility of measuring many astronomical sources at the same time (crucial to conduct high precision differential photometry, see below).

There are some instrumental effects related with the CCD that need to be corrected: variability in the sensitivity from pixel to pixel, noise generated due to thermal agitation, noise produced during the readout, deviations from linearity at high intensities, and non-homogeneous exposure of the CCD caused by the finite shutter velocity. These effects can be corrected using the following calibration images: flats, darks, bias, linearity map, and shutter map, respectively. See next section for more details.

The CCD aperture photometry technique consists on estimating the received flux from an astronomical object, from the total number of counts inside a small circle or ellipse (called aperture) around the target. The aperture has to be small enough to avoid including light (counts) from other sources, but large enough to account for the largest possible percentage of the target flux. The instrumental magnitude measured from the n pixels inside a certain aperture region can be computed as

$$m^{\mathrm{inst}} = -2.5 \log_{10} \left[\frac{\sum_{i}^{n} (N_i - N_{\mathrm{sky}})}{t_{\mathrm{exp}}} \right] + C, \tag{2.1}$$

where N_i is the number of counts in pixel i, N_{sky} is the average number of sky background counts per pixel, t_{exp} is the exposure time of the CCD image, and C is an arbitrary constant.

The instrumental magnitude not only depends on the intrinsic properties of the source, but also depends on the telescope, the telescope site, the detector, the photometric aperture, the position of the astronomical object in the sky, the atmospheric extinction, the atmospheric conditions, and many other systematic effects. All of this results in the lack of a zero point for the instrumental magnitudes among different observations. Therefore a calibration method is required.

To obtain the calibrated magnitudes, the absolute photometry technique is needed. This technique consists on the observation of stars with well-known magnitudes, the photometric standard stars (e.g., Landolt (1992), aimed to correct the instrumental magnitudes from systematic effects. Due to the limited number of photometric stars, usually these stars are not in the same FOV as the target, requiring very good atmospheric conditions to properly model the airmass difference. However, in this thesis we are not interested in the absolute value of the target magnitude, but in the variability of the target magnitude along different nights. In this case, a differential photometry technique can be applied.

The simplest differential photometry method is to subtract from the target's instrumental magnitude, the magnitude of an intrinsically non-variable star located in the same FOV of the CCD. In the next chapter, we will present a more sophisticated differential photometry technique, but the underlying algorithm is the same. An intrinsically non-variable star (hereafter reference star), is a star which is intrinsically constant (at the needed precision and temporal scales). Therefore, any variability observed in a reference star is considered to be caused by instrumental or systematic effects. Because we also want to correct the atmospheric extinction (and other atmospheric effects), we are interested in those reference stars which are affected by the same (or similar) atmospheric layers than the target, therefore we are interested in those reference stars that are closer to the target.

After the magnitude difference has been computed, the resulting value is free of instrumental or systematic effects, and if we use the same reference star for all the images, the obtained magnitudes can be compared between them. Aimed to match the mean magnitude difference value with the tabulated value in the literature, an artificial offset value can be added to the magnitude differences. It is important to keep in mind that, when conducting differential photometry, we are obtaining the intrinsic variability of the source, but the magnitude zero point is artificial (unless absolute photometric observations are conducted).

The optical photometric observations presented in this thesis have been conducted with the robotic TFRM (see Fors et al. 2013; Fig. 2.1). The telescope is placed at the Observatori Astronòmic del Montsec (Lleida,

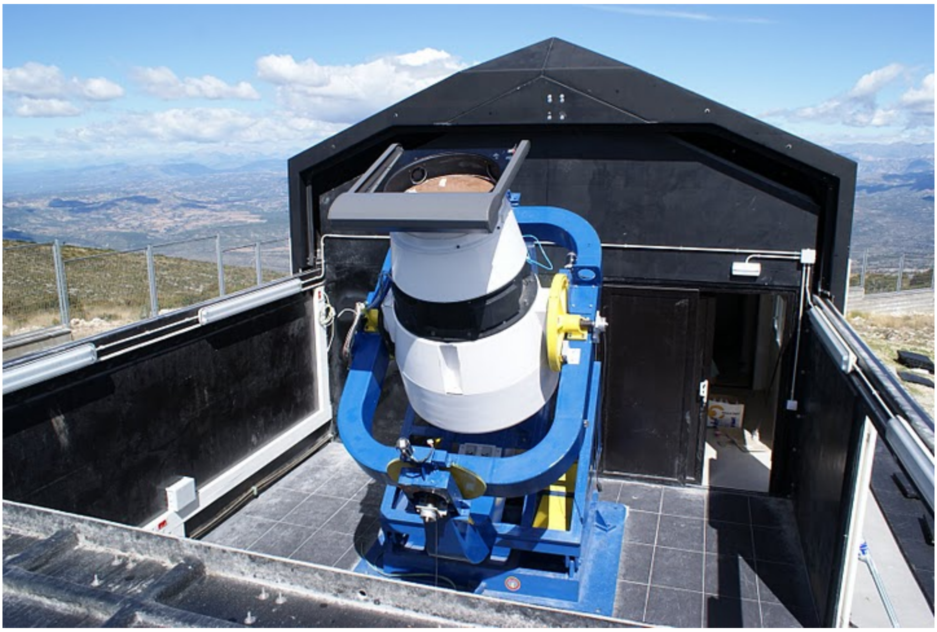

Figure 2.1: Telescope Fabra-ROA Montsec (TFRM). Image from: `http://www.am.ub.edu/bnc/`

Spain) at 1570 m above the mean sea level. The main specifications are: corrector plate of 0.5 m aperture and 0.78 m primary mirror, refurbished Baker-Nunn Camera for routine CCD robotic observations, focal ratio f/0.96, $4.4° \times 4.4°$ FOV with a pixel scale of $3.9''$/pixel, passband filter SCHOTT GG475 ($\lambda > 475$ nm.), and custom CCD based on FLI ProLine 16803 with quantum efficiency of 60% at 550 nm (Fors et al. 2013).

The data reduction and differential photometry have been conducted using a pipeline developed in the context of this thesis, the basics of which are described in Chapter 3.

2.2 $EW_{\mathrm{H}\alpha}$ OBSERVATIONS

When the light is absorbed (emitted) by an atom or molecule it produces an absorption (emission) line. These lines are called spectral lines and can be used to identify atoms and molecules present in stellar environments. A spectral lines presents an intensity profile as a function of the wavelength due to line broadening. The line can present a smaller (larger) intensity value with respect the continuum level, in that case we say that the line is in absorption (emission). The strength of the intensity profile can be characterized by the area enclosed between the line profile and the continuum level. The Equivalent Width (EW) is defined as the value in wavelength units, that multiplied by the continuum intensity value, results in the area enclosed by the line. Hence, the EW is a measure of the strength of the line.

The EW measurements presented in this thesis correspond to the ones of the Hα line ($EW_{\mathrm{H}\alpha}$). Hα is the spectral line of the transition between the third and the second energy level of the Hydrogen atom, being its wavelength of 656.3 nm (red part of the optical spectrum). The adopted convention in this thesis is positive EW for emission lines, and negative for absorption lines.

The $EW_{\mathrm{H}\alpha}$ measurements presented in this thesis have been obtained using FRODOspec on the robotic 2.0 m LT (see Fig. 2.2) at the Observatorio del Roque de los Muchachos (La Palma, Spain) placed at 2363 m above the mean sea level. The $EW_{\mathrm{H}\alpha}$ measurements have been obtained and analyzed by our collaborators in the same way as in Casares et al. (2012).

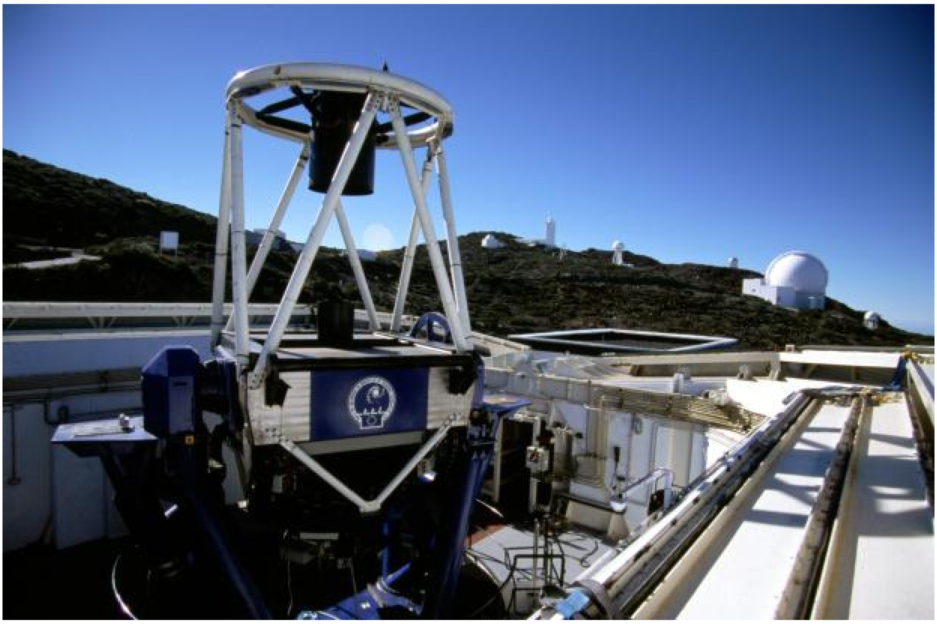

Figure 2.2: Liverpool Telescope. Image credit: Dr. Robert Smith, Liverpool John Moores University

3

A DATA REDUCTION AND ANALYSIS PIPELINE FOR DIFFERENTIAL PHOTOMETRY

The only way to reduce and analyze, efficiently and systematically, the thousands of raw images produced by long-term optical photometric observational campaigns, is to use an automatic pipeline. The main objective of this chapter is to provide an overview of all the steps, followed by the pipeline developed in the context of this work (~ 3000 lines), between data gathering and the final calibrated photometric measurements.

The astronomical images are obtained with the TFRM, and after being automatically retrieved (and visually inspected), are reduced and analyzed using an automatic pipeline, programmed in Python and named `Phot`[1], which has been developed by the author of this thesis. The data reduction and analysis process involves several steps (see Fig. 3.1), which can be grouped in three main blocks: image calibration (Section 3.1), photometric calibration (Section 3.2), and plotting (Section 3.3). These are described in the following sections.

3.1 IMAGE CALIBRATION

The astronomical images gathered from the telescope have to be processed before performing any photometric calibration.

Because we want to conduct differential photometry, we only need those reference stars that are closer to the target. The FOV of the TFRM is atypically large ($4.4° \times 4.4°$), therefore we can crop the image and

---

[1] The pipeline is available at `https://github.com/xparedesfortuny/Phot/`

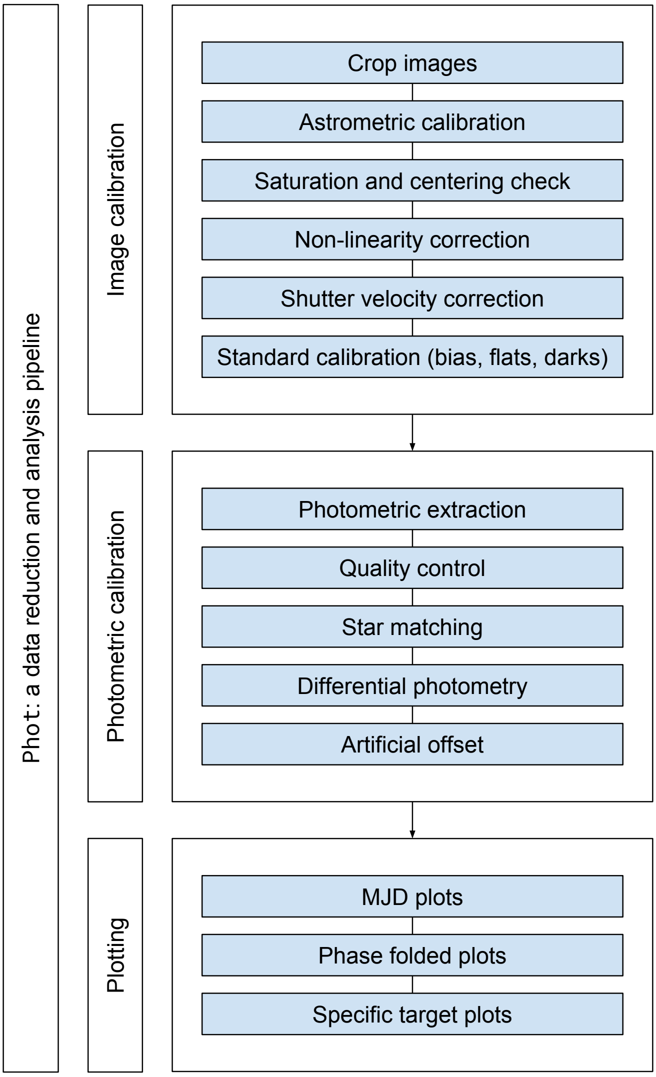
Phot: a data reduction and analysis pipeline
Image calibration
Crop images
Astrometric calibration
Saturation and centering check
Non-linearity correction
Shutter velocity correction
Standard calibration (bias, flats, darks)
Photometric calibration
Photometric extraction
Quality control
Star matching
Differential photometry
Artificial offset
Plotting
MJD plots
Phase folded plots
Specific target plots

Figure 3.1: Flowchart of `Phot`, the data reduction and analysis pipeline, used to analyze the photometric optical data from TFRM. The pipeline is available at `https://github.com/xparedesfortuny/Phot/`

keep a central region around our target, large enough to host many candidates for reference stars (1–2° radius depending on the field of stars around the target source). The cropping provides us with a faster computation time on the posterior calibration of the images, as well as a better astrometric accuracy.

The differential photometry technique applied to time-series requires the selection of the same set of reference stars among all the images (see Section 2.1). The physical coordinate system of the CCD, x and y, is not enough to provide a unique identification of the stars among different images and nights (different telescope pointing would lead to different star coordinates). Therefore an astrometric calibration of the images is required. The astrometric calibration consists on including the World Coordinate System (WCS) in the astronomical image, accounting for the transformations between the image physical coordinates and the sky coordinates. The pipeline performs the astronomical calibration using the `Astrometry.net` package (Lang et al. 2010). Once the astrometric calibration is finished, the pipeline is able to automatically locate the target in the image and conduct a saturation and centering check. The astrometric calibration is performed before the other calibration steps in order to save computing time if the image does not pass the saturation and centering checks.

The next step in the image calibration process is the non-linearity correction. The number of CCD pixel counts is proportional to the incident amount of light on that pixel for a wide range of light intensities (the so called linear regime of the CCD), but for a large number of counts (prior to saturation) the CCD deviates from linearity. Aimed to correct any minor deviation from linearity, a non-linearity correction is applied. The non-linearity correction is implemented in the pipeline using the following expression:

$$N_{corr}(x,y) = N(x,y) + b(x,y)\,N(x,y)^2 + c(x,y)\,N(x,y)^3, \qquad (3.1)$$

being $N_{corr}(x,y)$, and $N(x,y)$, the linearity-corrected number of counts, and the raw number of counts for a certain (x, y) pixel, respectively. The coefficients $b(x,y)$ and $c(x,y)$ are pixel dependent and are provided by the personnel from TFRM as a calibration image. This correction is done prior to the shutter velocity and standard calibration because in order to apply the non-linearity correction, the raw pixel value is required.

The next step is to apply the shutter correction. The physical shutter of the camera does not open and close instantaneously, therefore a pixel exposure time depends on its position in the CCD. This shutter effect will be larger for lower exposure times, because the ratio between the shutter-moving-time and the exposure time will be larger. The shutter correction is implemented in the pipeline with the following expression:

$$N_{corr}(x,y) = \frac{N(x,y)}{1 + s(x,y)/t_{exp}}, \tag{3.2}$$

where, t_{exp} is the exposure time of that image and $s(x,y)$ is the shutter map, which is pixel dependent and is provided by TFRM personnel as a calibration image. In principle, when conducting differential photometry, the shutter velocity is irrelevant as long as the pointing of the telescope and the exposures times are always the same. However, when observing for large periods of time, identical pointing and exposure time along years can not be assumed. Sometimes, for very bright objects a very short exposure time is required to avoid saturation, and in that case one has to find a trade-off between non-linear effects (increase exposure time), and shutter effects (decrease exposure time). Therefore, for very bright objects, both corrections are needed (e.g., see observations on very bright objects in Section A.1 and A.2).

Finally, the standard calibration is applied. The CCD is actively cooled down, but for large exposure times the CCD is slightly heated. This produces thermal agitation resulting in an increase of the noise, being this larger for higher temperatures (exposure times). To correct this effect the *dark* calibration image is subtracted to any image with non-zero exposure time. *Dark* images account for the thermal noise, and are built exposing the CCD with the same exposure as the image that has to be corrected, but with the shutter closed. In addition, the sensitivity of the CCD may be pixel dependent (e.g., non-identical pixels, and/or imperfections in the optical path like dust particles, resulting in some attenuation at some regions of the CCD). This non-homogeneous sensitivity is corrected by dividing the astronomical image by a *flat* image. *Flat* images are images obtained exposing the CCD under an homogeneous source of light (e.g., twilight images, or an image of a white screen). Prior to the *flat* correction, corrections of the read-out-noise and pixel-to-pixel variations in the zero-point can be applied by subtracting the *bias* image to all the images (astronomical, *flats*, and *darks*). *Bias* images are obtained exposing the CCD with the shortest possible exposure time (ideally zero seconds). However, since *dark* images have the *bias* signal embedded, any image that has been *dark*-subtracted is already *bias*-subtracted (this can not be applied if the *dark* image requires scaling). Because we are provided with *dark* images for both the astronomical images and the *flat* images by TFRM personnel, we do not conduct *bias*-subtraction. The standard calibration uses `IRAF`[2] routines (implemented through `PyRAF`[3]).

The image calibration module uses the `Astropy` package (Astropy Collaboration et al. 2013) to manipulate the images, which are provided in Flexible Image Transport System (`FITS`) format.

3.2 PHOTOMETRIC CALIBRATION

Photometric calibration involves all the steps from extracting the instrumental magnitudes until obtaining the final magnitude.

The first step, called photometric extraction, is to obtain the instrumental magnitudes, and build a catalog of objects from the astronomical image. The pipeline uses `SExtractor` for this purpose (Bertin & Arnouts 1996). We use `SExtractor` instead of `IRAF` routines because it conducts automatic aperture photometry with dynamic elliptical apertures, leading to a better precision compared with a single, non-dynamic, and circular aperture (e.g., `IRAF`), see `SExtractor` user's manual, and references therein. Once the photometric extraction has been conducted we discard the flagged stars (e.g., blended, saturated, etc.).

---

[2] `IRAF` is distributed by NOAO, which is operated by AURA, under cooperative agreement with NSF.

[3] `PyRAF` is a product of the Space Telescope Science Institute, which is operated by AURA for NASA.

The next step is the quality control. Because we are conducting long-term observational campaigns, and we are using the same reference stars for each image (and night), we need to discard those images that have low quality. To understand this, imagine that a cloud is covering a certain region of the FOV, or even worse, imagine that there is a thin cloud layer covering the image and we barely see any star. If we keep that image, and because all images have the same reference stars, we will loose most of the possible reference stars. If now we consider long-term observational campaigns this effect is cumulative along time. To avoid this, after conducting the photometric extraction we perform a simple (but efficient) quality control. The quality control consists on computing the maximum number of stars for that FOV using the whole data set, and then to discard those images with a low number of detections compared with the maximum number of stars (typically those with less than 40% of the maximum).

The next step is the star matching. To be able to use the same reference stars for each image, we need to perform a match between all the star catalogs built by `SExtractor` (one catalog per image). A catalog includes the magnitude and the estimated astronomical coordinates for each detection. The match is conducted using the `SkyCoord` module from `Astropy`. A second quality control is applied: those frames with a small number of matched stars, compared with the total number of stars at a certain reference frame, are discarded. After that, we have for each of the stars common in the whole data set: the magnitudes (for each image of each night), together with the astronomical coordinates.

The next step is to correct the instrumental magnitudes from atmospheric extinction and other systematic effects, using a differential photometry technique. The basic principle of the differential photometry is that when the difference between two instrumental magnitudes which are close in the sky is computed (the target and a reference star), then the systematic effects are removed from the target magnitude (including the atmospheric extinction). Therefore if one repeats this (with the same stars) for different images, the intrinsic variability of the target is obtained (assuming no variability in the reference star). The main difficulty is how to find those reference stars, and how to combine them in order to dilute any possible intrinsic variability. In the pipeline we implemented an iterative algorithm which is a modified version of the algorithm described in Broeg et al. (2005). The algorithm is implemented as follows:

1. Pick the instrumental magnitudes ($m_{i,j}^{inst}$). The subscripts i and j, denote the star i and the image (catalog) j, respectively.

2. From $m_{i,j}^{inst}$, pick a subset of stars having a magnitude ($m_{k,j}^{inst}$) within a certain range with respect the target magnitude. The subscripts k and j, denote the star k and the image j, respectively.

3. Assign a weight (w_k) to the star k, equal to 1 for each of the stars of the previous subset.

4. Correct the instrumental magnitudes of the whole initial data set ($m_{i,j}^{inst}$) as follows:
   a) Compute the correcting factor (Δm_j) for each image j, as the weighted average of the difference: $m_{k,j}^{inst}$-$m_{k,j=1}^{inst}$ (using only the stars in the subset, and their weights w_k). The correcting factor Δm_j is a measure of how much does the image j deviates from a reference frame, defined as the first image.
   b) Correct all the magnitudes ($m_{i,j}^{inst}$) from the initial set by subtracting Δm_j from them. This returns the corrected magnitudes ($m_{i,j}$) for the whole data set.

5. From the corrected magnitudes ($m_{i,j}$), pick a subset of stars having an average magnitude within the same range as in step 2, and filter for those which are located at a certain maximum distance with respect to the target. A star from this subset is denoted by the label k, having a corrected magnitude $m_{k,j}$, and an instrumental magnitude $m_{k,j}^{inst}$.

6. Compute a weight (w_k) for each of the selected stars in the subset as $w_k = \frac{1}{\sigma_k^2}$, being σ the standard deviation of the corrected magnitude of the star k. From that subset, keep only the n stars with the highest weight.

7. If the stars forming the subset of selected stars, or their ranking based on their weights, have been changed, go to step 4. Else stop.

When conducting differential photometry, we are interested in the variability of the photometric light curves. In order to check that any observed variability in the corrected light curves is caused by an intrinsic variability of the target, and not by an effect induced by an intrinsic variability of any of the reference stars, we repeat the magnitude correction process for different sets of reference stars (different sets of reference stars should lead to compatible results on the light curve of the target within uncertainties). The different sets are subsets of the final set, which has been obtained after the algorithm has converged in step 7.

The nightly observations are conducted in observation blocks of ~ 20 shots (i.e., images, and hence catalogs) per night. The optical photometry of the astronomical sources that we are interested in, does not present photometric variability on time scales smaller than one hour (within our photometric precision). Therefore, after obtaining the corrected magnitude for each image, we can average the ~ 20 measurements per night in a single measurement, obtaining a better precision. After that, an artificial offset is added to the average of the corrected magnitudes aimed to match the mean value (for the whole data set) with the tabulated value in the literature. Finally, the nightly uncertainties in the averaged magnitudes are estimated as the standard deviation of the magnitudes obtained from the single images for each night.

3.3 PLOTTING

Because we are interested in time series of the target magnitude, all of the plots involve the time-stamp of the observation, or some derived quantity such as the orbital phase. The pipeline includes some generic plots such as: nightly light curves, multi-night light curves or phase-folded light curves. But also includes the possibility to define specific plots for each scientific case, e.g., color-map of the magnitudes plotted against the orbital phase, and the superorbital cycle (see, e.g., figures in Chapter 4). Finally, some plots for sanity checks are produced. All of these plots are produced for each of the different reference stars sets built in the photometric calibration. These plots are useful to assess the reality of the variability detected in the target sources.

4

LONG-TERM OPTICAL OBSERVATIONS OF THE GAMMA-RAY BINARY LS I +61 303

LS I +61 303 is a gamma-ray binary hosting a compact object and a Be star. The optical emission is produced by the optical star and its circumstellar disk, being the orbital optical variability associated to perturbations of the circumstellar disk produced by the compact object along its orbital motion. LS I +61 303 also presents a multi-wavelength superorbital variability, that has been associated to periodic changes in the circumstellar disk.

In this chapter we present long-term optical observations of the gamma-ray binary LS I +61 303 conducted with the TFRM (see Section 2.1, and Section 3 for the data reduction) and the LT (see Section 2.2). Previous optical results on LS I +61 303 have been published in Paredes-Fortuny et al. (2014, 2015b).

4.1 INTRODUCTION

LS I +61 303 is the optical counterpart of the variable radio source GT 0236+610, which was discovered to be associated with the COS B gamma-ray source CG135+01 (Gregory & Taylor 1978; Gregory et al. 1979). LS I +61 303 is a galactic object placed at a distance of $\sim$ 2 kpc, based on H I measurements (Frail & Hjellming 1991). LS I +61 303 is hosting an optical star with $V \sim 10.7$ magnitude and spectral type $B0$ Ve, being a fast rotating early type star with a circumstellar decretion disk (Paredes & Figueras 1986; Hutchings & Crampton 1981; Casares et al. 2005). From radial velocity studies, the compact object can be a black hole or a neutron star. Currently, the pulsar-wind scenario that implies a neutron star is the most favored one, e.g., by the cometary tail morphologies seen in radio observations (Dhawan et al. 2006). However, X-ray and radio pulsations have not been found (Rea et al. 2010; McSwain et al. 2011; Cañellas et al. 2012). Alternative studies on the microquasar scenario have been conducted (e.g., Massi et al. 2001, 2004; Massi & Torricelli-Ciamponi 2016; Saha et al. 2016). Regardless of the scenario, the compact object is orbiting in a highly eccentric orbit with e in the range 0.54–0.72 (Casares et al. 2005; Aragona et al. 2009), with an orbital period of 26.4960 ± 0.0028 d (Gregory 2002).

A modulation of the flux synchronized with the orbital period has been detected from radio to very high-energy gamma rays (e.g., Taylor & Gregory 1982; Mendelson & Mazeh 1989; Paredes et al. 1994, 1997; Abdo et al. 2009; Albert et al. 2009; Marcote et al. 2016). LS I +61 303 also displays a long-term modulation on top of the orbital modulation. This superorbital variability was first detected in the amplitude of radio outburst by Paredes (1987) and Gregory et al. (1989). Gregory (2002) found a superorbital variability in the amplitude and orbital phase of the radio outburst with a period of 1667 ± 8 d (~ 4.6 yr), resulting in a drift of the orbital phase of the radio maximum from ~ 0.4 to ~ 0.9 orbital phases. The zero orbital and superorbital phases are defined at JD 2,443,366.775, being the periastron at orbital phase 0.23–0.28 (Casares et al. 2005; Aragona et al. 2009).

This ~ 4.6 yr superorbital variability has already been detected at all wavelengths. Zamanov et al. (2013) detected it in $EW_{\mathrm{H}\alpha}$ measurements using periodogram analysis, indicating that the superorbital variability could be related to periodic changes in the mass-loss rate of the Be star and/or variations in the circumstellar disk (see Massi & Torricelli-Ciamponi 2016; Saha et al. 2016 and references therein for an alternative interpretation). Li et al. (2012) discovered a superorbital variability in X-rays (3–30 keV) with a superorbital period compatible with that found from radio outbursts (Gregory 2002). Chernyakova et al. (2012) reported similar results together with contemporaneous radio observations, showing that the radio outbursts lag the X-ray maximum by ~ 0.2

orbital phases for the same superorbital phases. Ackermann et al. (2013) discovered a superorbital variability in gamma-rays (>100 MeV) compatible with the superorbital period found in radio. MAGIC Collaboration et al. (2016) found yearly variability in the TeV emission consistent with the superorbital period. Marcote et al. (2016) showed recently the existence of the superorbital variability at low radio frequencies as well.

Regarding the optical photometry, Zaitseva & Borisov (2003) found long-term variability in the averaged V-band magnitude, although a search for superorbital variability was not conducted. Recently, in the context of this thesis, we presented in Paredes-Fortuny et al. (2015b) the discovery of a superorbital variability in the optical photometry, reporting a phase shift of the maximum, and an increase in the optical flux, for data spanning ~ 1 yr. This superorbital variability was the missing piece in the multi-wavelength puzzle, and provided an evidence of the coupling between the thermal and non-thermal processes. In Paredes-Fortuny et al. (2015b), we also presented contemporaneous observations of $EW_{\mathrm{H}\alpha}$, reporting the already known superorbital flux variability, and, for the first time, a shift in the orbital phase of the maximum. We showed that the optical photometry displays a 0.1–0.2 phase lag with respect the contemporaneous $EW_{\mathrm{H}\alpha}$ observations.

In this work, we extend the contemporaneous optical photometry and $EW_{\mathrm{H}\alpha}$ observations of LS I +61 303 presented in Paredes-Fortuny et al. (2015b), with observations spanning nearly a whole superorbital cycle. We confirm the results presented in Paredes-Fortuny et al. (2015b), and show optical photometric (for the first time) and $EW_{\mathrm{H}\alpha}$ light curves compatible with the radio superorbital period of 1667 d. We discuss the results in a multi-wavelength context, and discuss on possible scenarios.

4.2 OBSERVATIONS AND DATA REDUCTION

We have conducted optical photometric observations and $EW_{\mathrm{H}\alpha}$ measurements of the gamma-ray binary LS I +61 303.

The optical photometric observations have been conducted with the robotic 0.5 m telescope TFRM (see Fors et al. 2013 and Section 2.1), and span from 2012 July 31 to 2016 January 27 (4 observational campaigns spanning a total of 3.5 yr) with 153 nights of good data (results on the first, and first and second observational campaigns have already been presented in Paredes-Fortuny et al. 2014, and Paredes-Fortuny et al. 2015b, respectively). The source has been observed ~ 20 times per night with exposures of 5–10 s (largest signal-to-noise ratio for the linear region of the CCD).

The data reduction and analysis has been conducted using the pipeline presented in Section 3. Because of the lack of a coherent set of calibration images (darks and flats) for the full monitoring (4 observational campaigns), we decided to disable standard calibration. The exposure times were high enough to avoid any shutter effect, but low enough to avoid any non-linearity effects of the CCD. Therefore, we disabled the shutter and non-linearity corrections. The light curves are corrected using a weighted average differential magnitude correction method using the 3 more constant stars in the field (see Section 3.2). The reference stars are ~ 1 mag fainter and are at a distance up to 21 arcmin with respect to LS I +61 303. The corrected light curves are averaged on a nightly basis, and we use an artificial offset to bring the instrumental magnitudes to a mean magnitude of 10.7 mag. The nightly uncertainties are estimated in a conservative way as the standard deviation of the magnitudes of the target obtained from the individual images for each night, being this in the 5–10 mmag range.

The $EW_{\mathrm{H}\alpha}$ measurements, which are contemporaneous with the photometric observations, have been obtained using FRODOspec on the robotic 2.0 m LT (see Section 2.2). The data span from 2012 July 2 to 2016 February 14 with 171 measurements (143 nights, 4 observational campaigns spanning a total of 3.6 yr), with exposures of 600 s. Results on the first and second yearly observational campaigns have already been presented in Paredes-Fortuny et al. (2015b). The data taking and reduction process have been conducted as in Casares et al. (2012). The nightly uncertainties of the $EW_{\mathrm{H}\alpha}$ measurements have been assumed to be at 10% level. The adopted convention is positive EW for emission.

4.3 RESULTS

The optical observations of the gamma-ray binary LS I +61 303 for the four yearly observational campaigns (all centered in autumn) plotted all together as a function of the MJD, and the orbital phase are shown in Fig. 4.1, both for the optical photometry (*top*, red), and the $EW_{\mathrm{H}\alpha}$ (*bottom*, blue). The folded light curves are plotted with a sinusoidal fit to the orbital variability, whose parameters (amplitude, phase of the maximum, and mean flux) can be found in Table 4.1-*first row*. From the folded light curves (Fig. 4.1-*right*) we can see the already known orbital variability (Zamanov et al. 2014; Paredes-Fortuny et al. 2015b), and a large scatter on top of the orbital variability.

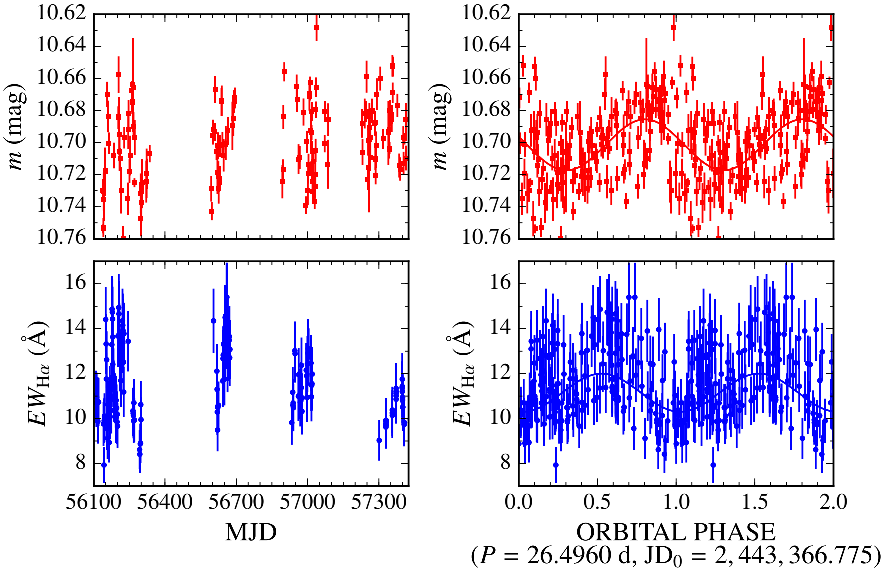

Figure 4.1: Optical photometric (*top*, red), and $EW_{\mathrm{H}\alpha}$ (*bottom*, blue) light curves of LS I +61 303 plotted as a function of the MJD (*left*), and folded with the orbital period (*right*). Error bars represent $1\,\sigma$ uncertainties. The solid lines in the folded light curves correspond to sinusoidal fits whose parameters can be found in Table 4.1-*first row*. Two cycles are displayed for clarity.

Table 4.1: Fitted sinusoidal parameters to the orbital modulation of the optical photometry and the $EW_{H\alpha}$ of LS I +61 303 for the total data set (Fig. 4.1-right) and for the four different observational seasons (Fig. 4.2). ϕ_{SO} stands for the approximate superorbital phase of the MJD of the optical photometry and $EW_{H\alpha}$ observations for a given season. The parameters are those of the functions: optical $m = -A\cos\left(2\pi\left[\phi - \phi_0\right]\right) + C$ and $EW_{H\alpha} = A\cos\left(2\pi\left[\phi - \phi_0\right]\right) + C$. Phases were computed using an orbital period of 26.4960 d and phase zero at JD 2,443,366.775.

Data set	ϕ_{SO}	$MJD^{optical}$	$A^{optical}$ (mmag)	$\phi_0^{optical}$	$C^{optical}$ (mag)	$MJD^{EW_{H\alpha}}$	$A^{EW_{H\alpha}}$ (Å)	$\phi_0^{EW_{H\alpha}}$	$C^{EW_{H\alpha}}$ (Å)
Total	-	56139–57414	16 ± 3	0.80 ± 0.03	10.701 ± 0.002	56110–57432	0.9 ± 0.1	0.53 ± 0.03	11.2 ± 0.1
Season 1	~ 0.7	56139–56335	32 ± 4	0.68 ± 0.02	10.707 ± 0.003	56110–56299	1.4 ± 0.3	0.56 ± 0.03	11.2 ± 0.2
Season 2	~ 0.95	56594–56693	22 ± 4	0.84 ± 0.03	10.701 ± 0.003	56604–56673	1.3 ± 0.3	0.78 ± 0.05	13.0 ± 0.3
Season 3	~ 0.2	56894–57086	30 ± 5	0.99 ± 0.02	10.701 ± 0.003	56933–57019	0.3 ± 0.2	0.64 ± 0.15	11.4 ± 0.2
Season 4	~ 0.4	57229–57414	10 ± 3	0.92 ± 0.06	10.692 ± 0.002	57301–57432	1.2 ± 0.2	0.41 ± 0.02	10.81 ± 0.09

We show in Fig. 4.2 the orbital variability of the optical photometry (Fig. 4.2-*left*, red) and the $EW_{\mathrm{H}\alpha}$ (Fig. 4.2-*right*, blue), together with a sinusoidal fit, for each of the yearly observational campaigns. The sinusoidal fits from each campaign, are plotted all together in the last row. The fitted parameters to the sinusoidal fits can be found in Table 4.1. From Fig. 4.2 and Table 4.1 we can see a clear positive drift in the orbital phase of the maximum of the optical photometry for each observational campaign (except for the last one, whose fit has a large uncertainty). The sinusoidal fits reveal a maximum phase drift in the optical photometry of 0.31 ± 0.03 orbital phases at $10\ \sigma$ confidence level (c.l.), between the first and the third observational campaigns for data spanning ~ 2.6 years (computed from Table 4.1). It is worth to mention the large scatter with respect to the sinusoidal fit in the last observational campaign, being this season the last one before the typical change in the superorbital behavior around superorbital phase $\phi_{\mathrm{SO}} \sim 0.5$ (Gregory 2002). Similarly, from Fig. 4.2 and Table 4.1 we see a clear positive drift too in the $EW_{\mathrm{H}\alpha}$ light curves from the first to the second observational campaigns, but unclear in the other campaigns. That positive drift is of 0.22 ± 0.06 orbital phases at 3.8σ c.l. for data spanning 1 yr (computed from Table 4.1). The lack of positive drift from the second to the third camping can attributed to the poor sampling (notice the large fit uncertainties in the sinusoidal fits from Table 4.1). However, the poor sampling in the fourth campaign does not seem to explain the absence of positive drift measured with respect any campaign (the position of the minimum seems well sampled). Equivalently to the optical photometry, this last campaign is the one before the typical change in the superorbital behavior. Comparing the individual optical light curves for each of the observational campaigns (Fig. 4.2) with respect to the light curve obtained using the whole data set (Fig. 4.1), we see a clear drop of the scatter. This is because we get rid of the drift in the phase of the maximum. From Table 4.1-*Seasons 1 and 2* we see that the maximum of emission occurs first in the $EW_{\mathrm{H}\alpha}$, and later in the optical photometry. This positive lag is of ~ 0.1, ~ 0.1, ~ 0.4, and ~ 0.5 orbital phases, for each of the four observational campaigns, respectively. All these results indicate the existence of a superorbital variability in the optical light curves, confirming the result already found from a smaller data set in Paredes-Fortuny et al. (2015b).

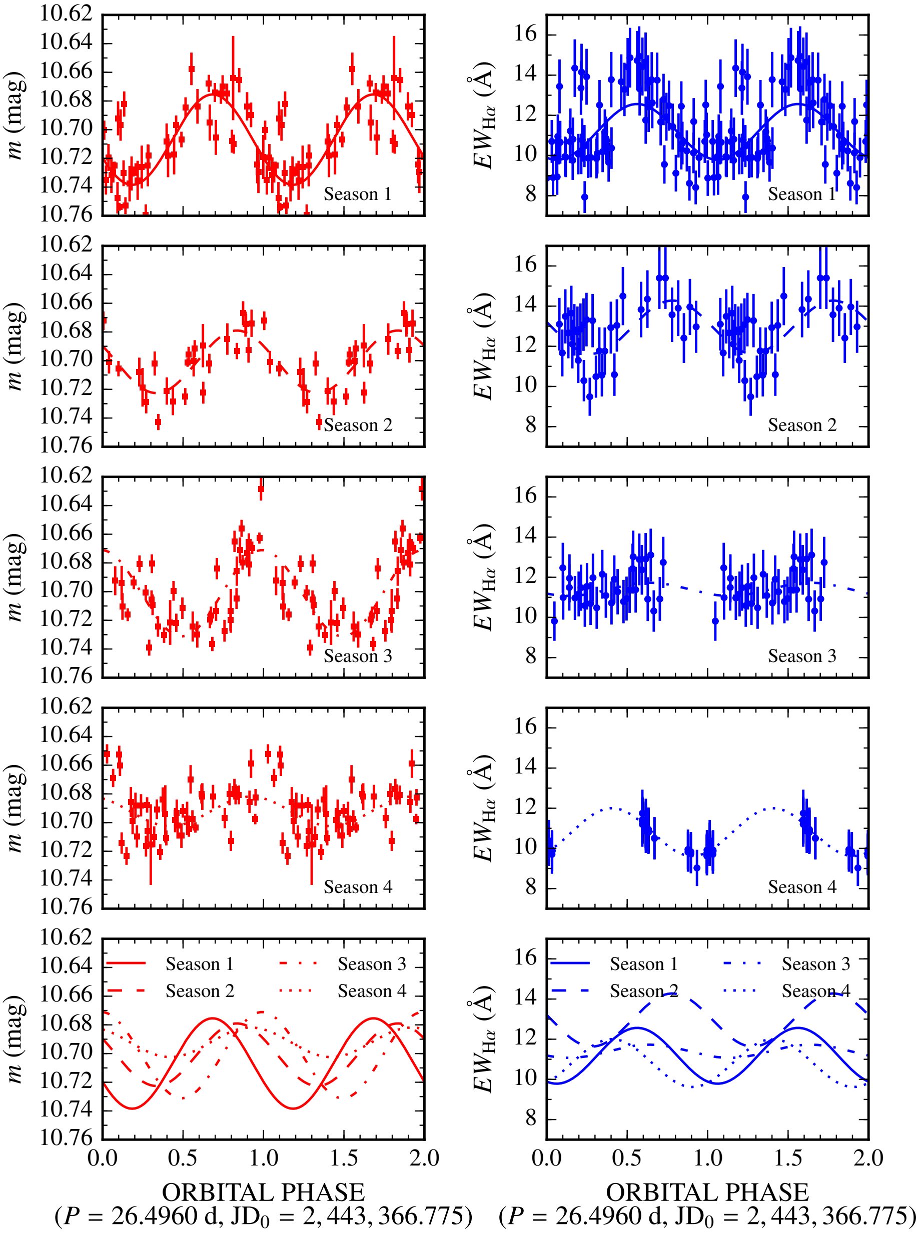

Figure 4.2: Optical photometric (*left*, red), and $EW_{H\alpha}$ (*right*, blue) light curves of LS I +61 303 (4 observational campaigns). The *bottom* panel shows all the sinusoidal fits (see Table 4.1).

We show in Fig. 4.3 the superorbital variability of the flux of the optical photometry and $EW_{\mathrm{H}\alpha}$ along the superorbital phase, respectively. The circles correspond to single measurements, while the green squares are the averaged values of each of the four yearly observational campaigns. The large scatter in both figures is due to the orbital variability. The superorbital variability of the optical photometry (Fig. 4.3-*top*) shows an approximately constant maximum flux ~ 10.66 mag and a minimum flux that increases from ~ 10.76 mag to ~ 10.72 mag, from superorbital phase ~ 0.6 to ~ 0.4. The averages, thus, show a monotonic increase, before starting the next cycle again at superorbital phase ~ 0.5 (Gregory 2002). Despite it looks a sawtooth behavior, we can not infer a firm conclusion on that due to the lack of data at superorbital phases close to ~ 0.5. The superorbital variability of the $EW_{\mathrm{H}\alpha}$ flux (Fig. 4.3-*bottom*) presents a variability compatible with the superorbital period. This variability displays a symmetric behavior with respect to the maximum, placed at superorbital phase ~ 1. Similar results but using an older estimation of the superorbital period, of 1584 d, were found by Zamanov et al. (1999).

To better display the superorbital variability, color maps of the optical photometry and $EW_{\mathrm{H}\alpha}$ as a function of the orbital phase and superorbital cycle are shown in Fig. 4.4. The red and blue crosses correspond to the phases of the maxima of the sinusoidal fits to the orbital variability of the optical photometry and $EW_{\mathrm{H}\alpha}$, respectively, for the different campaigns (see Table 4.1). The dotted red and blue lines represent the orbital phase drifts of the corresponding maxima along the superorbital cycle for the contemporaneous optical photometry and $EW_{\mathrm{H}\alpha}$ presented here (superorbital cycle 7.6–8.4). The dotted red line has been obtained as a linear fit to the 4 red crosses (Table 4.1). This superorbital variability displays a similar behavior than the one of the optical photometric flux from Fig. 4.3-*top*. The dotted blue line of the $EW_{\mathrm{H}\alpha}$ has been obtained as a linear fit to the 3 first blue crosses (Table 4.1). The last blue cross, corresponding to the last observational campaign, has been excluded from the fit as it deviates significantly from the previous linearly increasing trend. Its superorbital phase is close to $\phi_{\mathrm{SO}} \sim 0.5$, when there is the typical change in the superorbital behavior (Gregory 2002). In addition, the superorbital variability of the $EW_{\mathrm{H}\alpha}$ flux displays a similar behavior, be-

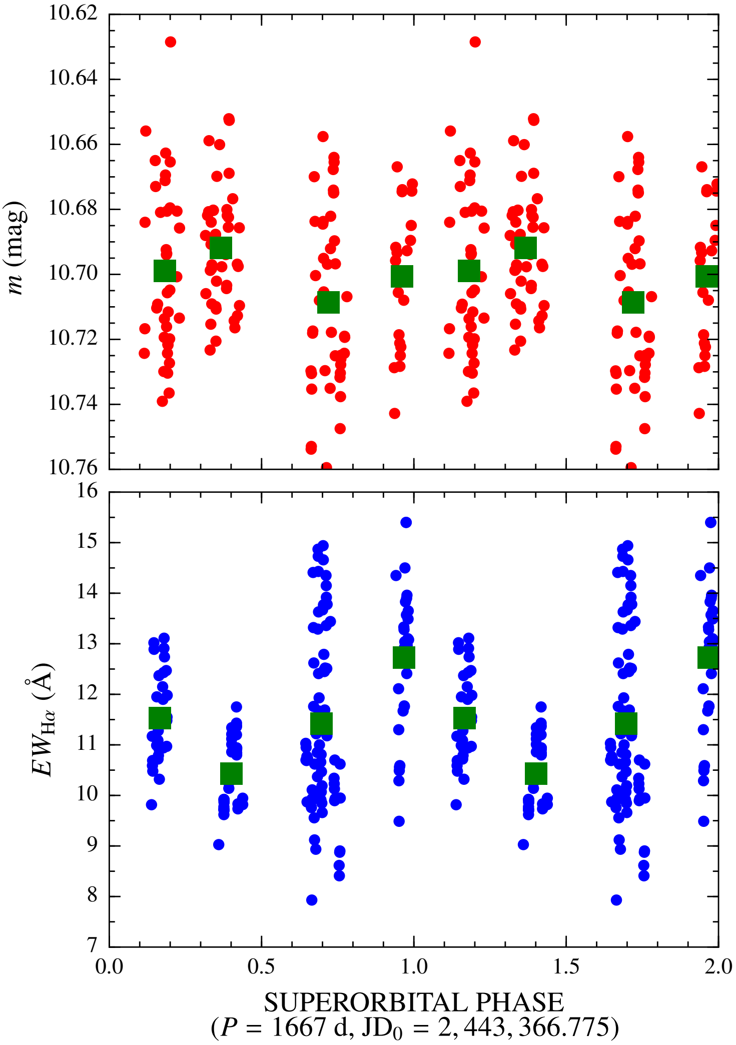

Figure 4.3: Optical photometry (*top*, red) and $EW_{\mathrm{H}\alpha}$ (*bottom*, blue) of LS I +61 303 plotted as a function of the superorbital phase. The green squares correspond to the averaged values of each of the the yearly observational campaigns. Two cycles are displayed for clarity.

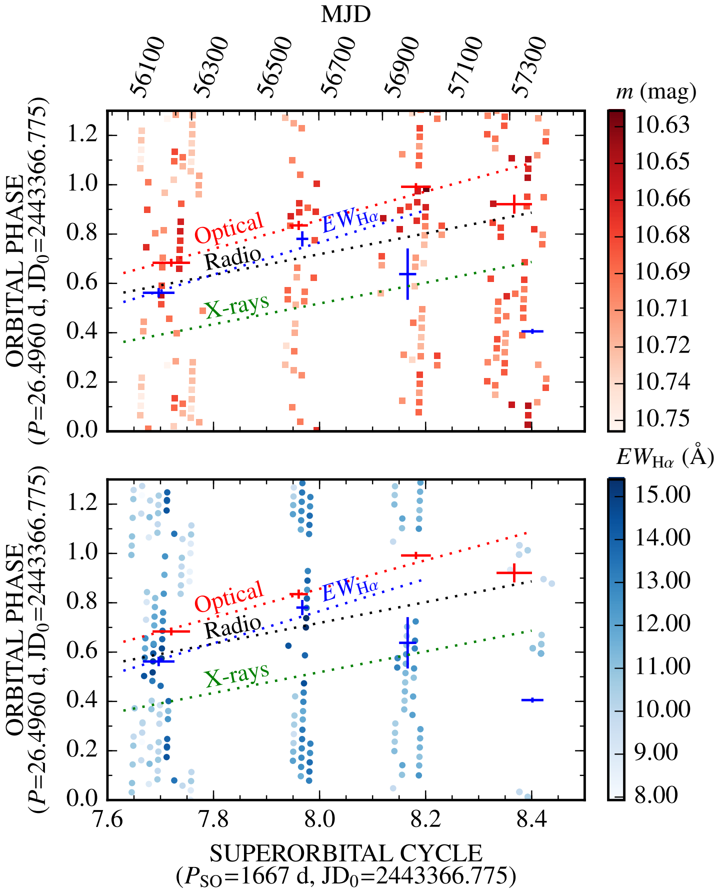

Figure 4.4: Color maps of the optical photometry (*top*, red) and $EW_{\mathrm{H}\alpha}$ (*bottom*, blue) from LS I +61 303 as a function of the orbital phase and superorbital cycle in mag and Å, respectively. The red and blue crosses correspond to the phases of the maxima of the sinusoidal fits to the orbital variability of the optical photometry and $EW_{\mathrm{H}\alpha}$, respectively (see Table 4.1). The dotted color lines represent the orbital phase drift of the emission peaks caused by the superorbital variability for the optical photometry (red), $\mathrm{EW}_{\mathrm{H}\alpha}$ (blue), radio (black), and X-rays (green). The dotted red line has been obtained as a linear fit to the 4 red crosses. Whereas the dotted blue line has been obtained as a linear fit to the 3 first blue crosses (Table 4.1). The radio and X-ray trends have been obtained from Chernyakova et al. (2012) using data of the previous superorbital cycle.

ing this more suitable for a sinusoidal fit than for a fit with a sawtooth profile. The contemporaneous radio and X-ray fluxes of the previous superorbital cycle (superorbital cycle 6) from Chernyakova et al. (2012) are shown as black and green dotted lines, respectively. The optical photometric observations show a lag of ~0.1 in orbital phase with respect to the radio outburst, and ~0.3 with respect to the X-ray outbursts for equivalent superorbital phases one cycle apart. The $EW_{\mathrm{H}\alpha}$ maxima, for the first two observational campaigns, occur at orbital phases similar to the radio outbursts for similar superorbital phases one cycle apart, whereas it is delayed by ~ 0.2 and ~ 0.5 orbital phases for the last two observational campaigns, respectively. In the averaged data of Zamanov et al. (2013, 2014) the maxima occur during the rising of the radio flux density.

Now we split the optical photometry in 10 consecutive orbital phase bins of 0.1 phases width, as done by Ackermann et al. (2013) using *Fermi* data, but using here the orbital phase of the periastron as reference. That binning is equivalent to conduct horizontal slices of 0.1 orbital phase width in Fig. 4.4-*top*. The photometric variability for each of these 10 orbital phase bins, plotted as a function of the 1667 d superorbital period is shown in red circles in Fig. 4.5. The green squares correspond to 0.2 superorbital phase width binning of the red circles. The dashed horizontal lines, placed at $m = 10.7$ mag, correspond to the mean value of the whole data set. The solid lines are the sinusoidal fits to the superorbital variability (red circles) for each bin. The sinusoidal fits from the orbital phase bins 0.73–0.83 and 0.83–0.93 presented large uncertainties (meaningless fits) and have not been drawn. The fitted parameters (amplitude, phase of the maximum and mean flux) for each orbital phase bin can be found in Table 4.2.

From Fig. 4.5 and Table 4.2 we clearly see a flux modulation compatible with the superorbital variability, being this very clear in some bins (e.g., orbital phase bins: 0.93–0.03 and 0.53–0.63), not so clear in some other bins (e.g., orbital phase bin: 0.43–0.53), and absent (or almost) at the orbital phase bins 0.73–0.83 and 0.83–0.93. From Fig. 4.5 and using the dashed horizontal line as reference level, we clearly see a modulation in the mean flux along different orbital phase bins, i.e., the orbital

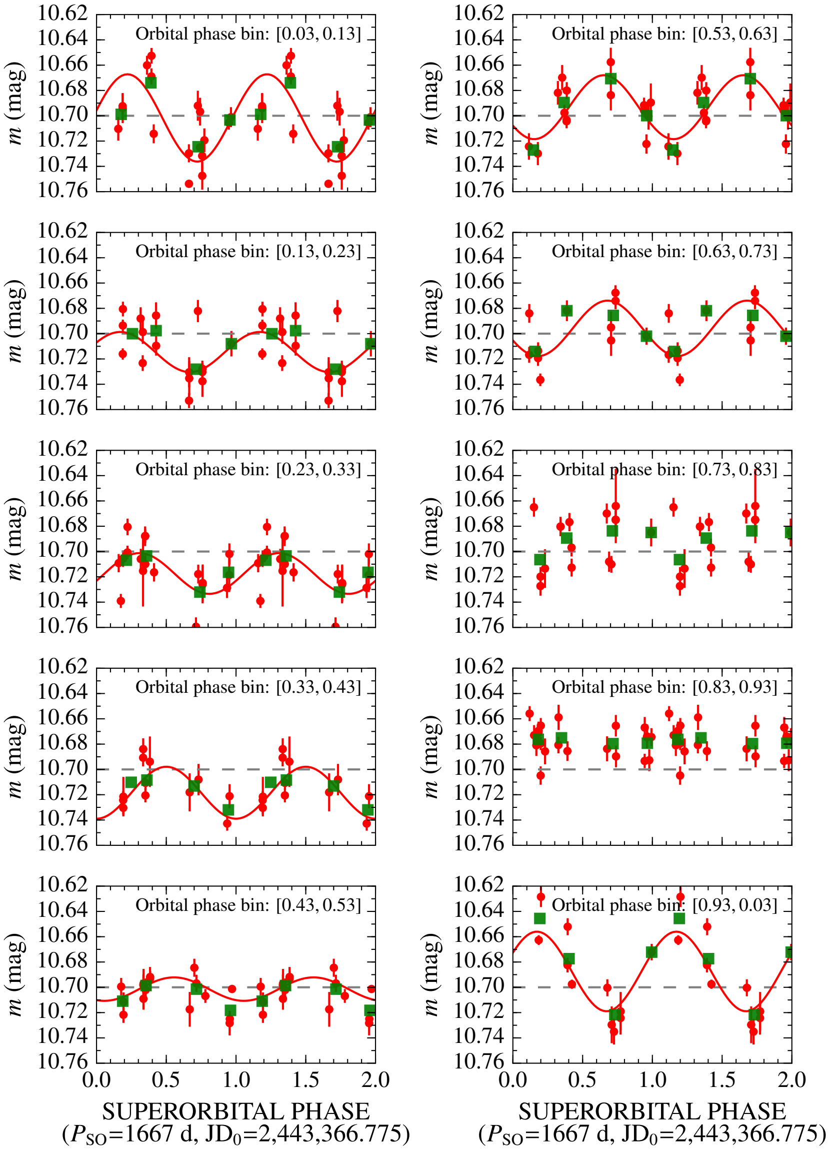

Figure 4.5: Optical photometry of LS I +61 303 plotted as a function of the superorbital phase for different orbital phase bins of 0.1 width (red circles). The solid lines correspond to sinusoidal fits (parameters listed in Table 4.2). The green squares correspond to 0.2 superorbital phase width binning of the red circles. The dashed line is placed at $m = 10.7$ mag for reference. Two cycles are displayed for clarity.

variability. This behavior is clearly visible in Fig. 4.6 where we plot the average flux of each orbital phase bin along the orbital phase, obtaining the average orbital modulation from Fig. 4.1-*top-right*. The error bars of the magnitude are computed as the standard deviation of the values within each bin, while the orbital phase error bars extend from the minimum to the maximum phase values observed within each bin. From Fig. 4.6 we observe a maximum in the optical photometric flux at orbital phase ~ 0.9 (i.e., after apastron which is at phase ~ 0.73), and a minimum at orbital phase 0.2–0.4 (i.e., just after periastron at phase ~ 0.23). In Fig. 4.7 we plot the standard deviation of the magnitude within each bin, i.e, the error bars from Fig. 4.6. In Fig. 4.7 we see a maximum of the standard deviation at orbital phase ~ 0.0, followed by a monotonically decrease until orbital phase 0.5, a secondary maximum at orbital phase 0.6–0.8, and another minimum value of the standard deviation at orbital phase ~ 0.9 (with a similar level than the one at orbital phase ~ 0.5).

Table 4.2: Fitted parameters to the superorbital modulation of the optical photometry for 10 orbital phase bins (Fig. 4.5). The parameters are those of $m = -A\cos(2\pi[\phi - \phi_0]) + C$. Orbital and superorbital phases were computed using an orbital and superorbital period of 26.4960 d and 1667 d, respectively, and phase zero at JD 2,443,366.775. Fitting to the $[0.73, 0.83]$ and $[0.83, 0.93]$ yield to meaningless fits.

Orbital phase	A (mmag)	ϕ_0	C (mag)
$[0.03, 0.13]$	35 ± 8	0.22 ± 0.05	10.702 ± 0.007
$[0.13, 0.23]$	16 ± 6	0.17 ± 0.10	10.715 ± 0.005
$[0.23, 0.33]$	16 ± 6	0.31 ± 0.08	10.717 ± 0.005
$[0.33, 0.43]$	21 ± 7	0.50 ± 0.06	10.718 ± 0.005
$[0.43, 0.53]$	9 ± 4	0.56 ± 0.06	10.701 ± 0.003
$[0.53, 0.63]$	25 ± 10	0.65 ± 0.02	10.693 ± 0.004
$[0.63, 0.73]$	22 ± 6	0.68 ± 0.09	10.696 ± 0.006
$[0.73, 0.83]$	-	-	-
$[0.83, 0.93]$	-	-	-
$[0.93, 0.03]$	31 ± 8	0.17 ± 0.04	10.687 ± 0.006

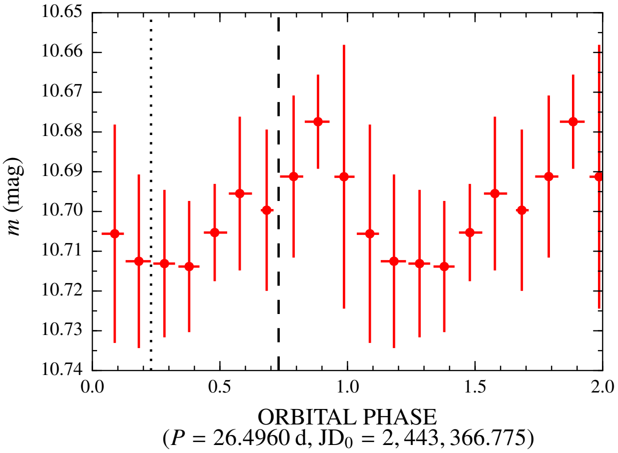

Figure 4.6: Binned optical photometric light curve plotted as a function of the orbital phase. The averaged magnitudes and orbital phases are computed from the 0.1 width orbital phase bins from Fig. 4.5. Magnitude error bars are computed as the standard deviation of the values within each bin. Orbital phase error bars extend from the minimum to the maximum phase values observed within each bin. The dotted line is placed at periastron phase 0.23. The dashed line is located at apastron phase 0.73. Two cycles are displayed for clarity.

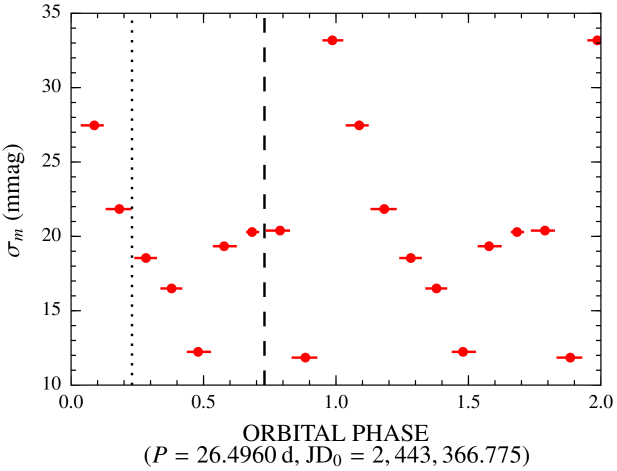

Figure 4.7: Standard deviation of the optical photometry of the 0.1 width orbital phase bins i.e., the error bars from Fig. 4.6. The remaining plot properties are the same as those of Fig. 4.6.

Now we perform the same study with the $EW_{\mathrm{H}\alpha}$. This is shown in Fig. 4.8 and Table 4.3. From there, we clearly see an $EW_{\mathrm{H}\alpha}$ modulation compatible with the superorbital variability, being this very clear in some bins (e.g., orbital phase bins: 0.53–0.63 and 0.63–0.73), not so clear in some other bins (e.g., orbital phase bins: 0.13–0.23 and 0.23–0.33), and absent (or almost) at the orbital phase bin 0.33–0.43. The poor sampling and/or lack of variability did not allow a proper sinusoidal fit in the orbital phase bins: 0.33–043, 0.73–0.83, and 0.93–0.03. The dashed horizontal lines, placed at $\mathrm{E}W_{\mathrm{H}\alpha} = 11.5$ Å, correspond to the mean value of the whole data set. From Fig. 4.8 and using the dashed horizontal line, as reference level, we clearly see a modulation in the mean $EW_{\mathrm{H}\alpha}$ along different orbital phase bins, i.e., the orbital variability. This behavior is clearly visible in Fig. 4.9 where we plot the average $EW_{\mathrm{H}\alpha}$ of each orbital phase bin along the orbital phase, obtaining the average orbital modulation from Fig. 4.1-*bottom-right*. The error bars of the $EW_{\mathrm{H}\alpha}$ are computed as the standard deviation of the values within each bin, while the orbital phase error bars extend from the minimum to the maximum phase values observed within each bin. From Fig. 4.9 we observe a maximum in the $EW_{\mathrm{H}\alpha}$ at orbital phase 0.5–0.8 (i.e., before/close to apastron at orbital phase ~ 0.73), and a minimum at orbital phase ~ 0 (i.e., before periastron at orbital phase ~ 0.23). The plot of the standard deviation of the $EW_{\mathrm{H}\alpha}$, analogous to that from the optical photometry (Fig 4.7), is shown in Fig. 4.10, although in some cases it has been computed from poorly sampled orbital phase bins (see Figs. 4.2 and 4.8).

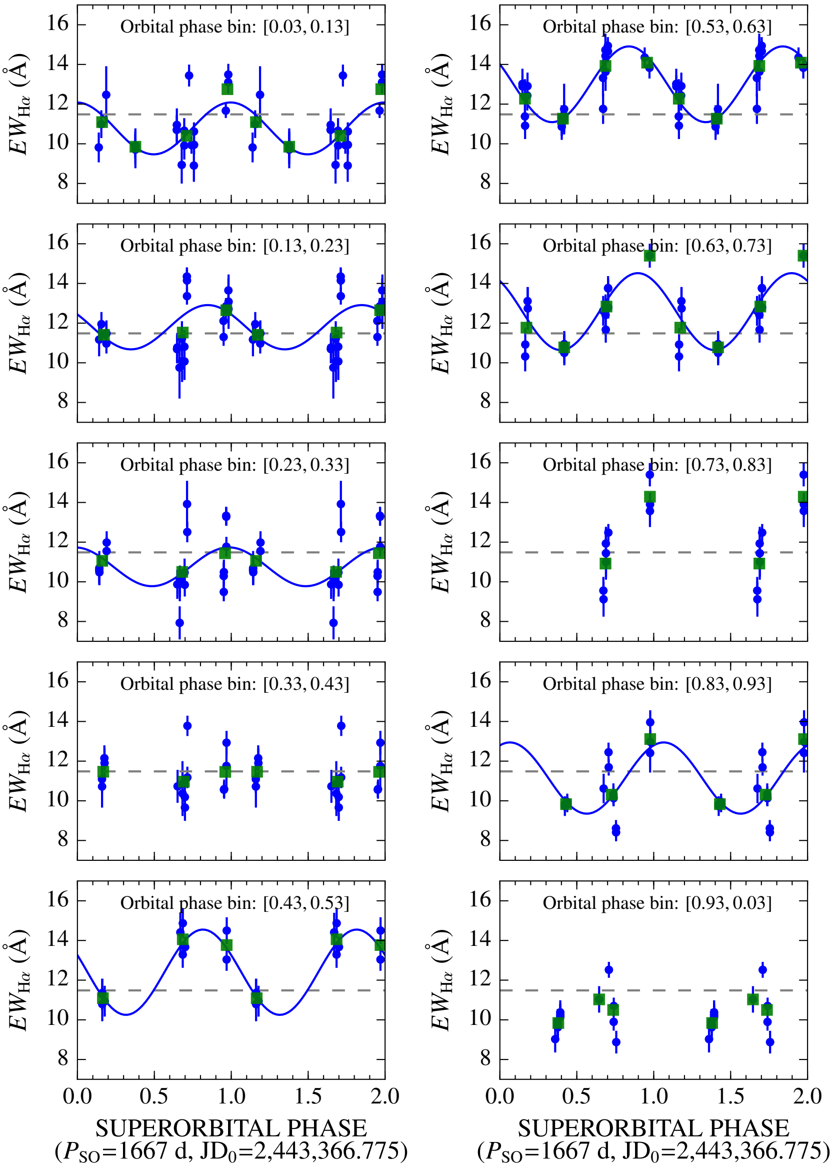

Figure 4.8: $EW_{\mathrm{H}\alpha}$ of LS I +61 303 plotted as a function of the superorbital phase for different orbital phase bins of 0.1 width (blue circles). The solid lines correspond to sinusoidal fits (parameters listed in Table 4.3). The green squares correspond to 0.2 superorbital phase width binning of the blue circles. The dashed line is placed at $\mathrm{EW}_{\mathrm{H}\alpha} = 11.5$ Å for reference. Two cycles are displayed for clarity.

Table 4.3: Fitted sinusoidal parameters to the superorbital modulation of the $EW_{H\alpha}$ of LS I +61 303 for 10 orbital phase bins (Fig. 4.8). The parameters are those of the function: $EW_{H\alpha} = A\cos\left(2\pi\left[\phi - \phi_0\right]\right) + C$. Orbital and superorbital phases were computed using a superorbital period of 1667 d, and an orbital period of 26.4960 d, respectively, and phase zero at JD 2,443,366.775. Sinusoidal fits to the $[0.33, 0.43]$, $[0.73, 0.83]$ and $[0.93, 0.03]$ yield to fits with very large uncertainties (meaningless fits).

Orbital phase	A (Å)	ϕ_0	C (Å)
$[0.03, 0.13]$	1.3 ± 0.4	0.50 ± 0.04	10.8 ± 0.3
$[0.13, 0.23]$	1.1 ± 0.5	0.35 ± 0.05	11.8 ± 0.3
$[0.23, 0.33]$	1.0 ± 0.7	0.48 ± 0.09	10.8 ± 0.5
$[0.33, 0.43]$	-	-	-
$[0.43, 0.53]$	2.2 ± 0.5	0.32 ± 0.03	12.4 ± 0.3
$[0.53, 0.63]$	1.9 ± 0.2	0.34 ± 0.02	13.0 ± 0.1
$[0.63, 0.73]$	1.9 ± 0.3	0.40 ± 0.03	12.6 ± 0.2
$[0.73, 0.83]$	-	-	-
$[0.83, 0.93]$	1.8 ± 0.8	0.56 ± 0.04	11.1 ± 0.5
$[0.93, 0.03]$	-	-	-

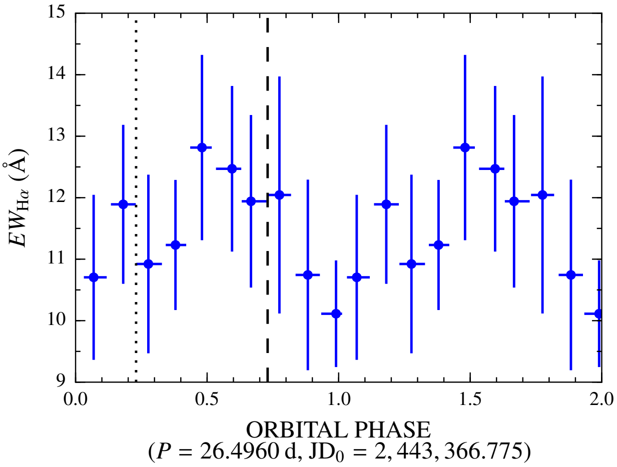

Figure 4.9: Binned $EW_{H\alpha}$ plotted as a function of the orbital phase. The averaged magnitudes and orbital phases are computed from the 0.1 width orbital phase bins from Fig. 4.8. Magnitude error bars are computed as the standard deviation of the values within each bin. Orbital phase error bars extend from the minimum to the maximum phase values observed within each bin. The dotted line is placed at periastron phase 0.23. The dashed line is located at apastron phase 0.73. Two cycles are displayed for clarity.

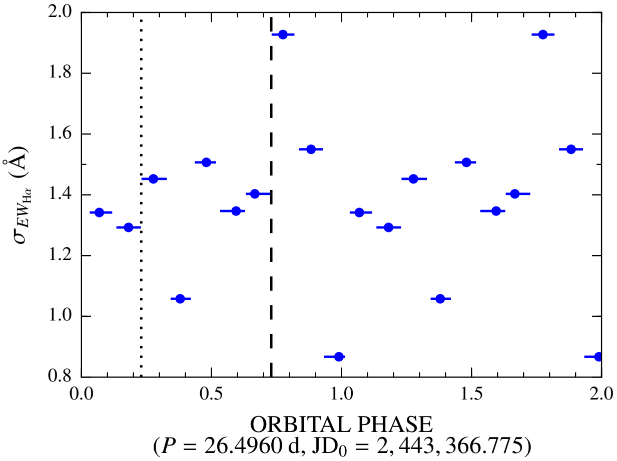

Figure 4.10: Standard deviation of the $EW_{H\alpha}$ of the 0.1 width orbital phase bins i.e., the error bars from Fig. 4.9. The remaining plot properties are the same as those of Fig. 4.9.

4.4 DISCUSSION

The optical observations of the gamma-ray binary LS I +61 303 presented in this thesis confirm the optical long-term variability published in Paredes-Fortuny et al. 2015b. In addition, the observations show, for the first time, an optical photometric and $EW_{\mathrm{H}\alpha}$ long-term variability consistent with the 1667 d superorbital period at different orbital bins (Figs. 4.5 and 4.8). This long-term variability is responsible for the large scatter displayed in the optical light curves when these span a long time and are folded with the orbital period (see Fig. 4.1-right). This scatter is largely reduced when the optical data is plotted separately in smaller sets, at the expense of the appearance of a drift in the orbital phase of the maximum in each set (see Fig. 4.2 and Table 4.1). In this section we discuss the orbital and superorbital variability of the optical photometry and the $EW_{\mathrm{H}\alpha}$, and their implications on the circumstellar disk structure. A cartoon representing the orbit of the compact object around the optical star LS I +61 303 is shown in Fig. 4.11, as it is useful for discussion.

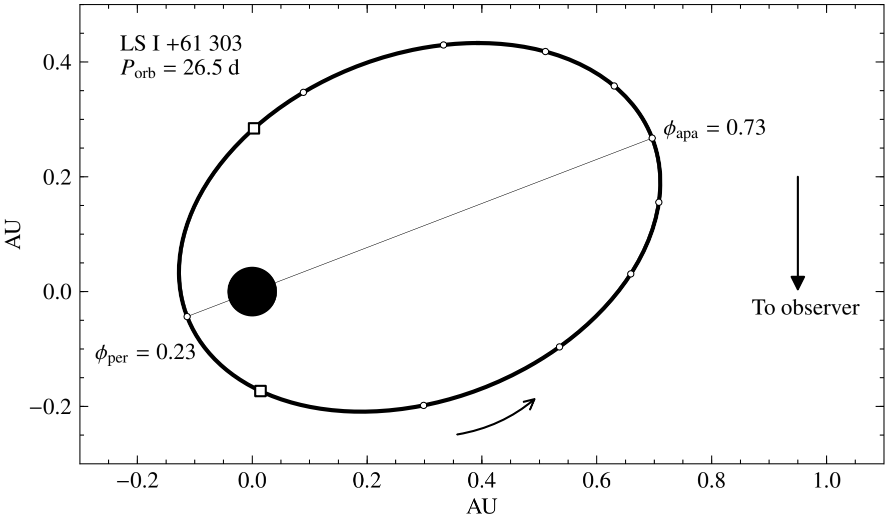
LS I +61 303
P_{orb} = 26.5 d
ϕ_{apa} = 0.73
ϕ_{per} = 0.23
To observer
AU
AU
0.4
0.2
0.0
−0.2
−0.2
0.0
0.2
0.4
0.6
0.8
1.0

Figure 4.11: Orbit of the compact object (black ellipse) around the star (black circle). White circles are plotted every 0.1 orbital phases. The squares mark the inferior and superior conjunction of the compact object at orbital phases 0.26 and 0.16, respectively. Adapted from Moldón (2012), using the orbital parameters from Casares et al. (2005).

4.4.1 *On the orbital variability*

The optical variability observed in each of the yearly observational campaigns is compatible with the $\sim$ 26.5 d orbital period (see Fig. 4.2). Casares et al. (2005) estimated that 35% of the optical flux in the gamma-ray binary LS I +61 303 is emitted from the inner regions of the decretion disk surrounding the Be star. The optical photometric orbital variability may be linked to the periodic interaction of the compact object and the circumstellar disk during the $\sim$ 26.5 d orbit. Under the assumption that the circumstellar disk is optically thick, the observed optical photometric flux will be proportional to the projected area of the emitting disk (Rivinius et al. 2013). That is, the orbital variability seen in the optical photometric light curves (see Fig. 4.2-left) may be interpreted as a periodic perturbation of the circumstellar disk by the compact object (see e.g., Massi & Torricelli-Ciamponi 2016 for alternative interpretations). This perturbation could be caused by tidal forces produced by the compact object, and/or the putative pulsar wind. This interpretation is supported by the orbital variability of the $EW_{\mathrm{H}\alpha}$ (see Fig. 4.2-right), an emission line that is present in circumstellar disks of Be stars and is a good tracer of the outer disk conditions (e.g., Negueruela et al. 1998). In this scenario, the perturbation, i.e., the decrease in the optical flux, starts as soon as the compact object approaches enough to the circumstellar disk.

The multi-wavelength orbital behavior can be clearly seen from vertical slices of Fig. 4.4. After periastron passage, first there is a maximum in the X-ray flux, caused by non-thermal processes. Then there is a maximum in the $EW_{\mathrm{H}\alpha}$, tracer of the outer parts of the disk (see Rivinius et al. 2013, Negueruela et al. 1998 and references therein), and radio, which is non-thermal emission from regions outside the binary system. Finally there is a maximum in the broadband optical photometry, which is thermal emission from inner parts of the disk, see Rivinius et al. (2013) and references therein. This wavelength dependence on the orbital phase of the outbursts is consistent with the fact that several emitting regions and processes, with different timescales, are involved. Because the $EW_{\mathrm{H}\alpha}$ traces the outer disk radius, it seems natural that the $EW_{\mathrm{H}\alpha}$ is affected before the optical photometry, which traces the inner parts of the disk (see

Fig. 4.4 and Table 4.1). This shift in phase is the first hint of a coplanar or quasi-coplanar circumstellar disk to the orbital plane (see Section 4.4.2.4 for a discussion on the circumstellar disk inclination in the superorbital context).

The optical photometric flux shows a ~ 0.06 mag variability (see, e.g., Table 4.1-Season 1-A^{optical}), corresponding to a $\sim 16\%$ of the disk flux (Casares et al. 2005), whereas the $EW_{\text{H}\alpha}$ shows a $\sim 30\%$ variability (see, e.g., Table 4.1-Season 1-$A^{EW_{\text{H}\alpha}}$). This higher variability in the $EW_{\text{H}\alpha}$ flux can be explained assuming a larger perturbation of the outer parts of the circumstellar disk ($EW_{\text{H}\alpha}$ emitting region), compared to the inner parts (optical photometry emitting region). This interpretation is compatible with the hypothesis that, because the circumstellar disk is a decretion disk, the outer parts of the disk are probably less dense than the inner parts, and hence should be more affected by the compact object interaction.

4.4.2 *On the superorbital variability*

The optical photometric and $EW_{\text{H}\alpha}$ fluxes present a modulation compatible with the 1667 d superorbital variability (Figs. 4.5 and 4.8). In addition, they present a superorbital variability of the orbital phase of the maximum similar to that seen in radio and X-rays (e.g., Gregory 2002; Li et al. 2012; Chernyakova et al. 2012; see also Fig. 4.2 and 4.4) at least during the first three seasons. These results suggest, for the first time, an evidence of coupling between thermal and non-thermal emission processes in the gamma-ray binary LS I +61 303 (conclusion published in Paredes-Fortuny et al. 2015b).

Because the $EW_{\text{H}\alpha}$ is a tracer of the circumstellar disk, its superorbital variability implies that the multi-wavelength superorbital variability might be correlated with a 1667 d periodic long-term variability of the Be circumstellar disk (e.g., density, geometry, etc.). In this context, the compact object faces different disk configurations in different orbital cycles. Hence, the perturbation degree induced to the disk by the compact object for a certain orbital phase, will depend on the intrinsic properties of the disk at that superorbital phase. Therefore, the resulting disk emitting area, which is responsible of the photometric flux, will depend on the orbital and superorbital phase of the disk.

Specifically, the following discussion will assume the density wave scenario (see, e.g., Negueruela et al. 1998). In the density wave scenario, the superorbital variability is explained by a density wave propagating azimuthally along the disk with the 1667 d superorbital period. As a result of that, the perturbation degree of the interaction between the compact object and the circumstellar disk for a given orbital phase depends on the superorbital phase. For instance, if the compact object is a young pulsar, the disruption degree of the circumstellar disk by the pulsar wind will depend on the density of the region of the circumstellar disk closer to the pulsar at that orbital and superorbital phases, being the disruption larger for lower densities, and vice-versa. We use this scenario as it is a very illustrative model, but another type of periodical variability of the physical properties of the disk may apply.

In the density wave scenario, we expect to observe superorbital optical variability at those orbital phases where the compact object is interacting with the circumstellar disk, and therefore at those phases in which the density plays a role in the perturbation degree resulting from the interaction. We also expect to see superorbital variability at those orbital phases where the compact object is not interacting with the circumstellar disk but the disk is still recovering from the previous interaction. We assume that the influence of the disk superorbital variability alone on the photometry is minor (the disk is assumed to be optically thick).

4.4.2.1 *On the superorbital variability: Optical photometry*

The superorbital variability of the optical photometric flux presents a different behavior depending on the orbital phase. From Fig. 4.5 and Table 4.2, we see that the superorbital variability starts to dim in the orbital range 0.63–0.73. This attenuation of the superorbital effect close to apastron phases (see Fig. 4.11) might be understood as the disk being recovered from the prior perturbation of the compact object (which is superorbital dependent), hence being less affected by the superorbital effect. The superorbital variability vanishes in the orbital phase bin 0.83–0.93. This might be interpreted as the disk being fully recovered from the prior disk-compact object interaction. In this phase bin, the superorbital variability of the disk density does not have any effect on the thermal emission, as this requires an interaction with the compact object that is missing. From Fig. 4.5 and Table 4.2 we also see a diminishing in the superorbital variability at orbital phase bin 0.43–0.53 (after periastron passage, at orbital phase 0.23). This attenuation might be caused by the strong perturbation of the disk due to the periastron passage of the compact object, resulting in a decrease of the overall optical emission (see Fig. 4.6), independently of the superorbital variability.

In addition, from Fig. 4.5 and Table 4.2 we see that after that lack of superorbital variability at the orbital phase bin 0.83–0.93 (~0.9 for simplicity), there is a sudden enhancement of the superorbital variability at the next orbital phase bin, 0.93–0.03 ($\sim$ 0.0 for simplicity). In the context of our discussion, this implies that the compact object has started to interact with the disk again, either gravitationally or by the ram pressure of the pulsar wind. As a first order approximation, this probably requires an optically emitting circumstellar disk extending close enough to the position of the compact object at orbital phases close to $\sim$ 0.0, and, assuming a symmetric disk, also to $\sim$ 0.5. The distance from the compact object to the massive star at these orbital phases is around 5 times the periastron distance (Casares et al. 2005).

The extended disk hypothesis, built from the optical photometric superorbital variability at different orbital phase bins, is also supported by the orbital variability of the flux. Figure 4.6 shows the averaged flux at each orbital phase bin, being the maximum flux reached at orbital phase $\sim$ 0.9. This supports the hypothesis that the disk is fully recovered at the orbital phase bin 0.83–0.93, corresponding to a maximum of thermal emitting area. The error bars are the standard deviation of the magnitude of each bin, being larger just after the maximum flux.

The hypothesis of an extended disk is also supported by Fig. 4.7. In Fig. 4.7 we show the error bars from Fig. 4.6, i.e., the standard deviation of the magnitude at each orbital phase bin, against the central orbital phase of each bin. Assuming a fairly-homogeneous sampling of the magnitude within each orbital phase bin, we can interpret the standard deviation of each bin, as a proxy of the level of superorbital variability at those orbital phases. From Fig. 4.7 we see a maximum in the standard deviation (superorbital variability) at orbital phase ∼ 0.0, i.e., when the compact object starts the interaction again with the circumstellar disk. After the maximum, the standard deviation (superorbital variability) monotonically decreases until orbital phase ∼ 0.5, i.e., the perturbation induced by the compact object to the disk causes the attenuation of the optical emission (including the optical photometric superorbital variability). From orbital phase ∼ 0.5 until orbital phase ∼ 0.8 the standard deviation (superorbital variability) monotonically increases, i.e., the disk recovers faster than it is perturbed (or simply the compact object stopped perturbing the disk), hence increasing its emission, and therefore its superorbital modulation (the standard deviation). This recovery of the disk at superorbital phase ∼ 0.5, would support the approximation of the disk extending relatively close to the compact object position (at superorbital phase ∼ 0.0), as the superorbital phase ∼ 0.5 is approximately symmetric to ∼ 0.0. Suddenly the standard deviation (superorbital variability) drops and reaches a minimum at orbital phase ∼ 0.9, i.e., at those orbital phases where the disk has been fully recovered from prior interactions and the pulsar is not interacting anymore with the disk. In this context, from Fig. 4.7, we see larger superorbital variability (standard deviation) when the compact object interacts with the circumstellar disk (orbital phase ∼ 0.0), than when the disk is recovering from a prior interaction (orbital phase ∼ 0.8).

In summary, there are several arguments that favor an extended disk that would reach a position close enough to the one of the compact object at orbital phases ∼ 0.0 and ∼ 0.5: First, the lack of superorbital variability at orbital phase ∼ 0.9 (phase bin: 0.83–0.93) followed by a sudden increase in the superorbital variability at orbital phase ∼ 0.0 (phase bin: 0.93–0.03) (Fig. 4.5). Second, the maximum of emission at orbital phase ∼ 0.9 (Fig. 4.6). Third, the behavior of the standard deviation of the magnitude: a monotonically decrease from ∼ 0.0 until ∼ 0.5 orbital phases, followed by a secondary maximum from ∼ 0.5 until ∼ 0.8, and a minimum at ∼ 0.9 (Fig. 4.7). We want to note that Grundstrom et al. (2007)

conducted Hα observations of the gamma-ray binary LS I +61 303 and concluded that the disk radius is smaller than the separation between the optical star and the compact object at periastron. However, regardless of the validity of our proposed physical scenario, such a small disk size probably can not explain the lack of superorbital variability at the orbital bin 0.83–0.93, followed by a sudden increase in the next orbital phase bin, 0.93–0.03.

4.4.2.2 *On the superorbital variability:* $EW_{\mathrm{H}\alpha}$

In Fig. 4.8 we observe the superorbital variability of the $EW_{\mathrm{H}\alpha}$ for different orbital phase bins. From Fig. 4.8 and Table 4.3 we see that the superorbital variability starts to dim close to periastron, and vanishes at orbital phase bin 0.33–0.43. The reduction of superorbital variability after periastron can be interpreted as the attenuation of the $EW_{\mathrm{H}\alpha}$ emission due to the perturbation of the disk by the compact object. Regardless of the poor sampling at the orbital phase bin 0.73–0.83, there seems to be some superorbital variability within that bin. On the other hand, the poor sampling in the orbital phase bin 0.93–0.03 does not allow any inference from that bin. The likely presence of the superorbital variability far from periastron, in contrast with the optical photometry, suggests that the region of the circumstellar disk responsible for the $EW_{\mathrm{H}\alpha}$ emission reaches apastron orbital phases and/or is never fully recovered within an orbital cycle. A very extended disk up to apastron phases is supported by the combination of: an extended disk responsible for the photometric emission up to ~ 0.0 orbital phases (Section 4.4.2.1), and the consideration that the $EW_{\mathrm{H}\alpha}$ traces outermost regions than the optical photometry. A non-recovered disk is supported by the larger orbital variability of the $EW_{\mathrm{H}\alpha}$ (30%) compared with the optical photometric variability (16%), discussed in Section 4.4.1. The wide maximum in the $EW_{\mathrm{H}\alpha}$ light curve (Fig. 4.9), starting at orbital phase ~ 0.5, is both compatible with the extended disk hypothesis, and with the (not necessarily extended)-disk that is never fully recovered but presents its maximum emission at orbital phase ~ 0.5.

4.4.2.3 *On the superorbital variability: a very simple density wave model*

In the following discussion we will assume a density wave propagating azimuthally counter-clockwise within the circumstellar disk (see Fig. 4.11 for reference). For simplicity, we will consider a bimodal density profile: one half of the disk very dense (less prone to perturbations), and the other half less dense (more easily to perturb). This density profile will propagate azimuthally and periodically along time (superorbital phase). Under that hypothesis let us consider 3 different superorbital configurations representative of 3 consecutive superorbital phases:

1. The less dense half of the disk is pointing towards periastron (i.e., left half of the disk, see Fig. 4.11): In this scenario, the circumstellar disk will experience the largest perturbation by the compact object interaction. This will result in the largest drop in the optical photometric and $EW_{\mathrm{H}\alpha}$ flux. In that configuration we expect the largest orbital variability.

2. The less dense half of the disk is placed at the bottom of the disk (see Fig. 4.11): In this scenario, the circumstellar disk will experience a smaller perturbation by the compact object interaction, resulting on average in larger optical photometric and $EW_{\mathrm{H}\alpha}$ flux, compared with the previous configuration. Because the disk recovery will happen latter than in the previous case, there will be a delay in the phase of the maximum. In that configuration we expect smaller orbital variability. Hence: superorbital flux ↑, orbital phase of the maximum ↑, and orbital variability ↓.

3. The less dense half of the disk is pointing towards apastron (i.e., right half of the disk, see Fig. 4.11): In this scenario, the circumstellar disk will experience the smallest perturbation by the compact object interaction. This will result on average in the largest optical and $EW_{\mathrm{H}\alpha}$ flux. Because the disk recovery will happen latter than in the previous case, there will be another delay in the phase of the maximum. In that configuration we expect the smallest orbital variability. Hence: superorbital flux ↑↑, orbital phase of the maximum ↑↑, and orbital variability ↓↓.

From that very simple scenario we expect the following: 1) The superorbital variability of the flux to be correlated with the orbital phase variation of the maximum. 2) The superorbital variability of the flux to be anti-correlated with the orbital variability.

From the optical observations we observe that 1) is fulfilled for both the optical photometry and the $EW_{\mathrm{H}\alpha}$ (see Figs. 4.3 and 4.4). From Fig 4.3-*top* we observe that 2) is fulfilled by the optical photometry: from superorbital phase ~ 0.6 to ~ 0.4, the maximum flux is approximately constant (~ 10.66 mag), and the minimum flux increases from ~ 10.76 mag to ~ 10.72, i.e., the orbital variability decreases. On the other hand, the poor sampling in the last two observational campaigns of the $EW_{\mathrm{H}\alpha}$ (see Fig 4.2) does not allow any firm conclusion on 2).

The delay between the optical photometry and the $EW_{\mathrm{H}\alpha}$ in the superorbital variability of the flux (Fig 4.3) can be understood considering different emitting regions: the intersection between the disk and the compact object is produced at different azimuthal angle (hence at a different superorbital state).

4.4.2.4 *On the superorbital variability: Disk inclination*

The orbital phase lag between the optical photometry and the $EW_{\mathrm{H}\alpha}$ has been suggested as a first hint of a coplanar or quasi-coplanar disk to the orbital plane (Section 4.4.1).

The optical observations suggest an optically emitting disk that extends close to the compact object orbit up to ~ 0.0 and ~ 0.5 orbital phases (Section 4.4.2.1). In that scenario, a non-coplanar (inclined enough) disk would interact with the compact object two times during the same orbital cycle, displaying two minima. However, the optical photometry presents a single minimum (see the light curves in Fig. 4.2-*left* and Fig. 4.6).

In addition, in the non-coplanar scenario, the disk would be partially recovered between the two minima, implying an increase of the emission, and an increase of the superorbital variability as well. Therefore, we would observe an increase in the standard deviation of the magnitude along the orbital phase, as it is a proxy for the superorbital variability (see Section 4.4.2.1). However, in Fig. 4.7 we observe a monotonic decrease in the standard deviation of the magnitude along the orbital phase, as it is expected for a unique and long interaction between the compact object and a (quasi)-coplanar disk. Therefore, the optical observations suggest an extended (quasi)-coplanar circumstellar disk.

4.4.2.5 *On the superorbital variability: Other scenarios*

We shortly discuss two other, a priori, plausible scenarios of the superorbital variability: the shrinking/expanding disk and the precessional disk scenarios.

A disk that produces the photometric superorbital variability modifying the projected emitting area with a period of 1667 d due to its own expansion/contraction or precession, should display superorbital variability regardless of the orbital phase of the compact object. Therefore, these models are unable to explain the lack of superorbital variability at orbital phases 0.83–0.93 (see Fig. 4.5 and Table 4.2). The former scenario was suggested in the past as an explanation of the superorbital variability in the GeV light curves (see Ackermann et al. 2013 and references therein). However, if the disk is precessing, the compact object will unavoidably face different disk configurations, through precession, in different orbital cycles, and one could explain the superorbital variability. Nonetheless, the precession angle responsible for such superorbital variability is restricted to small angles (Section 4.4.2.4).

4.5 CONCLUSIONS

We presented here, for the first time, the optical monitoring of a nearly complete superorbital cycle of the gamma-ray binary LS I +61 303, including contemporaneous optical photometric and $EW_{H\alpha}$ observations.

The optical observations present a superorbital variability of the orbital phase of the maximum, as seen in radio and X-rays, providing evidence of the coupling between the thermal and the non-thermal emission processes in LS I +61 303. The optical photometry presents a superorbital variability of the flux compatible with the 1667 d superorbital period at most of the orbital phases. That variability is not present in the orbital phase bin 0.83–0.93, and re-appears in the next orbital phase bin 0.93–0.03. The $EW_{\mathrm{H}\alpha}$ also presents superorbital variability of the flux compatible with the 1667 d superorbital period for most of the orbital phases. For both, the optical photometry and the $EW_{\mathrm{H}\alpha}$, the superorbital variability is attenuated close to the periastron.

The gamma-ray binary LS I +61 303 presents a temporal dependence on the multi-wavelength orbital variability. The optical photometry (inner disk conditions) always presents a positive lag with respect contemporaneous $EW_{\mathrm{H}\alpha}$ measurements (outer disk conditions; ~ 0.1, ~ 0.1, ~ 0.4, and ~ 0.5 orbital phases, for each of the four observational campaigns, respectively). The $EW_{\mathrm{H}\alpha}$ maximum of emission, of the first and second observational campaigns, occurs at similar orbital phases than non-contemporaneous radio outbursts (which occur outside the binary system), whereas it is delayed by ~ 0.2 and ~ 0.5 orbital phases for the last two observational campaigns, respectively. The photometric maximum lags ~ 0.3 orbital phases with respect X-ray outbursts (non-thermal processes) from the previous superorbital cycle. These lags can be naturally interpreted considering different emitting regions and the complex link between thermal and non-thermal emission phenomena.

The optical photometric variability is interpreted to be caused by the reduction of the projected emitting area of the circumstellar disk by the compact object interaction along the orbit, being the maximum emission when the disk is recovered. The superorbital variability seen in $EW_{\mathrm{H}\alpha}$ suggests a superorbital variability of the circumstellar disk as the origin of the multi-wavelength superorbital variability. The optical observations support a physical scenario where the disk properties are periodically modulated, such as the density wave scenario. The optical observations are not compatible with expanding/shrinking disk or precession-disk models to explain the superorbital variability without accounting for the compact object interaction. However, a very restrictive precessing-disk, involving low precession angles, that interacts with the compact object might explain the superorbital variability.

There are several arguments that favor an optically emitting extended disk from the optical photometry: 1) The lack of superorbital variability at orbital phase ~ 0.9 followed by a sudden increase at orbital phase ~ 0.0. 2) The maximum photometric flux at orbital phase ~ 0.9. 3) And the behavior of the standard deviation of the magnitude along the orbital phase. The extended optically emitting disk would reach a position close enough to the one of the compact object at orbital phases ~ 0.0 and ~ 0.5, implying a disk extending ~ 5 times the periastron distance.

The absence or diminishing of the superorbital variability at orbital phases close to periastron, in the optical photometry and in the $EW_{\mathrm{H}\alpha}$, is explained by a larger perturbation of the disk at those orbital phases, when the compact object is closer to the disk, independent of the superorbital variability.

There are several arguments supporting a (quasi)-coplanar disk: 1) The single minimum in the optical photometric light curve. 2) The orbital phase lag between the optical photometry and the $EW_{\mathrm{H}\alpha}$. 3) And, again, the behavior of the standard deviation of the magnitude along the orbital phase.

Part II

RELATIVISTIC HYDRODYNAMICS

5

RELATIVISTIC HYDRODYNAMICAL SIMULATIONS

The theoretical studies presented in this thesis, of the interaction of relativistic pulsar winds with inhomogeneous stellar winds, are conducted through numerical simulations. These numerical simulations are performed using a finite-difference numerical code that solves the equations of relativistic hydrodynamics for a two dimensional grid. The main objective of this chapter is to introduce the theoretical and technical background needed to understand the numerical simulations presented in Chapter 6 and Appendix B.

In Section 5.1 we show the equations of fluid dynamics, i.e., the Euler equations, and its numerical treatment. In Section 5.2 we present the relativistic equations of fluid dynamics. Last, in Section 5.3 we provide a summary of the steps followed by the numerical code used in the context of this thesis.

5.1 FLUID DYNAMICS

The Euler equations are a system of non-linear hyperbolic equations representing the conservation laws governing the dynamics of an adiabatic an inviscid flow (Toro 1999). The conservation laws are the conservation of mass, the conservation of momentum (or Newton's Second Law), and the conservation of energy. The equations can be expressed using the *physical variables* or the *conserved variables*. The physical (or primitive) variables are the mass-density (hereafter density), ρ, the pressure, p, and the three-velocity components, u, v, and w. On the other hand, the conserved variables (in non-relativistic hydrodynamics in Cartesian coordinates) are the density, ρ, the momentum components, ρu, ρv, and ρw, and the total energy per unit of volume, E, defined as

$$E = \rho\frac{1}{2}(u^2 + v^2 + w^2) + \rho\epsilon, \tag{5.1}$$

being ϵ the specific internal energy (per unit of mass). Then, the Euler equations in a conservation form are:

$$\begin{cases} \rho_t + (\rho u)_x + (\rho v)_y + (\rho w)_z = 0 \\ (\rho u)_t + (\rho u^2 + p)_x + (\rho u v)_y + (\rho u w)_z = 0 \\ (\rho v)_t + (\rho u v)_x + (\rho v^2 + p)_y + (\rho v w)_z = 0 \\ (\rho w)_t + (\rho u w)_x + (\rho v w)_y + (\rho w^2 + p)_z = 0 \\ E_t + [u(E + p)]_x + [v(E + p)]_y + [w(E + p)]_z = 0 \end{cases} \tag{5.2}$$

denoting the subscripted variable the partial derivative with respect that variable.

Now, let us consider the 1-dimensional case as it is more simple and illustrative. Being **U** the vector of conserved variables, and **F** the flux vector, both defined as

$$\mathbf{U} = \begin{bmatrix} \rho \\ \rho u \\ E \end{bmatrix}, \quad \mathbf{F} = \begin{bmatrix} \rho u \\ \rho u^2 + p \\ u(E + p) \end{bmatrix}, \tag{5.3}$$

the Euler equations in 1-D result in

$$\mathbf{U}_t + \mathbf{F}(\mathbf{U})_x = 0. \tag{5.4}$$

The previous equation, with an initial condition defined as

$$\mathbf{U}(x, t = 0) = \begin{cases} \mathbf{U}_L & \text{if} \quad x < 0, \\ \mathbf{U}_R & \text{if} \quad x > 0, \end{cases} \tag{5.5}$$

is called the *Riemann problem*. This problem can be solved numerically discretizing the state vector, **U**, within computational cells and computing the temporal evolution as

$$\mathbf{U}_i^{n+1} = \mathbf{U}_i^n + \frac{\Delta t}{\Delta x}[\mathbf{F}_{i-\frac{1}{2}} - \mathbf{F}_{i+\frac{1}{2}}], \tag{5.6}$$

where n denotes the time step and i the discretized cell. The intercell fluxes, $F_{i\pm\frac{1}{2}}$, may be calculated using the so called *Riemann Solvers* (see Toro 1999 and references therein).

5.2 RELATIVISTIC FLUID DYNAMICS

The equations describing the dynamics of a relativistic fluid are the relativistic Euler equations (see, e.g., Martí & Müller 2003). These equations are provided by the conservation of the stress-energy tensor and mass:

$$\begin{cases} \nabla_\mu T^{\mu\nu} = 0, \\ \nabla_\mu(\rho u^\mu) = 0, \quad \mu, \nu = 0, 1, 2, 3, \end{cases} \tag{5.7}$$

considering a perfect fluid, then the stress-energy tensor is

$$T^{\mu\nu} = \rho h u^\mu u^\nu + p g^{\mu\nu}, \tag{5.8}$$

being ρ the proper rest mass density, u^μ the 4-velocity, p the pressure, $g^{\mu\nu}$ the Minkowski metric tensor with space-positive signature, and h the specific enthalpy given by

$$h = 1 + \frac{\epsilon}{c^2} + \frac{p}{\rho c^2}, \tag{5.9}$$

where ϵ is the specific internal energy (per unit of mass), and c is the speed of light. As in the non-relativistic Euler equations, Eq. 5.7 can be written using the vector of conserved variables (or state vector) **U**, and the flux vector **F**, as

$$\mathbf{U}_t + \mathbf{F}^i(\mathbf{U})_{x^i} = 0, \quad i = 1, 2, 3, \tag{5.10}$$

where the vector of the conserved variables and the vector flux are

$$\mathbf{U} = \begin{bmatrix} D \\ S^1 \\ S^2 \\ S^3 \\ \tau \end{bmatrix}, \quad \mathbf{F}^i = \begin{bmatrix} Dv^i \\ S^1 v^i + p\delta^{1i} \\ S^2 v^i + p\delta^{2i} \\ S^3 v^i + p\delta^{3i} \\ S^i - Dv^i \end{bmatrix}, \tag{5.11}$$

being all the conserved variables measured in the *laboratory reference frame*, and defined using the physical variables (density, ρ, pressure, p, and i_{th} velocity component, v^i) in the *local rest frame*. The conserved quantities are: the *relativistic rest mass density*, D, the i_{th} component of the *relativistic momentum density*, S^i, and the *relativistic energy density*, τ, given by

$$D = \rho W \tag{5.12}$$

$$S^i = \rho h W^2 v^i \tag{5.13}$$

$$\tau = \rho h W^2 c^2 - p - \rho W c^2, \tag{5.14}$$

with W the Lorentz factor of the flow, defined as

$$W = \frac{1}{\sqrt{1-\beta^2}}. \tag{5.15}$$

The 3-velocity of the fluid in the laboratory reference frame is therefore

$$v^i = \frac{u^i}{W}. \tag{5.16}$$

From Eqs. 5.11–5.14, the vector of conserved variables and the flux vector for $i = 1$ are

$$\mathbf{U} = \begin{bmatrix} \rho W \\ \rho h W^2 v^1 \\ \rho h W^2 v^2 \\ \rho h W^2 v^3 \\ \rho h W^2 c^2 - p - \rho W c^2 \end{bmatrix}, \quad \mathbf{F}^1 = \begin{bmatrix} \rho W v^1 \\ \rho h W^2 v^1 v^1 + p \\ \rho h W^2 v^2 v^1 \\ \rho h W^2 v^3 v^1 \\ \rho h W^2 c^2 v^1 - \rho W c^2 v^1 \end{bmatrix}, \tag{5.17}$$

The system of Eqs. 5.10 is closed by an equation of state, and it does not have an analytical solution. Therefore, numerical methods are required to solve the Euler equations (Martí & Müller 2003; Perucho 2005).

5.3 THE NUMERICAL CODE

The simulations presented in this thesis have been performed using a finite-difference code that solves the two-dimensional equations of relativistic hydrodynamics in conservation form (Martí et al. 1997). The state vector is discretized within computational cells, and its temporal evolution is determined by the flux balance equation

$$\frac{d\mathbf{U}_{i,j,k}}{dt} = -\frac{1}{\Delta x}\left(\mathbf{F}^{x}_{i+\frac{1}{2},j,k} - \mathbf{F}^{x}_{i-\frac{1}{2},j,k}\right) - \frac{1}{\Delta y}\left(\mathbf{F}^{y}_{i,j+\frac{1}{2},k} - \mathbf{F}^{y}_{i,j-\frac{1}{2},k}\right) - \frac{1}{\Delta z}\left(\mathbf{F}^{z}_{i,j,k+\frac{1}{2}} - \mathbf{F}^{z}_{i,j,k-\frac{1}{2}}\right) + \mathbf{S}_{i,j,k}, \quad (5.18)$$

where the i and j indices correspond to the mean value of the (i_{th}, j_{th}) cell with respect to the x and y coordinate system, respectively, while the $\frac{1}{2}$ indices denote the values at the cell interfaces. The quantity $\mathbf{S}_{i,j,k}$ accounts for forces/geometrical terms (e.g., Perucho 2005). The intercell fluxes are computed using an approximate Riemann solver (see Donat & Marquina 1996; Font et al. 1994; Donat et al. 1998).

In order to obtain the intercell physical values required to compute the intercell fluxes, the algorithm applies a conservative monotonic parabolic reconstruction method (PPM; see Woodward & Colella 1984; Martí & Müller 1996; Mignone et al. 2005). Because the conserved variables are coupled through the Lorentz factor, the primitive variables cannot be derived analytically from the conserved ones. The numerical code uses then the Newton-Raphson algorithm to recover the physical variables (see Aloy 1999). The time integration of Eq. 5.18 is performed using a Runge-Kutta method. The code is parallelized using Open Message Passing (OpenMP) (Perucho 2005); see also Martí & Müller (2003).

6

SIMULATIONS OF THE INTERACTION OF RELATIVISTIC PULSAR WINDS WITH INHOMOGENEOUS STELLAR WINDS

The non-thermal high-energy emission from gamma-ray binaries hosting a massive star and a young pulsar depends on the dynamical effects of the collision of the stellar wind and the relativistic pulsar wind. For inhomogeneous stellar winds, the two-wind interaction region might suffer the impact of stellar wind inhomogeneities or clumps, modifying its dynamics and hence its radiative output.

In this chapter we present the results of axisymmetric RHD simulations of the interaction of a relativistic wind from a young pulsar with an inhomogeneous stellar wind. This chapter has been adapted from the work published in Paredes-Fortuny et al. (2015a), which was conducted during the context of this thesis.

6.1 INTRODUCTION

In binaries consisting of a massive star and a young non-accreting pulsar, the relativistic wind of the pulsar interacts with the non-relativistic wind of the stellar companion. This can result in efficient particle acceleration and in the production of non-thermal radiation, from radio to gamma rays. At present, PSR B1259−63 has been confirmed as a member of this class of objects, and there are several other high-mass binaries hosting a compact object whose nature is still unknown and may belong to this class as well (e.g., Dubus 2013; Paredes et al. 2013).

The properties of the non-thermal radiation in high-mass binaries hosting a non-accreting pulsar are determined to a large extent by the dynamics of the two-wind interaction structure. To study different aspects of this structure and its evolution along the orbit, heavy and detailed numerical simulations have been performed. Romero et al. (2007) carried out non-relativistic, smoothed particle hydrodynamic (SPH) simulations in three dimensions (3D) to study the orbital evolution of a hypothetic two-wind interaction region in LS I +61 303. Bogovalov et al. (2008) studied numerically the collision of the pulsar and the stellar wind in PSR B1259−63, treating the flows as laminar fluids by relativistic hydrodynamical simulations in two dimensions (2D). For the same system, Okazaki et al. (2011) and Takata et al. (2012) performed 3D SPH non-relativistic simulations to study the tidal and wind interactions between the pulsar and the decretion disc of the Be star, and Bogovalov et al. (2012) studied the collision of a magnetized and an anisotropic pulsar wind and the stellar wind adopting the same geometry and using a similar treatment to that adopted in Bogovalov et al. (2008). Lamberts et al. (2012b) performed non-relativistic hydrodynamical simulations in planar geometry of the two-wind interaction structure for several orbits on large scales. Lamberts et al. (2012a) and Lamberts et al. (2013) performed 2D RHD simulations in planar geometry of the interaction between the pulsar and the stellar wind on the scales of the binary system. Finally, Bosch-Ramon et al. (2012, 2015) performed 2D RHD simulations in planar geometry, and 3D RHD simulations, aimed at studying the interaction between the stellar and pulsar winds on scales at which the orbital motion is important.

Some relevant conclusions of the numerical work done up to now are the importance of instabilities, in particular the Rayleigh-Taylor (RT) and Kelvin-Helmholtz (KH)[1] instabilities, in the spatial and temporal properties of the two-wind interaction structure on both small and large scales, the occurrence of shocked-flow re-acceleration, the impact of orbital motion through lateral, strong shocks, the effective mixing of the shocked winds downstream of the flow, the strong effects of the pulsar wind ram pressure on Be discs, and the relatively minor role of pulsar wind anisotropies and magnetic fields. However, all the simulations of binaries hosting a pulsar considered smooth winds, while the stellar wind is expected to be inhomogeneous, in particular for earlier spectral types (Lucy & Solomon 1970). The wind inhomogeneities (clumps hereafter) are expected to play an important role in the structure of the two-wind interaction region, and therefore in the non-thermal emission. The origin of these clumps can be explained by different mechanisms depending on their scale, either the stellar surface at the wind formation region, or a circumstellar disc in the Be system. For instance, the impact of a fragment of a Be star disc on the two-wind interaction region has been proposed to cause the GeV flare observed in the gamma-ray binary PSR B1259−63 (Abdo et al. 2011; Chernyakova et al. 2014). In addition, some sort of wind clumping could explain short flares on scales of seconds to hours found in the X-ray light curves of LS 5039 and LS I +61 303 (e.g., Bosch-Ramon et al. 2005; Paredes et al. 2007; Smith et al. 2009; Li et al. 2011). The clump-pulsar wind interaction problem has previously been studied analytically (see Bosch-Ramon 2013), but numerical calculations of the interaction between an inhomogeneous stellar wind and a relativistic pulsar wind have not been conducted yet.

---

[1] RT: instability developed in the contact surface between two fluids of different densities, with the lightest fluid exerting a force on and accelerating the densest one. KH: instability developed in the contact surface between two fluids of different parallel velocities (see Chandrasekhar 1961).

In this work, we present 2D axisymmetric RHD simulations of the interaction between a wind clump and a relativistic pulsar wind. Orbital motion has not been accounted for because of the axisymmetric nature of the simulations; given the small spatial and temporal scales considered, this is a reasonable approximation. We simulated clumps with different sizes and densities to study the global variations induced in the two-wind interaction structure, as well as on the evolution of the clumps under the impact of the pulsar wind.

We note that this is the first time that relativistic simulations are carried out in a more realistic set-up, with axisymmetry along the two-star line, without suppressing the development of instabilities. The numerical results are compared with the analytical results found in Bosch-Ramon (2013). The chapter is structured as follows: in Sect. 6.2 we describe the physical framework: the two-wind interaction region, the origin of the clumps in the winds of massive stars, and the analytical equations; in Sect. 6.3, we describe the numerical simulations: the numerical set-up and the obtained results; finally, a discussion and the conclusions can be found in Sects. 6.4 and 6.5.

6.2 PHYSICAL FRAMEWORK

The collision between the stellar wind and the wind from the young pulsar creates a shock structure bow-shaped towards the wind with the lower momentum rate. The contact discontinuity is located where the ram pressure of the two winds balances. As discussed in Bosch-Ramon (2013), the presence of clumps can significantly distort the overall interaction structure, although their dynamical impact is determined by their size and mass (see, e.g., Pittard 2007, for a similar non-relativistic scenario). Winds formed by small and light clumps will behave as uniform winds, while massive clumps will tend to come less frequently and be more damaging for the global stability of the interaction region (see Perucho & Bosch-Ramon 2012 for the effect of an inhomogeneous wind on a high-mass microquasar jet). A sketch of the physical scenario is shown in Fig. 6.1.

The instability of the line-driving mechanism in the inner wind is thought to be an important source of clumps in the wind structure of hot stars of spectral types O and B (Lucy & Solomon 1970). Runacres & Owocki (2002) suggested that the outer evolution of the inhomogeneous wind can be approximated as a pure gas dynamical problem, and the stellar wind clumps initiated close to the star can survive up to long distances ($d \sim 1000\ R_{\odot}$). Moffat (2008) suggested that all hot stellar winds are likely to be inhomogeneous because of radiative instabilities, with a multi-scale distribution of masses and sizes. Therefore, considering the outer wind evolution as a gas dynamical problem, the clumps could expand with the wind flow and large clumps could reach the interaction region between the stellar and the pulsar wind. However, the relatively small initial sizes ($\sim 0.01\ R_{*}$), and limitations on the clump growth

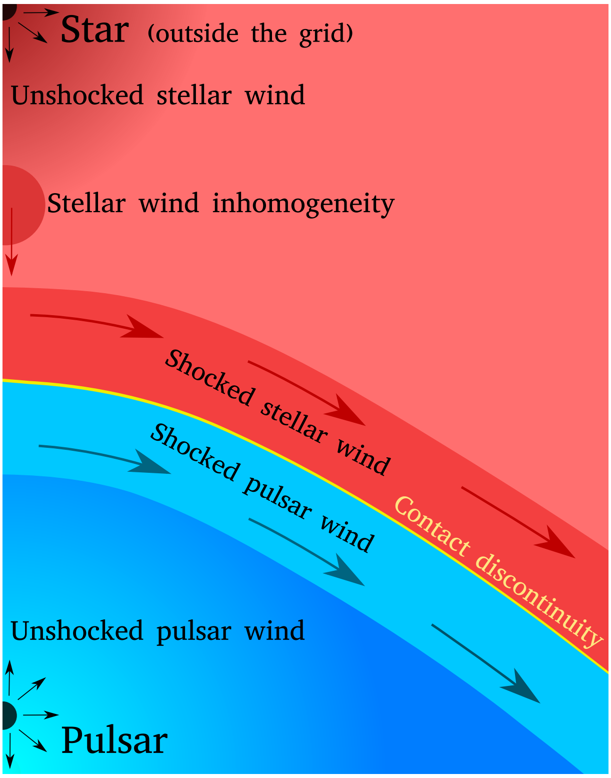
Star (outside the grid)
Unshocked stellar wind
Stellar wind inhomogeneity
Shocked stellar wind
Shocked pulsar wind
Contact discontinuity
Unshocked pulsar wind
Pulsar

Figure 6.1: Cartoon representing a density map of the physical scenario: an inhomogeneous stellar wind interacts with the relativistic pulsar wind. The shocked stellar wind and the shocked pulsar wind are separated by a contact discontinuity. The distances are not to scale. The simulations presented in this chapter only considered a stellar wind with one clump centered at the axis joining the two stars.

(which can be parameterized as $R_c = R_{c_0}\,(d/R_*)^{\alpha}$, with $\alpha \leqslant 1$ and R_{c_0} being the initial clump radius), could prevent the formation of clumps as large as $R_c \sim R_*$, for instance, which is required for the strongest variations of the two-wind interaction structure (see Bosch-Ramon 2013, and references there in). Typical massive star radii are $R_* \sim 10\,R_\odot$.

Large clumps different from those related to radiative instabilities may be found in the stellar wind. For instance, early-type stars known as Be stars present a decretion disc formed by material ejected from the stellar equator by rapid rotation (Hanuschik 1996). The truncation of this disc, either caused by tidal forces or by direct pulsar wind ram pressure (see Okazaki et al. 2011), could explain the presence of large clumps in the stellar wind formed by chunks of disc. This possibility has been considered for instance to explain the GeV flare detected from the gamma-ray binary PSR B1259−63 by Chernyakova et al. (2014) (see Sect. 6.4.2.1). Other types of large-scale structures in the stellar wind, of size of the order of the stellar radius, have also been inferred from the observed discrete absorption components (DACs) in the UV (e.g., Kaper et al. 1997). The appearance of DACs can be interpreted as co-rotating dense structures produced at the stellar surface and extending several tens of stellar radii (e.g., Lobel 2008), and can be attributed to the dynamical effects of rotation, magnetic fields, or non-radial pulsations (Cranmer & Owocki 1996). The arrival of any of those structures at the two-wind interaction region should modify the latter in space and time.

Bosch-Ramon (2013) developed an analytical model for the two-wind interaction dynamics accounting for the lifetime of clumps under the pulsar-wind impact. It was concluded that for a clump radius $R_c \ll \chi^{-1/2}\Delta R$, being ΔR the thickness of the two-wind interaction region and $\chi = \rho_c/\rho_w$ the density contrast between the clump density and the wind density, the clump is destroyed and deflected by the shocked wind medium before crossing the two-wind interaction region. Otherwise, for R_c approaching $\chi^{-1/2}\Delta R$ or larger, the clump will penetrate into the unshocked pulsar wind. When R and R' are the initial and final distances between the pulsar and the contact discontinuity, following Bosch-Ramon (2013), this approximate relation applies

$$R' \sim R - \chi^{1/2} R_c \quad (\text{where } R' > 0\,), \tag{6.1}$$

which for $R_c \sim R'$ implies

$$R_c \sim R' \sim \frac{R}{\left(1 + \chi^{1/2}\right)}\,. \tag{6.2}$$

The simulations presented here are intended to investigate in detail the dynamical consequences of the presence of clumps in the stellar wind. Below we compare analytical estimates with numerical results.

6.3 NUMERICAL SIMULATIONS

6.3.1 *Numerical set-up*

The simulations were performed using a finite-difference code based on a high-resolution shock-capturing scheme that solves the equations of relativistic hydrodynamics in two dimensions in a conservation form (Martí et al. 1997). The code is parallelized using OpenMP (Perucho 2005). The simulations were run in a workstation with two Intel(R) Xeon(R) CPU E5-2643 processors (3.30 GHz, 4 × 2 cores, with two threads for each core) and four modules of 4096 MB of memory (DDR3 at 1600 MHz).

We adopted an ideal relativistic gas without a magnetic field, one particle species, and a polytropic index of $\gamma = 1.444$, intermediate between a non-relativistic (stellar wind) and a relativistic (pulsar wind) index. The physical size of the domain is $r \in [0, 30\ a]$ and $z \in [0, 50\ a]$, where $a = 8 \times 10^{10}$ cm. The adopted resolution is 150×250 cells. The pulsar is located at $(r, z) = (0, 5\ a)$, and the star at $(r, z) = (0, 60\ a)$, outside the simulated grid. This yields a pulsar-star separation of $d = 4.4 \times 10^{12}$ cm. The typical orbital separation distances in gamma-ray binaries are $\sim 10^{13}$ cm (see, e.g., Dubus 2013, and references therein).

The initial conditions of the simulation were computed in spherical coordinates assuming adiabatic gas radial propagation and solving the

Bernoulli equation for the pulsar and stellar winds. The initial two-wind separation point is derived as the approximate location where the on-axis wind ram pressures become equal ($z = 22\ a$).

The chosen physical parameters of the pulsar wind, given at a distance $r = a$ with respect to the pulsar center, are the total luminosity $L_{\rm sd} = 10^{37}$ erg s^{-1}, the Lorentz factor $\Gamma = 5$, and the specific internal energy $\epsilon_{\rm pw} = 9.0 \times 10^{19}$ erg g^{-1}. As a result of resolution limitations, the adopted Lorentz factor is smaller than expected in pulsar winds, $\Gamma \sim 10^4$–10^6 (see Khangulyan et al. 2012; Aharonian et al. 2012, and references therein), but high enough to capture important relativistic effects (see the discussion in Bosch-Ramon et al. 2012). For the stellar wind, the physical parameters, given at a distance $r = a$ with respect to the star center, are a mass-loss rate $\dot{M} = 10^{-7}\ M_\odot$ yr^{-1}, a radial velocity $v_{\rm sw} = 3000$ km s^{-1}, and a specific internal energy $\epsilon_{\rm sw} = 1.8 \times 10^{15}$ erg g^{-1}. The derived pulsar wind and stellar wind densities, given at the same distances, are $\rho_{\rm pw} = 1.99 \times 10^{-19}$ g cm^{-3} and $\rho_{\rm sw} = 2.68 \times 10^{-13}$ g cm^{-3}, respectively. The values of $L_{\rm sd}$, $\dot{M}$ and $v_{\rm sw}$ were chosen as representative values of gamma-ray binaries hosting a pulsar because $L_{\rm sd}$ is to be high enough to power the gamma-ray emission, and the stellar wind properties correspond to those of an OB star. All these parameters are summarized in Tables 6.1 and 6.2.

The previous physical values lead to a pulsar-to-stellar wind thrust ratio of

$$\eta = \frac{F_{\rm pw} S_{\rm pw}}{F_{\rm sw} S_{\rm sw}} = \frac{\left(\rho_{\rm pw} \Gamma^2 v_{\rm pw}^2 h_{\rm pw} + p_{\rm pw}\right) S_{\rm pw}}{\dot{M} v_{\rm sw} + p_{\rm sw} S_{\rm sw}} \approx \frac{L_{\rm sd}}{\dot{M} v_{\rm sw} c} \sim 0.2, \qquad (6.3)$$

where $F_{\rm pw}$ ($F_{\rm sw}$) is the momentum flux of the pulsar wind (stellar wind), $S_{\rm pw}$ ($S_{\rm sw}$) the spherical surface at a distance $r = a$ with respect to the pulsar (star), $h_{\rm pw}$ the specific enthalpy of the pulsar wind given by $h_{\rm pw} = 1 + \frac{\epsilon_{\rm pw}}{c^2} + \frac{p_{\rm pw}}{\rho_{\rm pw} c^2}$, and $p_{\rm pw/sw}$ the pressure of the pulsar/stellar wind given by $p_{\rm pw/sw} = (\gamma - 1)\, \rho_{\rm pw/sw} \epsilon_{\rm pw/sw}$.

The pulsar wind is introduced by defining an injector with the mentioned properties and radius $3\ a$ (2.4×10^{11} cm; 15 cells) as a boundary condition, and the stellar wind is injected according to its characterization at the upper boundary of the grid. The lower and right boundaries

Table 6.1: Simulation parameters. Polytropic index γ, density unit ρ_0, distance unit a, physical r grid size l_r, physical z grid size l_z, number of cells in the r axis n_r, and number of cells in the z axis n_z.

Parameter	Value
γ	1.444
ρ_0	22.5×10^{-22} g cm^{-3}
a	8×10^{10} cm
l_r	30 a (2.4×10^{12} cm)
l_z	50 a (4.0×10^{12} cm)
n_r	150
n_z	250

of the grid are set to outflow, while the left boundary of the grid is set to reflection.

The pulsar wind is injected with a Lorentz factor of 5, but because of adiabatic propagation, it reaches Lorentz factors of ~ 6 before termination.

The stellar wind clumps are introduced at $(r, z) = (0, 33\ a)$ after the steady state is reached. The clumps are characterized by their radius R_c and their density contrast χ with respect to the average stellar wind value at their location. We present here the results for four different cases: $\chi = 10$ and $R_c = 1\ a$, $2.5\ a$, $5\ a$ and $\chi = 30$ and $R_c = 1\ a$, corresponding to different degrees of wind inhomogeneity, from modest $\chi = 10$ and $R_c = 1\ a$ to rather high $\chi = 10$ (30) and $R_c = 5$ (1) a.

The axisymmetric nature of the simulations, in particular the reflection boundary conditions, the presence of a coordinate singularity, plus the concentration of fluxes, all at $r = 0$, lead to the generation of perturbations that quickly grow, posing difficulties to achieve a steady state. This effect makes the simulation also quite sensitive to the initial conditions, and the initial two-wind contact discontinuity has to be carefully chosen so as not to enhance the axis perturbations further. In this context, the modest resolution of most of the simulations and the pulsar

Table 6.2: Pulsar and stellar parameters in code and CGS units. Density ρ, specific internal energy ϵ, and wind velocity v at a distance $r = a$ with respect to the pulsar and star centers located at (r_0, z_0).

Parameter	Pulsar wind	Stellar wind
ρ	$88.45\ \rho_0$	$1.19 \times 10^8\ \rho_0$
	$(1.99 \times 10^{-19}$ g cm$^{-3})$	$(2.68 \times 10^{-13}$ g cm$^{-3})$
ϵ	$0.1\ c^2$	$2.0 \times 10^{-6}\ c^2$
	$(9 \times 10^{19}$ erg g$^{-1})$	$(1.8 \times 10^{15}$ erg g$^{-1})$
v	$0.9798\ c$	$0.01\ c$
	$(2.94 \times 10^{10}$ cm s$^{-1})$	$(3 \times 10^8$ cm s$^{-1})$
(r_0, z_0)	$(0, 5\ a)$	$(0, 60\ a)$
	$(0, 4 \times 10^{11}$ cm$)$	$(0, 4.8 \times 10^{12}$ cm$)$

wind Lorentz factor adopted were chosen to stabilize the solution of the calculations through a larger numerical dissipation and moderate wind density contrast. Given the fast growth of any perturbation (numerical or physical) in the simulated problem (as explained below), higher resolutions will enhance (as also shown below) the instability of the simulated structures through the penetration of small fragments of stellar wind material into the pulsar wind region. On the other hand, higher Lorentz factors would have enhanced the wind density contrast and thereby the instability growth rate. Finally, the grid size was also limited to prevent the instabilities from fully disrupting the two-wind interaction structure within the simulated region. With our resolution, larger grid sizes would have given enough time to the instabilities to develop and grow towards the downstream edge of the grid. The resulting structures would be similar to those found in the higher resolution simulations also presented in this work, and would also lead to the collapse of the two-wind interaction region. Albeit small, the grid size does not significantly affect the hydrodynamics within as the flow is supersonic at the outflow boundaries. We remark that because the clump is the strongest dynamical factor, its impact can be studied neglecting the role of numerical perturbations on the axis after a (quasi-)steady state has been reached.

6.3.2 *Results*

Figure 6.2 shows the density map of the simulated flow in the (quasi-)steady state at $t = 58000$ s. The shock structure is bow-shaped towards the pulsar, with the contact discontinuity at $\sim 18\ a$ from the pulsar. The thickness of the shocked two-wind region is $\sim 8\ a$ on the simulation axis. After being shocked, winds are accelerated side-wards because of the strong pressure gradient in the downstream region, as pointed out in Bogovalov et al. (2008). This is seen in the velocity maps presented in this section, for which the two-wind interaction structure has not yet been affected by the clump arrival. Because of this flow re-acceleration, the ratio of the momentum-flux to pressure shows that the flow becomes supersonic at the boundaries.

These axisymmetric simulations are quite sensitive to the initial conditions, and in particular, reaching steady state is highly dependent on the initial set-up of the simulation. It is still an open question, supported though by recent low-resolution 3D simulations (Bosch-Ramon et al. 2015), to which extent this sensitivity to the initial set-up is caused by the geometry of the grid. Nevertheless, it is expected that instabilities quickly grow if perturbations are present, as shown by planar coordinate relativistic simulations (Bosch-Ramon et al. 2012; Lamberts et al. 2013). In the present simulations, the conditions at the axis induce perturbations there that grow under the RT instability. These perturbations are then amplified by the KH instability as the flow propagates along the contact discontinuity. For grid sizes larger than $30\ a$ in the r direction, the structures resulting from instability growth can reach deep into the pulsar wind, eventually disrupting the two-wind interaction region and filling the pulsar vicinity with shocked material. For small grids, on the other hand, these structures are advected out of the grid before it happens. For a fixed η, the RT and KH instabilities grow faster for faster (and lighter) pulsar winds, which implies a stronger wind density con-

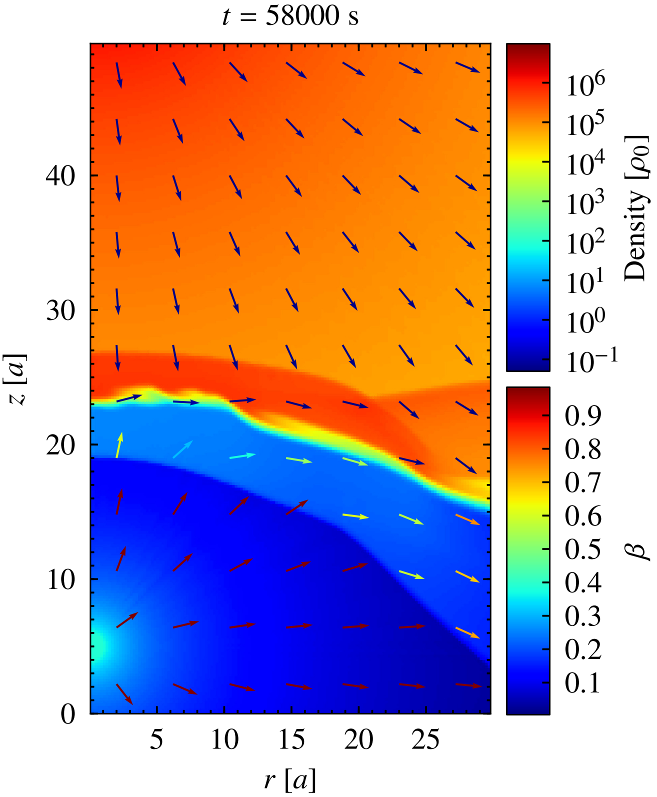

Figure 6.2: Density distribution by color at time $t = 58000$ s. The colored arrows represent the three-velocity at different locations ($\beta = v/c$). The axes units are $a = 8 \times 10^{10}$ cm. The density units are $\rho_0 = 22.5 \times 10^{-22}$ g cm^{-3}. The pulsar and the star are located at $(r, z) = (0, 5\ a)$ and $(r, z) = (0, 60\ a)$, respectively. The same units are used in all the figures.

trast and thus a more unstable contact discontinuity. A Lorentz factor of $\Gamma \sim 5$–6 was adopted as a compromise: a rather relativistic flow with tenable instability-growth rates.

Despite numerical perturbations introducing a degree of deformation in the global structure of the two-wind collision region, as shown by the wave at $r \sim 20 - 30$ a in the two-wind interaction region in Fig. 6.2, the opening angle and width of the shocked wind zone are similar to those found in Bogovalov et al. (2008, 2012). Those simulations were similar to ours given their axisymmetry, although the simulated flows were laminar there.

Figures 6.3, 6.4, 6.5, and 6.6 show the density map evolution for the clumps characterized by $\chi = 10$ and $R_c = 1$ a, 2.5 a, 5 a, and $\chi = 30$ and $R_c = 1$ a, respectively. The times of the map snapshots were chosen such that the images are illustrative of the structure evolution. The bigger clumps, characterized by $\chi = 10$ and $R_c = 2.5$ a and $R_c = 5$ a, and the smallest but densest one, with $\chi = 30$ and $R_c = 1$ a, strongly perturb the two-wind interaction region, pushing the contact discontinuity to less than a half its initial distance (see Fig. 6.2) to the pulsar (see Figs. 6.4, 6.5, and 6.6, respectively).

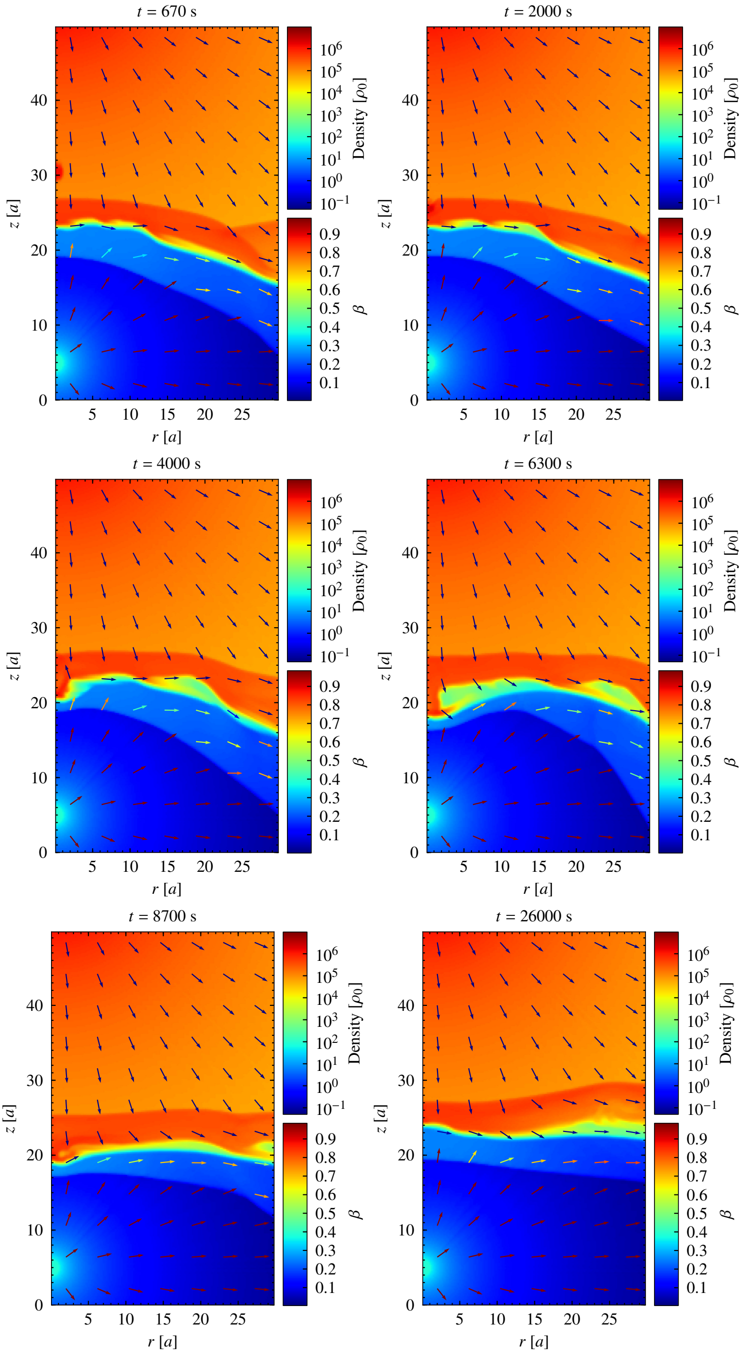

Figure 6.3: Density distribution by color for the case with clump parameters $\chi = 10$ and $R_c = 1\ a$ for the times shown at the top of each plot. The remaining plot properties are the same as those of Fig. 6.2.

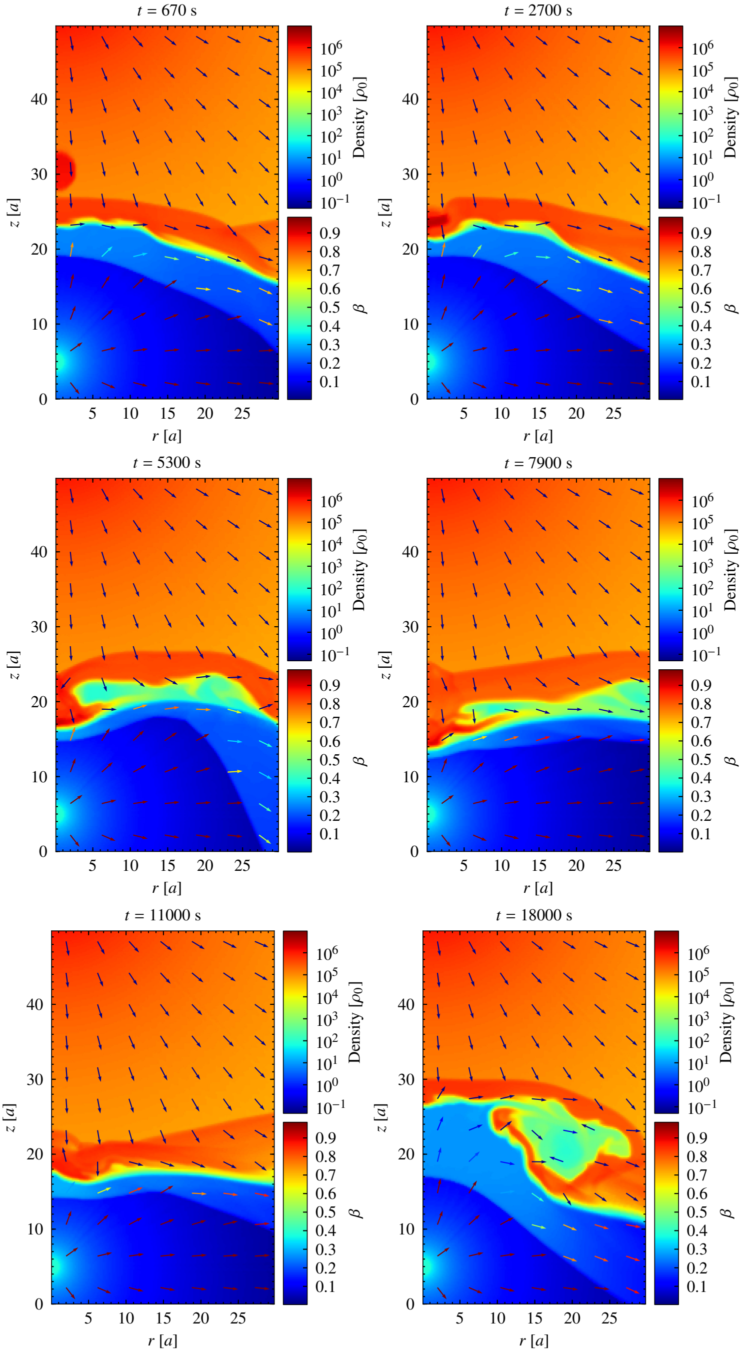

Figure 6.4: Density distribution by color for the case with clump parameters $\chi = 10$ and $R_c = 2.5\ a$ for the times shown at the top of each plot. The remaining plot properties are the same as those of Fig. 6.2.

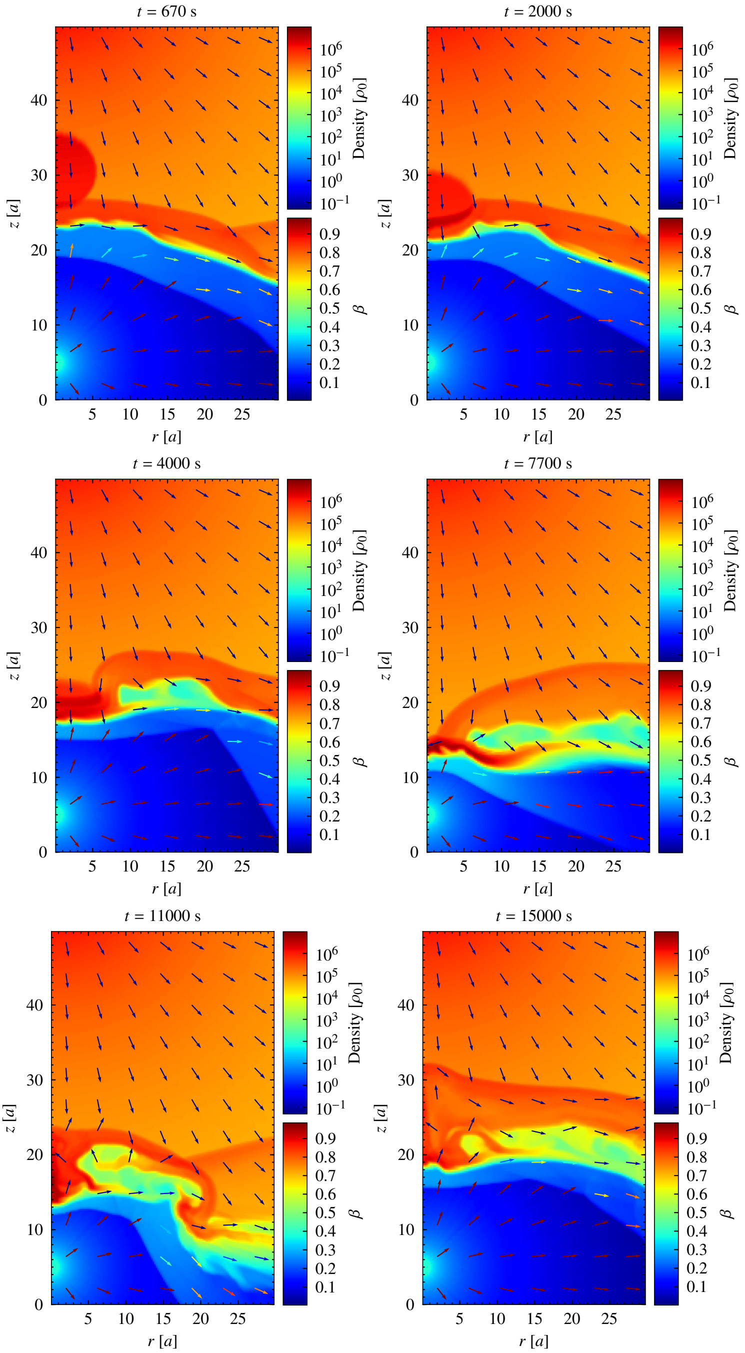

Figure 6.5: Density distribution by color for the case with clump parameters $\chi = 10$ and $R_c = 5\ a$ for the times shown at the top of each plot. The remaining plot properties are the same as those of Fig. 6.2.

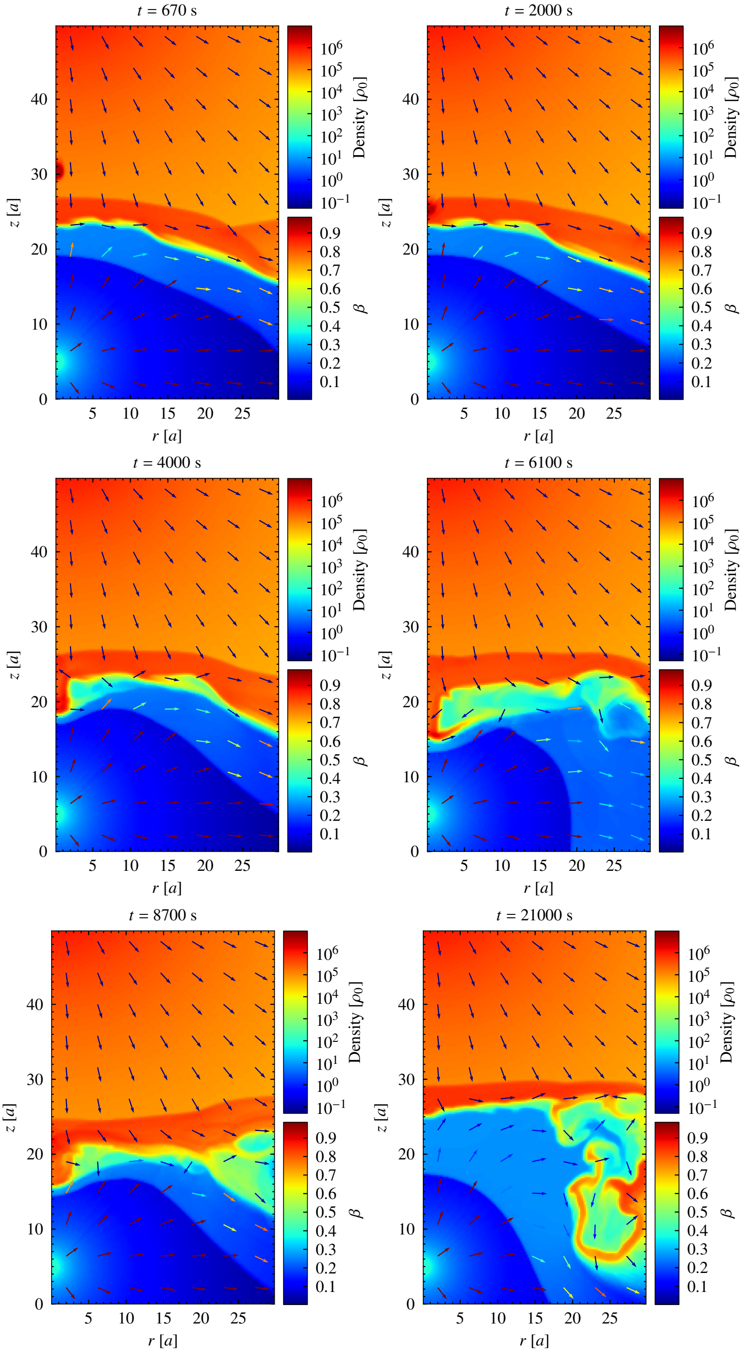

t = 670 s

t = 2000 s

t = 4000 s

t = 6100 s

t = 8700 s

t = 21000 s

Figure 6.6: Density distribution by color for the case with clump parameters $\chi = 30$ and $R_c = 1\ a$ for the times shown at the top of each plot. The remaining plot properties are the same as those of Fig. 6.2.

We now focus on a clump with $\chi = 10$ and $R_c = 2.5\ a$, as it is illustrative of the strong impact of a clump of intermediate size. For this case, we also show Figs. 6.7, 6.8, 6.9, 6.10, and 6.11, which display the evolution of the clump in the density map, the tracer map (1 for the clump material and 0 otherwise), the pressure map, the map of momentum flux over pressure (greater than a few for a super-sonic flow), and the map of β. These figures show how the two-wind interaction region is pushed by the clump, until the contact discontinuity reaches a minimum distance to the pulsar at $R'_{\mathrm{num}} \approx 8.5\ a$ ($R'_{\mathrm{num}} \approx 7.5\ a$ for the termination shock). After that, the clump starts to be pushed backwards by the pulsar wind, is shocked, and decelerates, eventually disrupting, with its fragments driven away from the simulation axis by the shocked flow. All this is clearly seen in the density maps (Figs. 6.4 and 6.7), and in the tracer (Fig. 6.8). In addition, Figs. 6.9, 6.10 and 6.11 provide information on the presence of shocks, apparent as sudden increases in pressure or drops in the ratio of momentum-flux to pressure, and relevant for particle acceleration; flow re-acceleration, important for non-radiative cooling, flow relativistic motion, and flow-to-sound-speed relation; and flow speed and direction downstream of the shocks, determining Doppler effects on the flow emission. Equivalent images to Figs. 6.7, 6.8, 6.9, 6.10, and 6.11 for the other three simulated clump cases are available in the online material of the Paredes-Fortuny et al. (2015a) publication. In all the simulations, a $t = 0$ is assigned to the steady state plus a clump at the initial position.

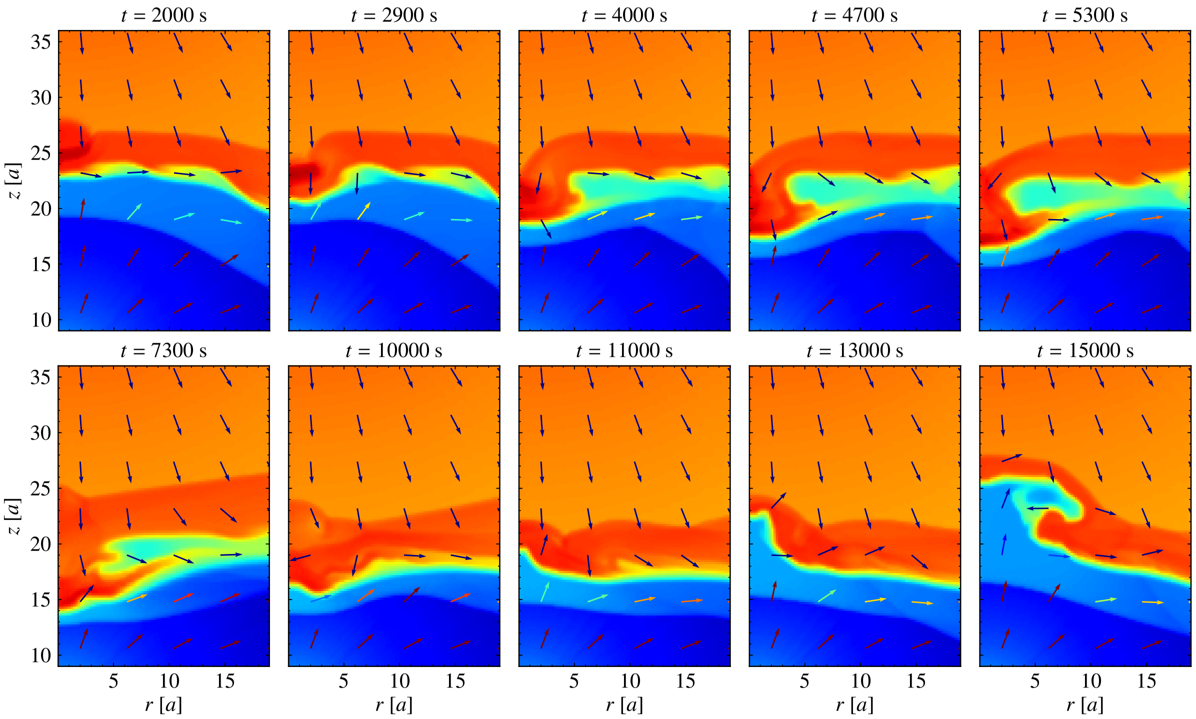

Figure 6.7: Zoom-in of the density distribution by color for the case with clump parameters $\chi = 10$ and $R_c = 2.5\ a$ for the times shown at the top of each plot. The remaining plot properties are the same as those of Fig. 6.4. The pulsar and the star are located at $(r, z) = (0, 5\ a)$ and $(r, z) = (0, 60\ a)$, respectively.

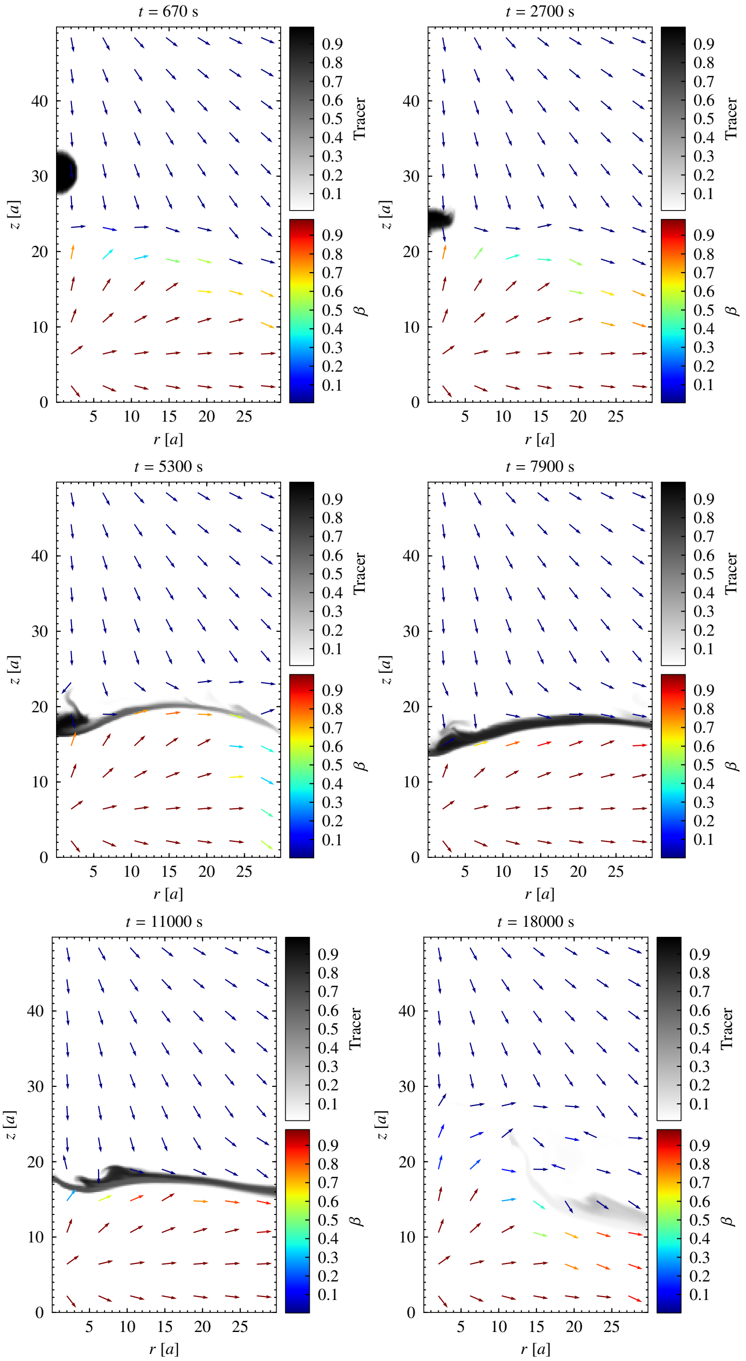

Figure 6.8: Tracer distribution by color for the case with clump parameters $\chi = 10$ and $R_c = 2.5\ a$ for the times shown at the top of each plot. The tracer value ranges from 0 (pulsar and stellar wind) to 1 (clump). The remaining plot properties are the same as those of Fig. 6.2.

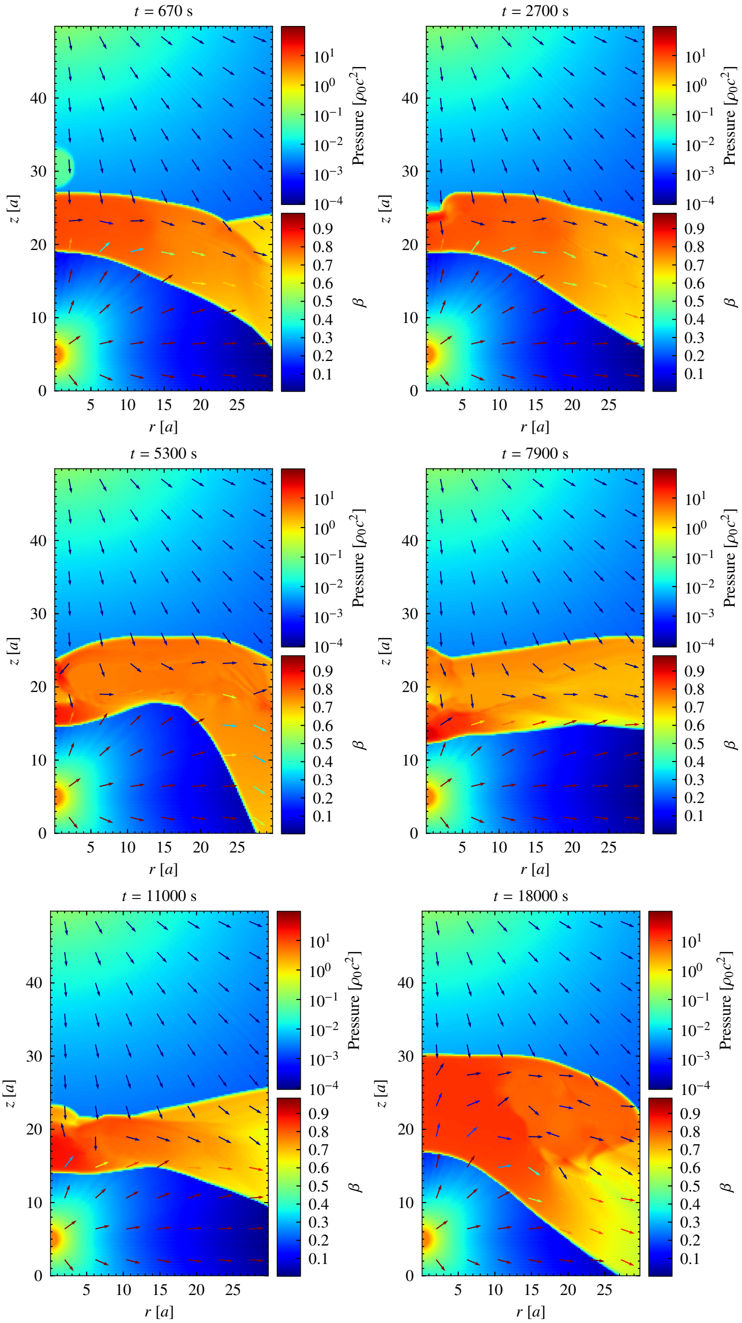

Figure 6.9: Pressure distribution in units of $\rho_0 c^2$ by color for the case with clump parameters $\chi = 10$ and $R_c = 2.5\ a$ for the times shown at the top of each plot. The remaining plot properties are the same as those of Fig. 6.2.

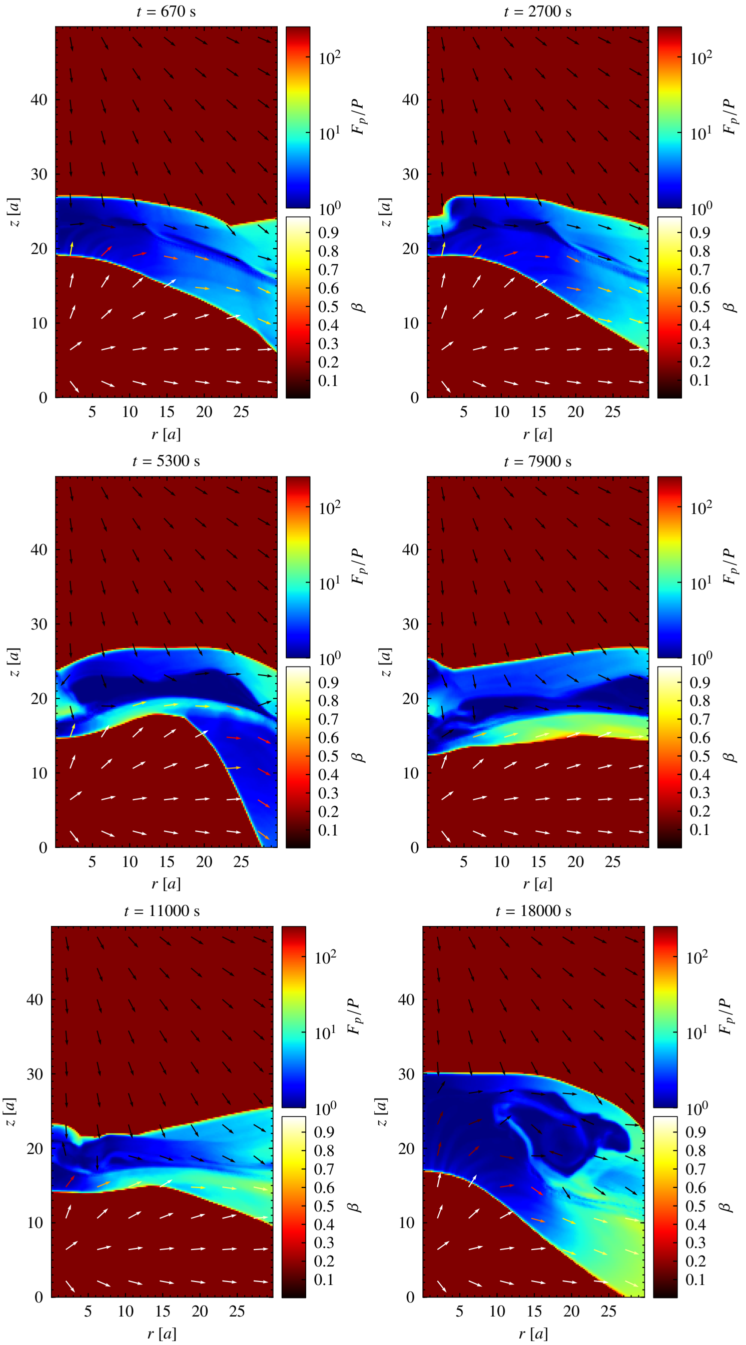

Figure 6.10: Momentum flux over pressure distribution by color for the case with clump parameters $\chi = 10$ and $R_c = 2.5\ a$ for the times shown at the top of each plot. The momentum flux is given by $F_p = \rho\,\Gamma^2 v^2 (1 + \epsilon + P/\rho) + P$. The remaining plot properties are the same as those of Fig. 6.2.

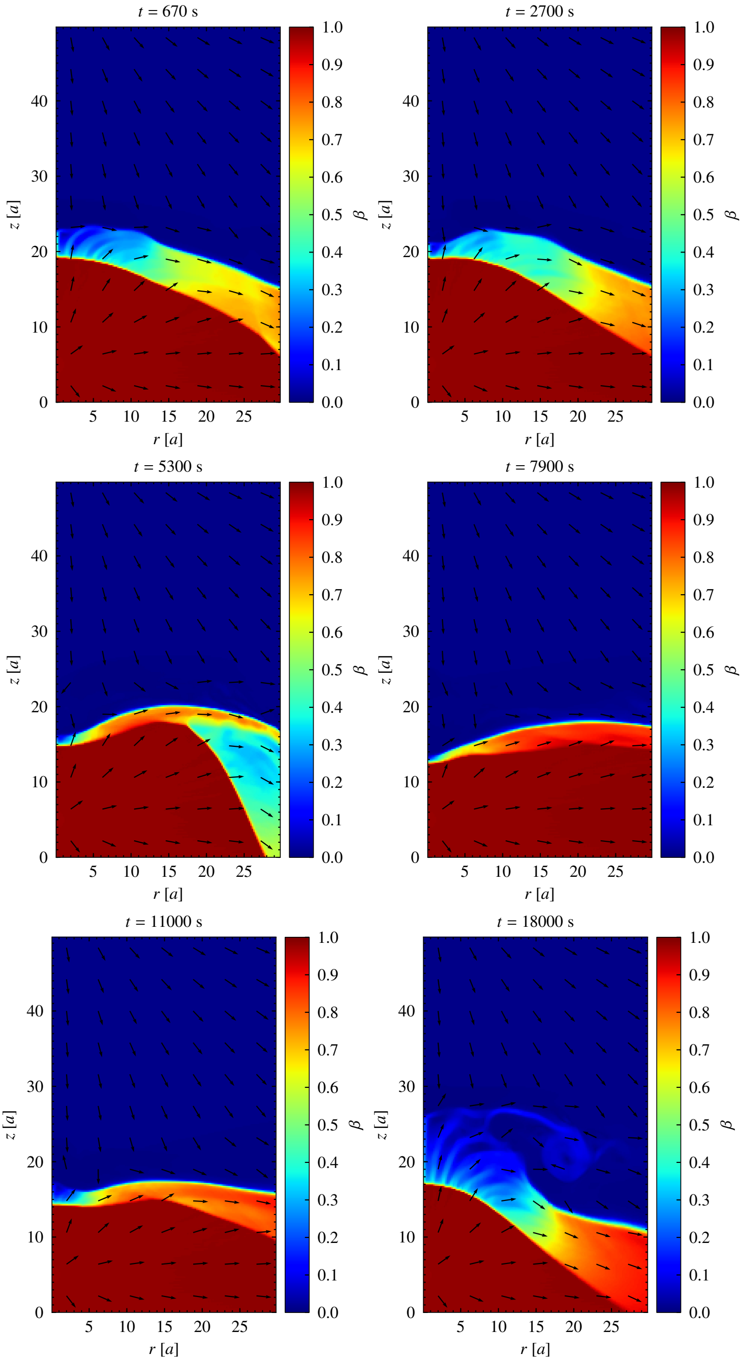

Figure 6.11: β distribution by color for the case with clump parameters $\chi = 10$ and $R_c = 2.5\ a$ for the times shown at the top of each plot. The remaining plot properties are the same as those of Fig. 6.2.

Concerning stability, under the perturbation induced by the clump with $\chi = 10$ and $R_c = 5\ a$, the system recovers the steady state after the clump has been advected. In contrast, for the cases with $\chi = 10$ and $R_c = 2.5\ a$, and $\chi = 30$ and $R_c = 1\ a$, the instabilities eventually lead to the collapse of the two-wind interaction region, filling the region close to the pulsar with shocked pulsar wind. The clump with $R_c = 1\ a$ and $\chi = 10$ only slightly perturbs the two-wind interaction region and pushes the contact discontinuity to $\sim 2/3$ of its initial distance (see Fig. 6.2) to the pulsar (see Fig. 6.3). Afterwards, the system recovers the (quasi-)steady state. We recall that although the steady-state solution is only metastable in the context of our simulations, the main features of the clump phase should be reliable because the clump represents a dominant perturbation over any other, physical or numerical, before it is assimilated by the two-wind flow.

Other simulations, not shown here, were carried out for clumps with $R_c = 0.5$–5 and $\chi =10$–100. As seen before, the impact on the two-wind interacting region is larger the denser the clump or the larger is its radius, so different combinations of these parameters yield results in line with those shown.

To show the impact of increasing resolution, we present the results of two simulations with the same set-up but, a resolution 2 and 1.5 times (i.e. 300×500 and 225×375 cells, respectively) higher than the resolution adopted for most of the simulations in this work. For the highest resolution case, we were unable to reach steady state (without clump) because the higher resolution allowed the rapid development of instabilities already within the grid, leading to the collapse of the two-wind interaction region. A temporal state of this simulation taken shortly before the collapse of the interaction region is shown in Fig. 6.12. For the intermediate-resolution case, we reached (quasi-)steady state, but compared with the lower resolution simulations, it presented a more unstable pattern in the two-wind interaction region away from the simulation axis and a more compressed two-wind interaction region close to the axis singularity. A sequence of images showing the evolution of a clump characterized by $\chi = 10$ and $R_c = 2.5\ a$ for the intermediate resolution simulation is shown in Fig. 6.13. The higher resolution allowed the de-

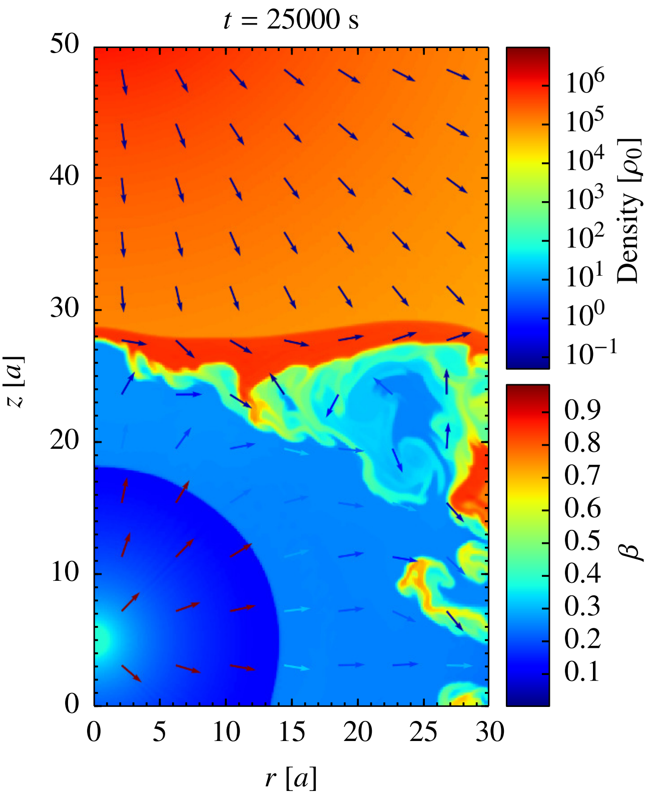

Figure 6.12: Density distribution by color at time $t = 25000$ s for the simulation with a resolution of 300×500 cells. The remaining plot properties are the same as those of Fig. 6.2.

velopment of denser small-scale structures that pushed the pulsar wind termination shock closer to the neutron star. However, the general behavior of the higher and lower resolution clump simulations is similar, which suggests that the main features resulting from the lowest resolution simulations, albeit smoother, are reliable.

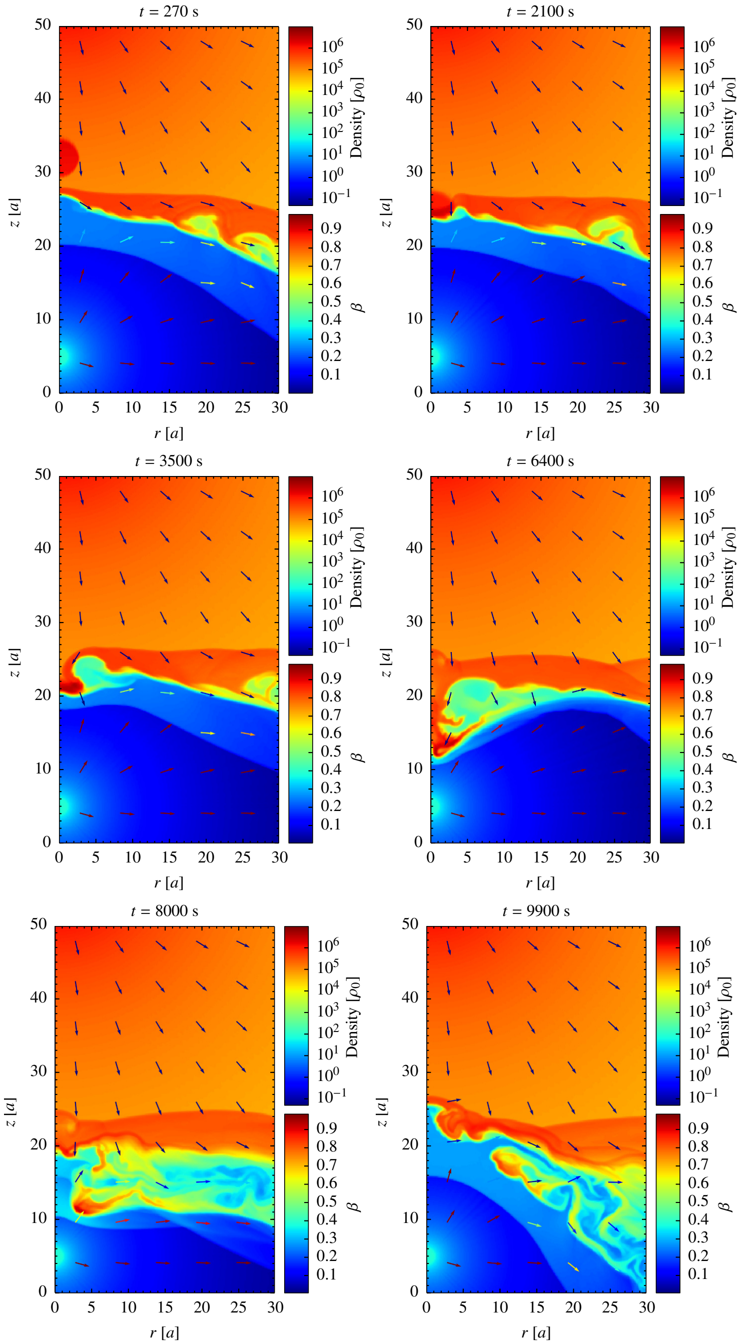

Figure 6.13: Density distribution by color for the case with clump parameters $\chi = 10$ and $R_c = 2.5\ a$ and a resolution of 225×375 cells for the times shown at the top of each plot. The remaining plot properties are the same as those of Fig. 6.2.

6.4 DISCUSSION

The interaction of a relativistic pulsar wind with the non-relativistic wind of a massive star was simulated through relativistic axisymmetric hydrodynamic calculations. The two-wind interaction structure reaches a (quasi-)steady state, although the solution is metastable and quite sensitive to the initial set-up parameters, such as the grid size or the wind density contrast. Therefore, even though the collision between the two winds forms a structure similar to those previously found in axisymmetric relativistic simulations, it shows some irregularities (Fig. 6.2). In the dynamical problem solved here, the axisymmetric geometry may introduce numerical perturbations to the physical solution that grow affected by the RT instability close to the axis, and by the KH instability farther away. However, similar irregularities have been also found in relativistic 2D simulations in planar geometry that have been attributed to the development of KH instabilities (Bosch-Ramon et al. 2012; Lamberts et al. 2013), which implies that the irregularities found in this work are not only related to the axisymmetric geometry adopted (see also Bosch-Ramon et al. 2015).

The growth of instabilities strongly affects the shocked pulsar-wind region in its (quasi-)steady state. Given the very high sound speed, this region can change within time intervals significantly shorter than the dynamical time of the simulation, $\sim d/v_{\rm sw}$, dominated by the slow stellar wind. Nevertheless, we find that over all the interaction region follows the expected geometry both for the contact discontinuity and for the width of the two-wind collision region (Bogovalov et al. 2008, 2012).

The arrival of clumps can have a very strong impact on the whole interaction structure, overcoming the effect of any possible numerical perturbation related to the geometry of the calculations. The clumps trigger violent RT and KH instabilities because the structure is prone to suffer them, and thus the interaction between the clump and the two-wind collision region is highly non-linear, leading not only to a *secular* modification of the general geometry, but also to quick changes of the shocked pulsar-wind region. This is apparent in all the map time sequences (in

Table 6.3: Clump impact on the size of the two-wind interaction region. Density contrast χ, clump radius R_c, numerical minimum distance with respect to the contact discontinuity $R'_{\rm num}$ (analytical: $R'_{\rm an}$), and numerical minimum distance with respect to the termination shock $R'^{\rm (TS)}_{\rm num}$.

χ	R_c (a)	$R'_{\rm num}$ (a)	$R'_{\rm an}$ (a)	$R'^{\rm (TS)}_{\rm num}$ (a)
10	1	13	14.8	11
10	2.5	8.5	10	7.5
10	5	7.5	2.2	6
30	1	10	12.5	8

particular in the zoomed-in sequence: Fig. 6.7), as the largest variations affect the shocked pulsar wind.

Below we discuss a few relevant points: the comparison between the analytical and the numerical approximation; the clump effect on the overall structure and radiation, with a mention of the GeV flare of PSR B1259—63 as a possible instance of matter clump-perturbation of the two-wind interaction region, and work under development.

6.4.1 *Numerical results vs analytical estimates*

An analytical estimate of the minimum distance between the two-wind interaction region and the pulsar, after the clump has penetrated the shocked pulsar wind, has been presented in Sect. 6.2. For comparison, the analytical and numerical values of the minimum distances from the contact discontinuity and the termination shock to the pulsar, are shown in Table 6.3 for all the simulated clumps.

The final distance between the pulsar and the contact discontinuity, for a given density contrast and a clump radius, computed using Eq. (6.1), agree well with the numerical results except for the clump with radius $R_c = 5\ a$ (see Table 6.3). The reason is that such a large clump is already outside of the application range of Eq. (6.1), which strictly applies only to clumps with $R_c \ll R'$. For $R_c \to R'$ or bigger, the clump behaves more as an homogeneous wind than as a discrete obstacle, but χ times denser than the average stellar wind. In this case, the minimum distance from the contact discontinuity to the pulsar can be computed from Eq. (6.3), and assuming momentum flux equality, as $R' = \eta_{\chi}^{1/2}\, d/(1+\eta_{\chi}^{1/2}) \simeq \eta_{\chi}^{1/2}\, d$, with $\eta_{\chi} = \chi^{-1}\eta$. For $\chi = 10$ it gives $R'_{\rm an} \sim 7.9\ a$, which agrees well with the numerical result for the clump with $R_c = 5\ a$ ($R'_{\rm num} \approx 7.5\ a$).

The time required for the clump with $\chi = 10$ and $R_c = 2.5\ a$ to become shocked is ~ 4000 s, and for full clump disruption, meaning that when the clump material is advected away already integrated in the shocked flows, the time required is $\sim$ 10000–15000 s (see Fig. 6.7). These times are consistent with the analytical value of the clump lifetime, $\sim \chi^{1/2} R_c/v_{\rm sw} \approx 2000$ s (Bosch-Ramon 2013), or 4000 s, if the clump diameter is adopted as the characteristic clump size.

6.4.2 *Clump effects on the global structure and radiation*

On the scales simulated in this work, stellar winds with a modest inhomogeneity degree ($\chi = 10$ and $R_c = 1\ a$) present non-negligible variations of the interaction structure, and even smaller/lighter clumps can provide continuous perturbations for the development of instabilities in the contact discontinuity. In addition, larger size or denser clumps ($R_c = 2.5$, $5\ a$ and $\chi = 10$; $R_c = 1\ a$ and $\chi = 30$) can lead to strong variations in the size of the two-wind interaction structure. Both small and larger/denser clumps can generate quick and general variations in the shocked pulsar wind. This affects the location of the pulsar wind termination shock (i) and also introduces seeds for small-scale relativistic and transonic turbulence that would grow downstream of this shock (ii).

(i) The consequences of large variations in the termination shock location have previously been discussed in Bosch-Ramon (2013). In short, they can induce variations in the cooling, radiative as well as non-radiative, channels, and non-linear radiation processes, through synchrotron self-Compton or internal pair creation, for large reductions of the emitter size.

(ii) The relativistic flow variations on small spatial and temporal scales downstream of the pulsar wind shock, already apparent despite the modest resolution in Fig. 6.11, would lead to a complex radiative pattern in time and direction. This complex radiative pattern is caused by Doppler boosting because of the complex orientation of the fluid lines and the relativistic speeds achieved through re-acceleration of the shocked pulsar wind (see Khangulyan et al. 2014, for a study of the impact of Doppler boosting on radiation).

Finally, weak shocks are present in the shocked pulsar wind (e.g., Fig. 6.10), which suggests that further particle acceleration, additional to that occurring in the pulsar wind termination shock, could take place already deep inside the binary system, well before the postshock flow has been affected by the orbital motion (see, e.g., Bosch-Ramon et al. 2012, 2015, for a discussion of the larger-scale evolution of the shocked structure).

6.4.2.1 *The flare in PSR B1259–63*

The flare in PSR B1259–63, observed by Fermi about 30 days after periastron passage (Abdo et al. 2011), has a potential connection with the Be disc through the disruption and fragmentation of the latter. This may have led to the impact of a dense piece of disc on the two-wind interaction structure, largely reducing the size of the pulsar wind termination shock. This size reduction could allow efficient Compton scattering by a population of GeV electrons on local X-ray photons, as proposed in Dubus & Cerutti (2013) (see also Khangulyan et al. 2012, for a similar proposal involving infrared photons) as a result of the strong enhancement of the X-ray photon density. This idea is worth to be studied in more detail, although it remains unclear why such a modification of the GeV emitter has no clear effects at other wavelengths (Chernyakova et al. 2014).

It is worth estimating what fraction of the mass of a Be stellar disc the simulated clumps would represent. The mass of a typical Be disc can be derived from the disc mass-loss rate, $\sim 10^{-12}$–$10^{-9}\,M_\odot\,\mathrm{yr}^{-1}$, times the disc extension, say ~ 1 AU (quantities similar to those adopted in

Okazaki et al. 2011 and Takata et al. 2012), with a typical disc radial velocity of ~ 1 km s^{-1} (Okazaki 2001). This yields a disc mass of $\sim 10^{22}$–10^{25} g. In particular, for PSR B1259–63, Chernyakova et al. (2014) estimated a disc mass of 2×10^{25} g, with a disc radius of 0.42 AU, roughly similar to the values just mentioned. The masses of the simulated clumps are $\sim 8 \times 10^{18}$ g, $\sim 10^{20}$ g, $\sim 10^{21}$ g and $\sim 2 \times 10^{19}$ g for the clumps characterized by $\chi = 10$ and $R_c = 1\ a$, $2.5\ a$, $5\ a$ and $\chi = 30$ and $R_c = 1\ a$, respectively. For comparison, the mass of the clump with $R_c = 2.5\,a$ would be ~ 0.001–1% the disc mass.

6.4.3 *Future work*

To distinguish the importance of numerical artefacts in our results and study a more realistic case, a 3D version of the simulations presented here is under way to more accurately characterize the instabilities that affect the two-wind interaction region. In addition, we are planning to carry out calculations of the radiation outcome expected from the two-wind interaction region, and most importantly, from the clump interaction with this structure, making full use of the dynamical information provided by these simulations (de la Cita et al., in preparation).

6.5 CONCLUSIONS

We presented, for the first time, 2D axisymmetric RHD simulations of the interaction between an inhomogeneous stellar wind and a relativistic pulsar wind, focusing on the region inside the binary system. We simulated clumps with different sizes and densities to study different degrees of the stellar wind inhomogeneity. The presence of the clumps results in significant variations of the interaction region, which are expected to strongly affect the non-thermal radiation as well. Therefore, we confirm the sensitive nature of the two-wind interaction structure to the presence of the stellar wind inhomogeneities. The shocked flow presents a complex spatial and temporal pattern, with fast changes in the shocked pulsar wind. This can lead to strong short time-scale flux variability in the non-thermal radiation of gamma-ray binaries, which might be observed for instance in gamma rays with the future Cherenkov Telescope Array (CTA; Acharya et al. 2013; Paredes et al. 2013).

7

HYDRODYNAMICAL STREAMLINE COMPUTATION

The raw data produced by RHD simulations only provide information on the dynamics of the simulated system, and the derived radiative information is often limited to an inference out of the qualitative or semi-quantitative analysis of that data. In order to obtain detailed information of the radiative output of the simulated system, we need to feed a radiative code with the proper hydrodynamical information, i.e., the *streamlines* of the RHD simulation, which are the trajectories followed by the fluid elements in a steady flow. The main objective of this chapter is to provide an introduction to streamline calculations, and present the results obtained in the context of this thesis.

In Section 7.1 we describe all the process and assumptions made to compute a streamline from an axisymmetric RHD simulation. The streamline calculation from RHD simulations has been implemented with a Python code developed in the context of this thesis[1]. In Section 7.2 we present the streamlines computed from the RHD simulations presented in Chapter 6 (see Appendix B for RHD simulations and streamline calculations of an AGN jet interacting with a stellar wind). The posterior radiative computations are conducted by our collaborators and are beyond the scope of this thesis. See our contribution in de la Cita et al. 2016 for the radiative calculation in the context of AGN.

---

[1] The Python code developed to compute the streamlines from RHD simulations is available at `https://github.com/xparedesfortuny/pylines`

7.1 STREAMLINE CALCULATION

A streamline defines the trajectory followed by a fluid element in a steady flow. Because RHD simulations provide with the physical values at each cell of the simulated grid, assuming steady flow conditions, a streamline can be computed tracing a fluid element with the spatial components of the velocity at each cell.

In axisymmetric RHD simulations, with cylindrical coordinates r and z, the time evolution can be computed as:

$$\begin{aligned} r_{\text{new}} &= r + v_r \Delta t, \\ z_{\text{new}} &= z + v_z \Delta t, \end{aligned} \tag{7.1}$$

being v_r, v_z, and Δt the velocities and the time step size, respectively. The time step is set by the minimum cell size over the maximum speed in the simulation. After a new position is obtained, bilinear interpolation is applied to obtain the physical variables, v_r, v_z, ρ, and p, at the new position (Press et al. 1992). The process is repeated until the fluid element falls outside the simulated grid.

The radiative calculations not only require the values of the hydrodynamical physical variables along the line, but also the streamline values for the transversal area and the magnetic field. The transversal surface is computed assuming conservation of the energy crossing the streamline transversal sections per time unit as

$$S = S_0 \frac{\rho_0 \Gamma_0^2 h_0 v_0}{\rho \Gamma^2 h v}, \tag{7.2}$$

denoting the subscript 0 the value in the first cell of the streamline, and being h the enthalpy, v the modulus of the three-velocity, and Γ the Lorentz factor. Due to the axisymmetric nature of the simulation, the initial transversal surface of a fluid element is

$$S_0 = \pi \left(r_{\text{outer}}^2 - r_{\text{inner}}^2 \right), \tag{7.3}$$

being r_{outer} and r_{inner} the right and left radial boundaries of the initial fluid element defining the streamline.

The magnetic field in the fluid reference frame along the streamline is computed assuming that it is frozen into the plasma and is perpendicular to its direction of motion:

$$B = B_0 \sqrt{\frac{\rho v_0 \Gamma_0}{\rho_0 v \Gamma}}, \tag{7.4}$$

being B_0 the magnetic field at the first cell, derived assuming equality between the Poynting flux and a fraction χ_B of the matter flux as

$$B_0^2 = \chi_B 4\pi(\rho_0 h_0 c^2). \tag{7.5}$$

7.2 STREAMLINES OF THE INTERACTION OF RELATIVISTIC PULSAR WINDS WITH INHOMOGENEOUS STELLAR WINDS

We present the streamline calculation of the RHD simulations of the interaction of relativistic pulsar winds with inhomogeneous stellar winds presented in Chapter 6. The posterior radiative computations of the non-thermal radiation are conducted by our collaborators and are beyond the scope of this thesis.

Because we are interested in the non-thermal particles we computed the streamlines originating at the injection of the pulsar wind, i.e., those current lines starting at a distance of 2.4×10^{11} cm with respect to the pulsar center located at $(r_0, z_0) = (0, 4 \times 10^{11})$ cm. The steady flow assumption needed to compute the streamlines (Section 7.1) is guaranteed by the larger dynamical time-scales of the two-wind interaction region compared with the time-scales of the shocked pulsar wind.

As an illustration of calculations of streamlines, Figs. 7.1 and 7.2 show the computed current lines plotted on top of the density map for the simulation of the interaction between an homogeneous stellar wind and a pulsar wind in the (quasi)-steady state, and for the clump with $\chi = 10$ and $R_c = 8 \times 10^{10}$ cm, respectively.

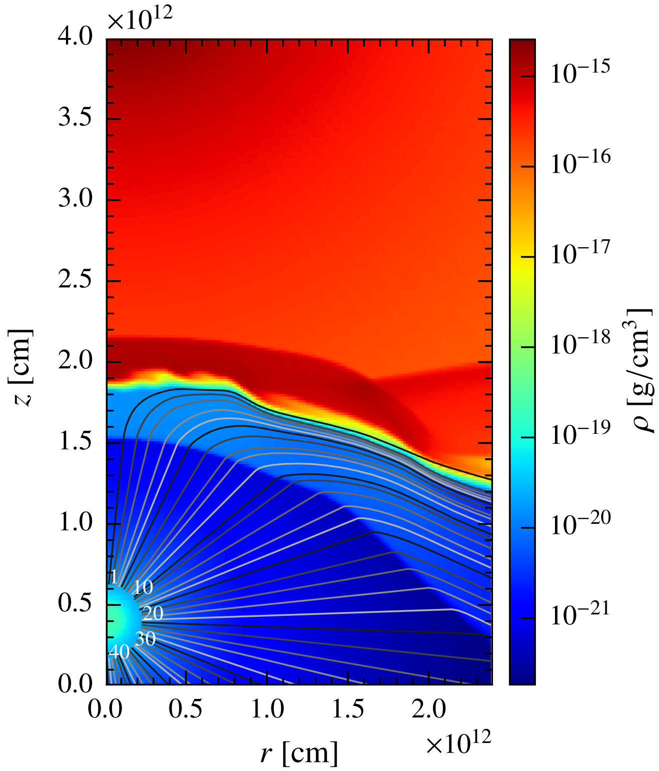

Figure 7.1: Density distribution by color at time $t = 5.8 \times 10^4$ s in the (quasi)-steady state. The star is located at $(r_0, z_0) = (0, 4.8 \times 10^{12})$ cm and the pulsar wind is injected at a distance of 2.4×10^{11} cm with respect the pulsar center at $(r_0, z_0) = (0, 4 \times 10^{11})$ cm. The grey lines show the obtained streamlines describing the trajectories of the pulsar wind fluid cells.

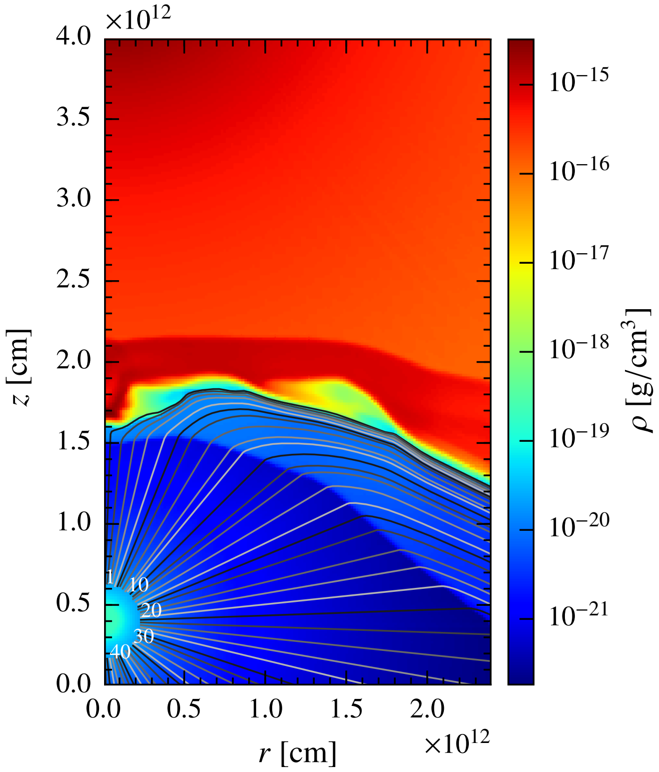

Figure 7.2: Density distribution by color at time $t = 0.4 \times 10^4$ s (measured from the steady case) considering an inhomogeneous stellar wind with $\chi = 10$ and $R_c = 8 \times 10^{10}$ cm. The remaining plot properties are the same as those of Fig. 7.1.

Part III

CONCLUDING REMARKS

8

CONCLUDING REMARKS OF THE THESIS

In this PhD thesis we presented observational and theoretical studies of the interaction of pulsar winds with stellar environments in gamma-ray binaries. In this chapter, we list the most relevant new scientific results obtained from the work conducted in the context of this thesis, both for the observational (Section 8.1) and theoretical studies (Section 8.2).

8.1 CONCLUDING REMARKS OF PART I

In Part I we presented the results of the long-term optical photometric and $EW_{\mathrm{H}\alpha}$ monitoring of the gamma-ray binary LS I +61 303 (four yearly observational campaigns). The new scientific results obtained from that part are:

- The optical observations of both photometric and $EW_{\mathrm{H}\alpha}$ present a superorbital variability of the orbital phase of the maximum, as seen in radio and X-rays, providing an evidence of the coupling between the thermal and non-thermal emission processes in LS I +61 303.
- The optical photometric observations present a superorbital variability of the flux compatible with the 1667 d superorbital period. We confirm previous results on the same effect with the $EW_{\mathrm{H}\alpha}$ observations.
- This superorbital variability is attenuated close to periastron in both the optical photometry and $EW_{\mathrm{H}\alpha}$.

- In the optical photometry, the superorbital variability is not present in the orbital phase bin 0.83–0.93, and re-appears in the next orbital phase bin 0.93–0.03.
- Optical orbital variability in a multi-wavelength context is as follows:
  - The optical photometry always presents a positive lag with respect contemporaneous $EW_{\mathrm{H}\alpha}$ measurements (~ 0.1, ~ 0.1, ~ 0.4, and ~ 0.5 orbital phases, for each of the four observational campaigns, respectively).
  - The $EW_{\mathrm{H}\alpha}$ maximum of emission, of the first and second observational campaigns, occurs at similar orbital phases than non-contemporaneous radio outbursts, whereas it is delayed by ~ 0.2 and ~ 0.5 orbital phases for the last two observational campaigns, respectively.
  - The photometric maximum lags ~ 0.3 orbital phases with respect X-ray outbursts from the previous superorbital cycle.
  - These lags can be naturally interpreted considering different emitting regions.
- Constrains in the optically emitting circumstellar disk. The observations seem to be:
  - Only compatible with an optically emitting extended disk with a radius larger than the periastron distance.
  - Only compatible with a coplanar (or slightly inclined) circumstellar disk.
  - Compatible with a strong perturbation of the disk due to the periastron passage of the compact object, resulting in a decrease of the overall optical emission at those phases (and its superorbital variability).
- Constrains in the superorbital variability scenario. The observations seem to be:

  - Compatible with a scenario where the circumstellar disk properties are periodically modulated.
  - Compatible with the density wave scenario.
  - Not compatible with a expanding/shrinking disk model.
  - Not compatible with a precession-disk model that produces the superorbital variability only by a change in the projected emitting area through precession.
  - Compatible with a very restrictive precession-disk, involving low precession angles, that interacts with the compact object.

8.2 CONCLUDING REMARKS OF PART II

In Part II we presented the results of the simulations of the interaction of relativistic pulsar winds with inhomogeneous stellar winds (hereafter clumps). The new scientific results obtained from that part are:

- General remarks. Results obtained for the first time from numerical simulations:
  - In the context of axisymmetric simulations, the two-wind interaction structure is very unstable and sensitive to the tiniest perturbations, which lead to quick Rayleigh-Taylor (RT) and in particular Kelvin-Helmholtz (KH) instability growth.
  - The arrival of clumps can have a very strong impact on the whole interaction structure, which is expected to strongly affect the non-thermal radiation as well.
  - The clumps trigger violent RT/KH instabilities leading to quick changes of the shocked pulsar-wind region.
- Clump effects on the global structure:
  - Clumps characterizing a modest inhomogeneity degree: produce non-negligible variations of the interaction structure and enhancement of the instability growth.

  - Clumps characterizing a high inhomogeneity degree: produce strong variations in the size of the two-wind interaction structure.
  - Clumps generate quick and global variations in the shocked pulsar wind. This can lead to strong short time-scale flux variability in the non-thermal radiation of gamma-ray binaries.

- Scientific hypothesis supported by our simulations:
  - The impact of a piece of disk on the two-wind interaction structure in the gamma-ray binary PSR B1259–63 could cause the flare observed by Fermi $\sim$ 30 days after periastron passage.
  - The impact of clumps might explain the short X-ray variability from scales of second to hours found in the X-ray light curves of LS 5039 and LS I +61 303.

Part IV

APPENDIX

A

OTHER OBSERVATIONAL RESULTS

The observational results presented in this thesis have been focused in the optical observations of the gamma-ray binary LS I +61 303. However, we initiated many observational campaigns apart from those of LS I +61 303. The main objective of this chapter is to provide a short overview of some of the other observational results obtained in the context of this thesis for sources showing/possibly showing gamma-ray emission.

In this chapter, we present the optical photometric observations of the following sources: MWC 656 (Section A.1), MWC 148 (Section A.2), TYC 4051-1277-1 and TYC 3594-2269-1 (Section A.3), and PSR J1023+0038 (Section A.4). The presented optical photometric observations have been conducted with the robotic 0.5 m telescope TFRM (see Fors et al. 2013 and Section 2.1). The data reduction and analysis have been conducted using the pipeline presented in Section 3.

A.1 MWC 656

MWC 656 (HD 215227) is a Be star (V ∼ 8.8 mag) that has been proposed by Williams et al. (2010) as the optical counterpart of the transient HE gamma-ray source AGL J2241+4454 detected by *AGILE* (Lucarelli et al. 2010). Williams et al. (2010) discovered an optical photometric periodicity of 60.37 d, and based on this suggested a binary nature for the source. This was later confirmed thanks to radial velocity measurements by Casares et al. (2012). Casares et al. (2014) revealed a black hole as the nature of the compact object, discovering the first binary system hosting a Be-type star with a black hole companion.

In Fig. A.1 we present preliminary results on the ongoing optical photometric program on MWC 656. The optical photometric observations span from 2012 July 23 to 2016 January 01 with 181 nights of good data. The orbital variability originally discovered by Williams et al. (2010) is clearly seen. Very preliminary results were published in Paredes-Fortuny et al. (2012).

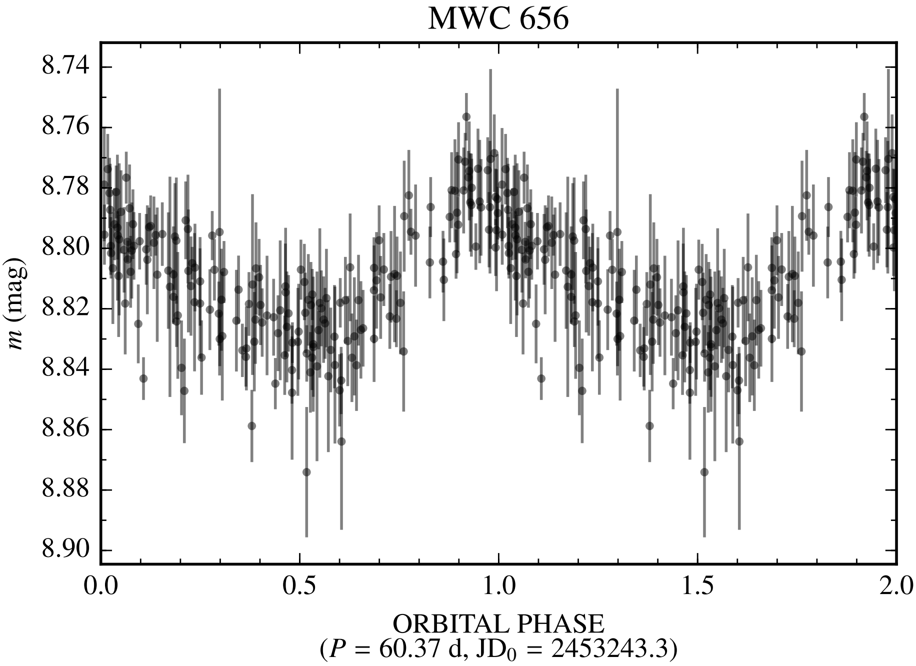

Figure A.1: Optical photometric light curve of MWC656 folded with the orbital period. Error bars represent 1σ uncertainties. Two cycles are displayed for clarity.

A.2 MWC 148

MWC 148 is a Be star (V ~ 9.1 mag) that has been proposed by Aharonian et al. (2007) as the optical counterpart of the VHE source HESS J0632+057. Bongiorno et al. (2011) reported X-ray flares modulated with a period of 321 d, suggesting the binary nature for the source. Casares et al. (2012) found a 321 d modulation in the main parameters of the Hα emission line. Casares et al. (2012) also presented radial velocity curves and an orbital solution for the system, confirming its binary nature.

In Fig. A.2 we present preliminary results on the ongoing optical photometric program on MWC 148. The photometric observations span from 2013 January 30 to 2016 January 27 with 68 nights of good data.

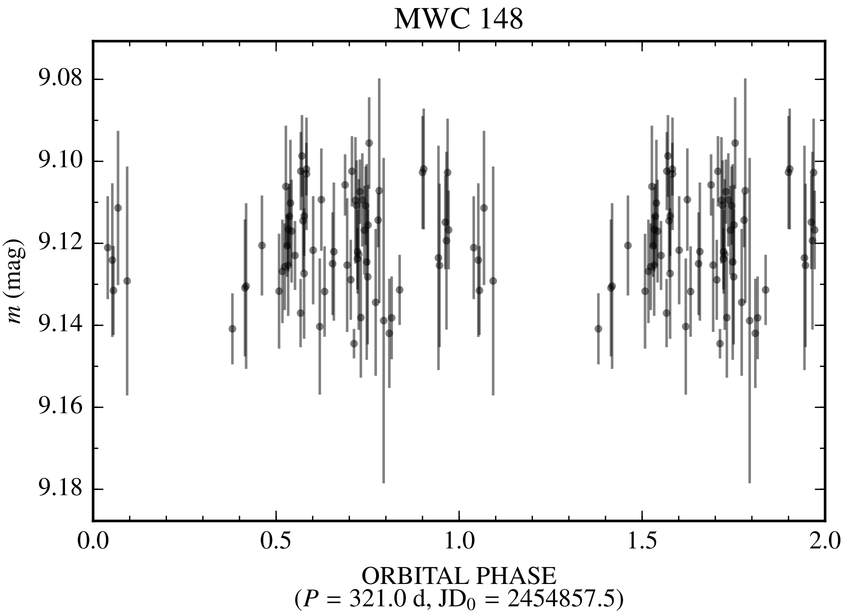

Figure A.2: Optical photometric light curve of MWC 148 folded with the orbital period. Error bars represent 1σ uncertainties. Two cycles are displayed for clarity.

A.3 TYC 4051-1277-1 AND TYC 3594-2269-1

In the quest of non-thermal signatures in early-type stars, Martí et al. (2015) conducted optical and radio observations of the early type stars TYC 4051-1277-1 and TYC 3594-2269-1, being the former located in the error ellipse of a *Fermi* source. However, these sources were not detected at radio wavelengths.

In Figs. A.3 and A.4 we present the optical photometric results published in Martí et al. (2015). The TYC4051-1277-1 observations span from 2012 July 31 to 2014 February 5 with 81 nights of good data. The TYC3594-2269-1 observations span from 2012 October 3 to 2013 June 12 with 54 nights of good data. The data reduction was conducted with a previous version of the pipeline presented in Section 2.1. The main difference is that the aperture photometry was performed using the `PHOT` package from `IRAF` instead of `SExtractor`.

For the TYC 4051-1277-1 observations, a χ^2 test assuming a constant value provided a reduced χ^2 of 1.28, which implies variability at 2.0σ c.l.. We searched for periodicities between 2 and 200 d using the Phase Dispersion Minimization (PDM) (Stellingwerf 1978) and the CLEAN (Roberts et al. 1987) algorithms. A possible period of 6.08 d appears in the data, although the fact that statistically we cannot claim variability makes us to be very cautious in this respect. More data are needed to assess the variability/periodicity in the optical light curve of this source.

For the TYC3594-2269-1 observations, a χ^2 test assuming a constant value provided a reduced a χ^2 of 2.31, which implies detection of variability at 5.2σ c.l.. We have also run the PDM and CLEAN algorithms to the TYC 3594-2269-1 data set. There are some possible periods between 20 and 30 days, but none of them is significant enough to claim periodicity. As in the previous case, more data are needed to clarify this issue.

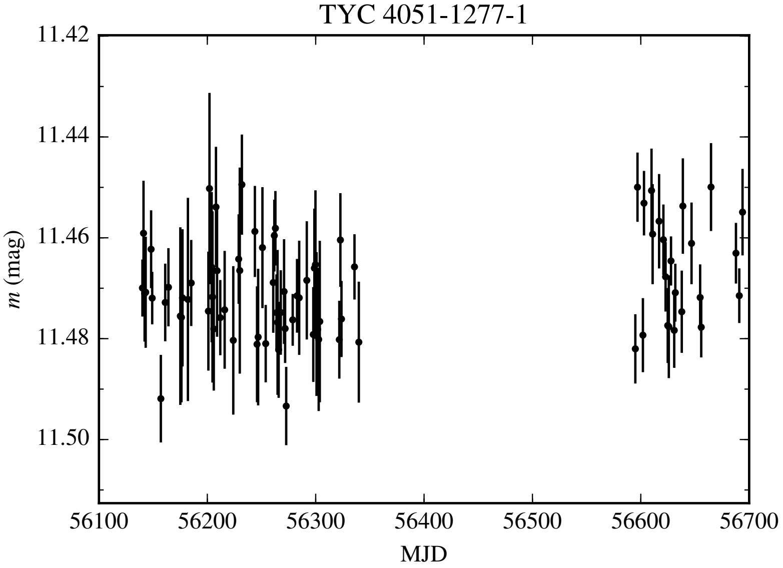

Figure A.3: Optical photometric light curve of TYC 4051-1277-1 as a function of the MJD. Error bars represent 1σ uncertainties.

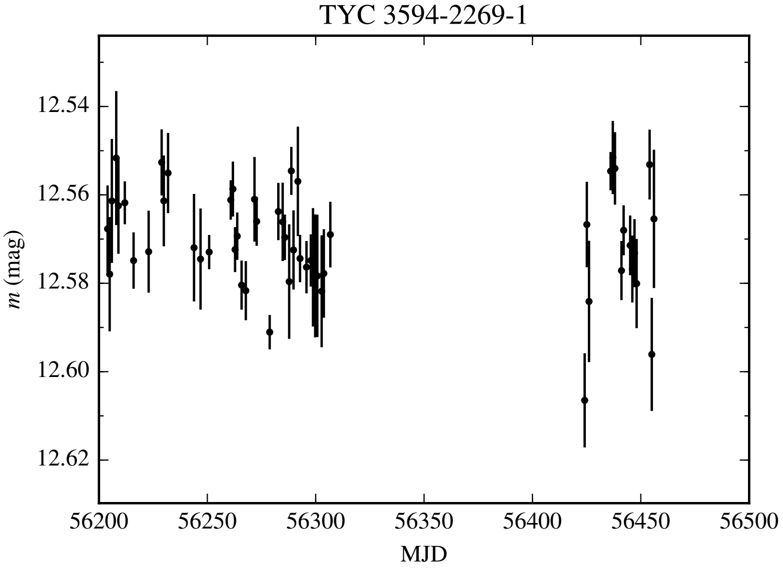

Figure A.4: Optical photometric light curve of TYC 3594-2269-1 as a function of the MJD. Error bars represent 1σ uncertainties.

A.4 PSR J1023+0038

PSR J1023+0038 is a galactic radio millisecond pulsar in a 4.75 hr circular binary orbit with an optical star. This binary system ($V \sim 17$ mag) has displayed two very different states: a non-accreting state where radio pulsations have been detected, and an accreting state where pulsations have not been found (current state). Gamma-ray emission during the accreting state has been detected with *Fermi*. See Archibald et al. 2009; Halpern et al. 2013; Stappers et al. 2014 and references therein.

In Fig. A.5 we present the optical photometric observations of the binary system hosting PSR J1023+0038. The optical photometric observations span from 2014 November 21 to 2015 November 19 with 34 nights of good data, resulting in 428 individual measurements. Because the source presents hourly variability, nightly averages have not been conducted. The error bars are omitted for the sake of clarity, but are typically ± 0.06 mag (estimated from the average of the standard deviation of the nightly measurement of a comparison star with a similar magnitude). The observed behavior is similar to that shown in Bogdanov et al. (2015).

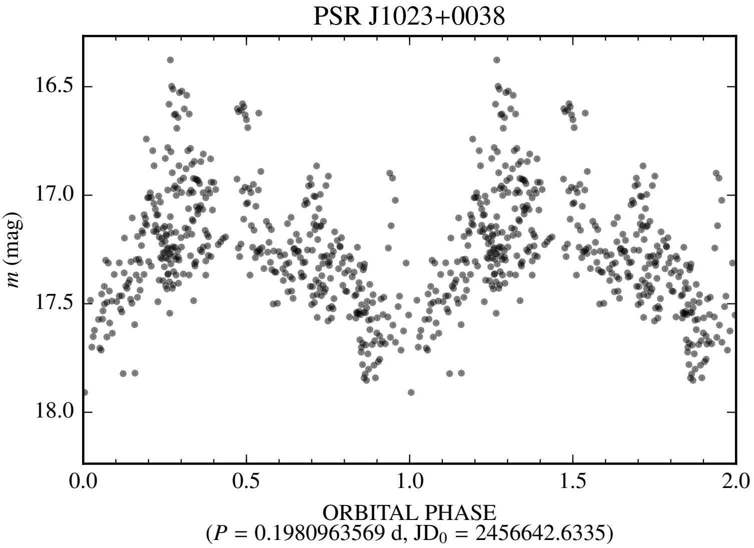

Figure A.5: Optical photometric light curve of PSR J1023+0038 folded with the orbital period. Error bars represent 1σ uncertainties. Two cycles are displayed for clarity.

B

SIMULATIONS OF A RELATIVISTIC JET

This thesis is centered on the study of the interaction of pulsar winds with stellar environments in gamma-ray binaries. However, during the context of this thesis we conducted complementary studies on other possible, related, physical scenarios of gamma-ray emission. In this Chapter we present axisymmetric RHD simulations and streamline calculations of the interaction of a relativistic jet with two different environments.

In Section B.1 we present the simulations and streamline calculations of a relativistic jet interacting with a stellar wind. These streamlines have been used to compute detailed radiative calculations by our collaborators and have been published in de la Cita et al. (2016). In Section B.2 we show the simulations and streamlines of the same jet, but now interacting with a very dense obstacle.

B.1 SIMULATIONS OF A JET-STELLAR WIND INTERACTION

B.1.1 *Numerical set-up*

We performed axisymmetric RHD simulations of the interaction of a relativistic jet and a stellar wind, using the same numerical code (Martí et al. 1997; Perucho 2005) as in those simulations presented in Chapter 6. We assumed an ideal relativistic gas without magnetic field, one particle species, and a relativistic polytropic index of $\gamma^{\text{ad}} = 4/3$. The physical size of the domain is $r \in [0, l_r]$, with $l_r = 2 \times 10^{15}$ cm, and $z \in [0, l_z]$, with $l_z = 1.5 \times 10^{15}$ cm. The adopted resolution is 400×300 cells (see

Table B.1: Simulation parameters. Polytropic index γ^{ad}, physical r grid size l_r, physical z grid size l_z, number of cells in the r axis n_r, and number of cells in the z axis n_z.

Parameter	Jet-stellar wind simulation
γ^{ad}	$4/3$
l_r	2.0×10^{15} cm
l_z	1.5×10^{15} cm
n_r	400
n_z	300

Table B.1). The star is located at $(r_0, z_0) = (0, 0.3 \times 10^{15})$ cm and its spherical wind is introduced defining a circular injector with radius $r_{in} = 7 \times 10^{13}$ cm (14 cells). The jet is injected at the bottom boundary of the grid at $z = 1 \times 10^{13}$ cm. The upper and right boundaries of the grid are set to outflow, while the axis boundary is set to reflection.

The chosen physical parameters of the jet are the total luminosity $L = 4 \times 10^{37}$ erg s^{-1}, the Lorentz factor $\Gamma = 10$ (with $v_r = 0$ and $v_z = 0.995$ c), and the specific internal energy $\epsilon_{jet} = 9 \times 10^{18}$ erg g^{-1}. The derived jet density is $\rho_{jet} = 1.24 \times 10^{-27}$ g cm^{-3}. For the spherical stellar wind, the physical parameters are the mass-loss rate $\dot{M} = 10^{-9}$ $M_\odot$ yr^{-1}, the radial velocity $v_{sw} = 2000$ km s^{-1}, and the specific internal energy $\epsilon_{sw} = 9 \times 10^{13}$ erg g^{-1}. The derived stellar wind density is $\rho_{sw} = 5.12 \times 10^{-21}$ g cm^{-3}. The values of v_{sw}, ϵ_{sw} and ρ_{sw} are given at the injection surface at a distance r_{in} with respect to the star center. The grid was initially filled with the jet properties except at the stellar wind injection region, where it was filled with the stellar wind properties. The jet and stellar wind physical parameters are summarized in Table B.2.

The previous physical values lead to a jet-to-stellar wind thrust ratio of

$$\eta = \frac{F_{jet} S_{jet}}{F_{sw} S_{sw}} = \frac{\left(\rho_{jet} \Gamma^2 v_{jet}^2 h_{jet} + p_{jet}\right) S_{jet}}{\dot{M} v_{sw} + p_{sw} S_{sw}} \approx \frac{L}{\dot{M} v_{sw} c} \sim 100, \qquad \text{(B.1)}$$

Table B.2: Jet and stellar-wind physical parameters. Density ρ, specific internal energy ϵ, and velocity v at $z \leqslant 1 \times 10^{13}$ cm for the jet (boundary condition), and at a distance $r_{\text{in}} \leqslant 7 \times 10^{13}$ cm with respect to the star center located at $(r_0, z_0) = (0, 0.3 \times 10^{15})$ cm (boundary condition).

Parameter	Jet	Stellar wind
ρ	1.24×10^{-27} g cm^{-3}	5.12×10^{-21} g cm^{-3}
ϵ	9.0×10^{18} erg g^{-1}	9.0×10^{13} erg g^{-1}
v	0.995 c	2000 km s^{-1}

where $F_{\text{jet/sw}}$ is the momentum flux of the jet/stellar wind, S_{jet} the circular base of the jet of radius l_r, S_{sw} the spherical surface of the external boundary of the stellar injector, h_{jet} the specific enthalpy of the jet given by $h_{\text{jet}} = 1 + \frac{\epsilon_{\text{jet}}}{c^2} + \frac{p_{\text{jet}}}{\rho_{\text{jet}} c^2}$, and $p_{\text{jet/sw}}$ the pressure of the jet/stellar wind given by $p_{\text{jet/sw}} = (\gamma - 1)\, \rho_{\text{jet/sw}} \epsilon_{\text{jet/sw}}$. Therefore, from Eq. 6.3, the on-axis position (with respect to $z = 0$) where the jet and the stellar wind momentum fluxes are equal (i.e., the contact discontinuity location) is given by

$$z_{\text{CD}} = z_0 - \sqrt{\frac{1}{4\eta}}\, l_r = 0.2 \times 10^{15} \text{ cm}. \tag{B.2}$$

B.1.2 *Streamline calculations*

We computed the streamlines as it is described in Section 7. In addition, to the general procedure, we defined a streamline every 5 computational cells along the jet base placed at $z = 1 \times 10^{13}$ cm and $r \in [0, l_r]$. After a streamline was computed, we down-sampled the line into 200 equidistant cells, aimed to reduce the computing time of the radiative calculations.

B.1.3 *Results*

Figure B.1-*top* shows the density map and the computed streamlines for the jet-stellar wind simulation once the (quasi-)steady state (metastable state with periodic perturbations) is reached at $t = 3.3 \times 10^7$ s. The shock is bow-shaped towards the star, whose wind has a lower momentum rate, and the contact discontinuity is placed at $z_{\rm CD}^{\rm num} \sim 0.2 \times 10^{15}$ cm, as obtained with the analytical estimation from Eq. B.2. The shock structure presents some irregularities caused by possible numerical effects related to the axisymmetric nature of the simulation, and likely by the two-wind density and velocity contrasts due to the RT and KH instabilities, respectively (see Chandrasekhar 1961). Figure B.1-*bottom* shows the density map and the computed streamlines before reaching the (quasi-)steady state for $t = 4.3 \times 10^6$ s, at which time the perturbations have penetrated deep into the jet increasing the size of the stellar wind shocked region and modifying the streamline trajectory.

The development of instabilities imposed a limitation on the simulation parameters. A lighter and/or faster jet would enhance the development and growth of the perturbations due to RT and KH instabilities, respectively, and higher resolutions would enhance instabilities through the production of smaller and denser fragments of stellar wind material. Similar irregularities have been also found in relativistic 2D simulations in planar geometry (Bosch-Ramon et al. 2012; Lamberts et al. 2013), i.e. without reflecting boundary conditions and without the presence of a coordinate singularity, hence, attributed to a physical origin. In addition, we ran low-resolution 3D simulations (not presented here) focusing on the region close to the star, and we found that the shocked region was also presenting that waving structure. See Section 6 (and Paredes-Fortuny et al. 2015a) for an extended discussion on the instability origin in a relativistic axisymmetric simulation of a two-wind collision.

The results presented here have been used by our collaborators to compute the detailed radiative output from the simulated system. These have been published in the context of this thesis in de la Cita et al. (2016).

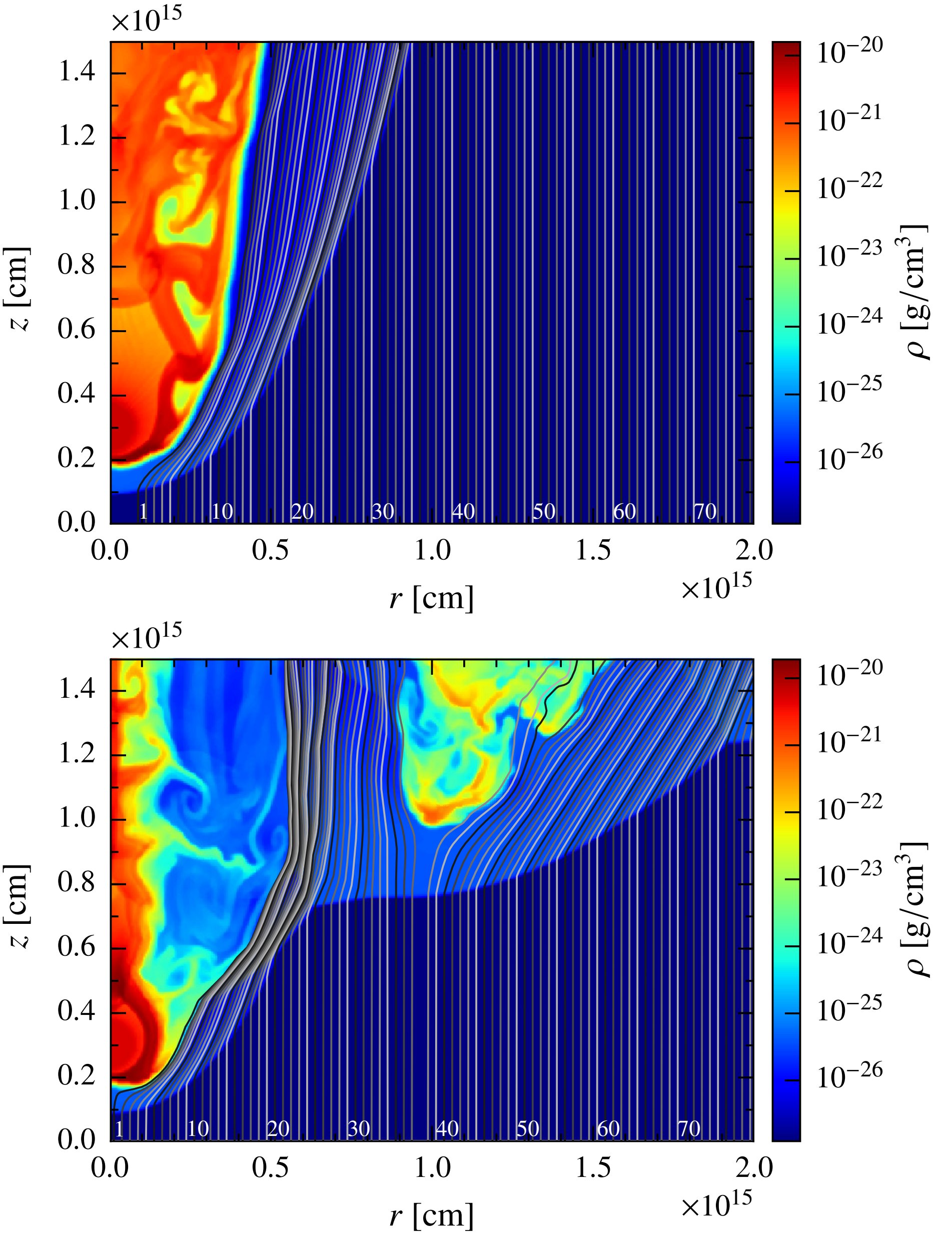

Figure B.1: Density distribution by color at time $t = 3.3 \times 10^7$ s (*top*) and $t = 4.3 \times 10^6$ s (*bottom*). The star is located at $(r_0, z_0) = (0, 0.3 \times 10^{15})$ cm and the jet is injected at $z < 1 \times 10^{13}$ cm. The gray lines show the computed streamline trajectories.

Table B.3: Simulation parameters. Polytropic index γ^{ad}, physical r grid size l_r, physical z grid size l_z, number of cells in the r axis n_r, and number of cells in the z axis n_z.

Parameter	Jet-obstacle simulation
γ^{ad}	$4/3$
l_r	0.8×10^{15} cm
l_z	1.5×10^{15} cm
n_r	160
n_z	300

B.2 SIMULATIONS OF A JET-OBSTACLE INTERACTION

B.2.1 *Numerical set-up*

We performed axisymmetric RHD simulations of the interaction of a relativistic jet and a very dense obstacle, to check the case of an obstacle with infinite inertia, using the same numerical code as in the jet-stellar wind simulations. We also adopted the same relativistic polytropic index of $\gamma = 4/3$. The physical size of the domain is $r \in [0, l_r]$, with $l_r = 0.8 \times 10^{15}$ cm, and $z \in [0, l_z]$, with $l_z = 1.5 \times 10^{15}$ cm. The adopted resolution is 160×300 cells (see Table B.3). The obstacle is located at $(r_0, z_0) = (0, 0.3 \times 10^{15})$ cm as the star in the former simulation, and its radius is $r_{\mathrm{ob}} = 1.4 \times 10^{14}$ cm. The jet injection and the boundary conditions are the same as in the previous simulation, while the obstacle is only set as an initial condition.

The chosen physical parameters of the jet are the same as in the jet-stellar wind simulation, except for the total luminosity which is set to $L = 6 \times 10^{36}$ erg s^{-1} (which is lower compared to the previous simulation due to a smaller jet base; the injected energy flux is the same). For the obstacle, the physical parameters are the density $\rho_{\mathrm{ob}} = 1.0 \times 10^{-18}$ g cm^{-3}, the radial velocity $v_{\mathrm{ob}} = 0$ km s^{-1}, and the

Table B.4: Jet and obstacle physical parameters. Density ρ, specific internal energy ϵ, and velocity v at $z \leqslant 1 \times 10^{13}$ cm for the jet (boundary condition), and at a distance $r_{\rm in} \leqslant 1.4 \times 10^{14}$ cm with respect to the obstacle center located at $(r_0, z_0) = (0, 0.3 \times 10^{15})$ cm, for the obstacle (as an initial condition only).

Parameter	Jet	Obstacle
ρ	1.24×10^{-27} g cm^{-3}	1.0×10^{-18} g cm^{-3}
ϵ	9.0×10^{18} erg g^{-1}	9.0×10^{12} erg g^{-1}
v	0.995 c	0 km s^{-1}

specific internal energy $\epsilon_{\rm ob} = 9 \times 10^{12}$ erg g^{-1}, where $\rho_{\rm ob}$, $v_{\rm ob}$ and $\epsilon_{\rm ob}$ are set at a distance $r_{\rm ob} \leqslant 1.4 \times 10^{14}$ cm with respect to the obstacle center. The grid was initially filled with the jet properties except at the obstacle region, where it was filled with the obstacle properties. The jet and obstacle physical parameters are summarized in Table B.4.

B.2.2 *Streamline calculations*

We computed the streamlines as it is described in Section 7. In addition, to the general procedure, we defined a streamline every 3 computational cells along the jet base placed at $z = 1 \times 10^{13}$ cm and $r \in [0, l_r]$. As in the previous simulations, we down-sampled each line into 200 equidistant cells, aimed to reduce the computing time of the radiative calculations.

B.2.3 *Results*

Figure B.2 shows the density map and the computed streamlines for the jet-obstacle simulation once the steady state is reached at $t = 1.0 \times 10^6$ s. The shock is bow-shaped towards the obstacle and presents a smooth structure compared to the jet-stellar wind simulation.

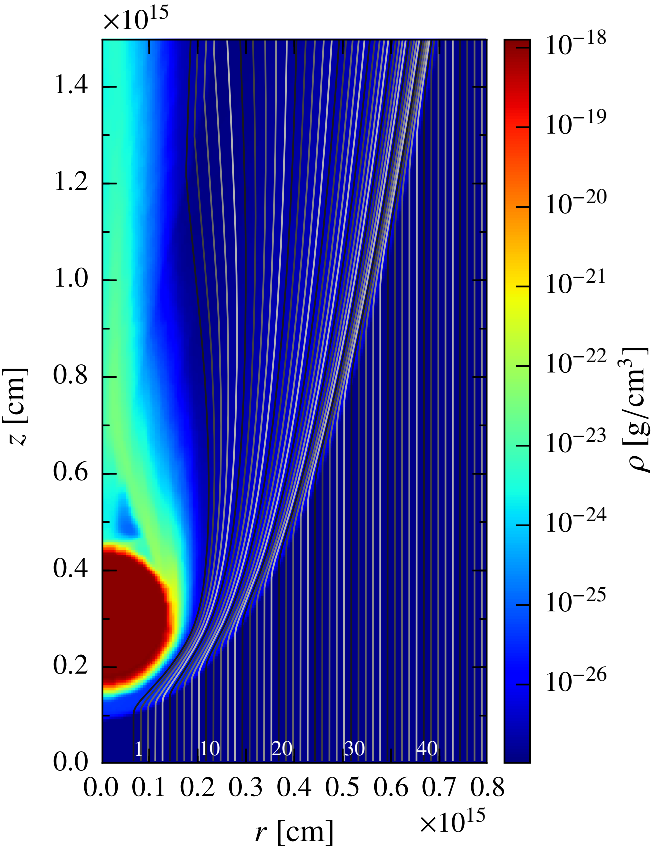

Figure B.2: Density distribution by color at time $t = 1.0 \times 10^6$ s. The obstacle is located at $(r_0, z_0) = (0, 0.3 \times 10^{15})$ cm and the jet is injected at $z < 1 \times 10^{13}$ cm. The gray lines show the computed streamline trajectories.

PUBLICATIONS

Directly related with this thesis

1. **Paredes-Fortuny X.**, Ribó M., Bosch-Ramon V., Casares J., Fors O., Núñez J., 2015, *Evidence of coupling between the thermal and nonthermal emission in the gamma-ray binary LS I +61 303*. A&A, 575, L6

2. **Paredes-Fortuny X.**, Bosch-Ramon V., Perucho M., Ribó M., 2015, *Simulations of an inhomogeneous stellar wind interacting with a pulsar wind in a binary system*. A&A, 574, A77

Non-directly related with this thesis

3. de la Cita V. M., Bosch-Ramon V., **Paredes-Fortuny X.**, Khangulyan D., Perucho M., 2016, *Coupling hydrodynamics and radiation calculations for star-jet interactions in AGN*. Accepted for publication in A&A (arXiv:1604.02070)

4. Martí J., Luque-Escamilla P. L., Casares J., Marcote B., **Paredes-Fortuny X.**, Ribó M., Paredes J. M., Núñez J., 2015, *In quest of nonthermal signatures in early-type stars*. Ap&SS, 356, 277

Conference proceedings

5. **Paredes-Fortuny, X.**, Ribó, M., Bosch-Ramon, V., del Ser Badia, D., Fors, O., Núñez, J., 2016, *Gamma-ray binaries and recent results on LS I +61 303*. Accepted for publication in PoS(MULTIF15)024

6. **Paredes-Fortuny, X.**, Bosch-Ramon, V., Perucho, M., Ribó, M., 2016, *Numerical simulations of the collision of an inhomogeneous stellar wind and a relativistic pulsar wind in a binary system*. Accepted for publication in Workshop Series of the Argentinian Astronomical Society.

7. **Paredes-Fortuny X.**, Ribó M., Fors O., Núñez J., Bosch-Ramon V., 2014, *Optical Photometric Monitoring of LS I +61 303*. IJMPS, 28, 1460197

8. **Paredes-Fortuny X.**, Ribó M., Fors O., Núñez J., 2012, *Optical photometric monitoring of gamma-ray binaries*. AIPC, 1505, 390

LIST OF FIGURES

Figure 1.1 *Fermi* five-year all-sky image 3
Figure 1.2 VHE all-sky map 4
Figure 2.1 Telescope Fabra-ROA Montsec (TFRM) 16
Figure 2.2 Liverpool Telescope 18
Figure 3.1 Flowchart of `Phot` 20
Figure 4.1 Optical photometric and $EW_{\mathrm{H}\alpha}$ light curves of LS I +61 303 plotted as a function of the MJD . . . 33
Figure 4.2 Optical photometric and $EW_{\mathrm{H}\alpha}$ light curves of LS I +61 303 (4 observational campaigns) 36
Figure 4.3 Optical photometry and $EW_{\mathrm{H}\alpha}$ of LS I +61 303 plotted as a function of the superorbital phase. . . 38
Figure 4.4 Color maps of the optical photometry and $EW_{\mathrm{H}\alpha}$ from LS I +61 303 as a function of the orbital phase and superorbital cycle 39
Figure 4.5 Optical photometry of LS I +61 303 plotted as a function of the superorbital phase for different orbital phase bins of 0.1 width 41
Figure 4.6 Binned optical photometric light curve plotted as a function of the orbital phase 43
Figure 4.7 Standard deviation of the optical photometry of the 0.1 width orbital phase bins 43
Figure 4.8 $EW_{\mathrm{H}\alpha}$ of LS I +61 303 plotted as a function of the superorbital phase for different orbital phase bins of 0.1 width 45
Figure 4.9 Binned $EW_{\mathrm{H}\alpha}$ plotted as a function of the orbital phase 47
Figure 4.10 Standard deviation of the $EW_{\mathrm{H}\alpha}$ of the 0.1 width orbital phase bins 47

Figure 4.11 Orbit of the compact object (black ellipse) around the star (black circle) 48
Figure 6.1 Cartoon representing a density map of the physical scenario 73
Figure 6.2 Density distribution by color of the (quasi)-steady state 80
Figure 6.3 Density distribution by color for the case with clump parameters $\chi = 10$ and $R_c = 1$ a 82
Figure 6.4 Density distribution by color for the case with clump parameters $\chi = 10$ and $R_c = 2.5$ a 83
Figure 6.5 Density distribution by color for the case with clump parameters $\chi = 10$ and $R_c = 5$ a 84
Figure 6.6 Density distribution by color for the case with clump parameters $\chi = 30$ and $R_c = 1$ a 85
Figure 6.7 Zoom-in of the density distribution by color for the case with clump parameters $\chi = 10$ and $R_c = 2.5$ a 87
Figure 6.8 Tracer distribution by color for the case with clump parameters $\chi = 10$ and $R_c = 2.5$ a 88
Figure 6.9 Pressure distribution in units of $\rho_0 c^2$ by color for the case with clump parameters $\chi = 10$ and $R_c = 2.5$ a 89
Figure 6.10 Momentum flux over pressure distribution by color for the case with clump parameters $\chi = 10$ and $R_c = 2.5$ a 90
Figure 6.11 β distribution by color for the case with clump parameters $\chi = 10$ and $R_c = 2.5$ a 91
Figure 6.12 Density distribution by color at time $t = 25000$ s for the simulation with a resolution of 300×500 cells 93
Figure 6.13 Density distribution by color for the case with clump parameters $\chi = 10$ and $R_c = 2.5$ a and a resolution of 225×375 cells 94
Figure 7.1 Density distribution by color in the (quasi)-steady state 104

Figure 7.2 Density distribution by color considering an inhomogeneous stellar wind with $\chi = 10$ and $R_c = 8 \times 10^{10}$ cm . . . 105
Figure A.1 Optical photometric light curve of MWC656 folded with the orbital period . . . 116
Figure A.2 Optical photometric light curve of MWC 148 folded with the orbital period . . . 117
Figure A.3 Optical photometric light curve of TYC 4051-1277-1 as a function of the MJD . . . 119
Figure A.4 Optical photometric light curve of TYC 3594-2269-1 as a function of the MJD . . . 119
Figure A.5 Optical photometric light curve of PSR J1023+0038 folded with the orbital period . . . 120
Figure B.1 Density distribution by color (star) . . . 125
Figure B.2 Density distribution by color (obstacle) . . . 128

LIST OF TABLES

Table 1.1 System parameters of gamma-ray binaries 5
Table 4.1 Fitted sinusoidal parameters to the orbital modulation of the optical photometry and the $EW_{H\alpha}$ of LS I +61 303 34
Table 4.2 Fitted parameters to the superorbital modulation of the optical photometry for 10 orbital phase bins 42
Table 4.3 Fitted sinusoidal parameters to the superorbital modulation of the $EW_{H\alpha}$ of LS I +61 303 for 10 orbital phase bins 46
Table 6.1 Simulation parameters 77
Table 6.2 Pulsar and stellar parameters 78
Table 6.3 Clump impact on the size of the two-wind interaction region 96
Table B.1 Simulation parameters (jet-stellar wind simulation) 122
Table B.2 Jet and stellar-wind physical parameters 123
Table B.3 Simulation parameters (jet-obstacle simulation) . . 126
Table B.4 Jet and obstacle physical parameters 127

ACRONYMS

AGILE	*Astro-Rivelatore Gamma a Immagini LEggero*
AGN	Active Galactic Nucleus
c.l.	confidence level
CCD	Charge-Coupled Device
CTA	Cherenkov Telescope Array
EW	Equivalent Width
$EW_{\mathrm{H}\alpha}$	Equivalent Width of the Hα line
Fermi	*Fermi Gamma-ray Space Telescope*
`FITS`	Flexible Image Transport System
FOV	Field of View
HAWC	The High-Altitude Water Cherenkov Observatory
HE	High Energy
H.E.S.S.	High Energy Stereoscopic System
IACT	Imaging Atmospheric Cherenkov Telescope
IC	Inverse Compton
KH	Kelvin-Helmholtz

LAT	Large Area Telescope
LT	Liverpool Telescope
MAGIC	Major Atmospheric Gamma Imaging Cherenkov Telescopes
OpenMP	Open Message Passing
PDM	Phase Dispersion Minimization
PWN	Pulsar Wind Nebula
RHD	Relativistic Hydrodynamics
RT	Rayleigh-Taylor
SNR	Supernova Remnant
TFRM	Telescope Fabra-ROA Montsec
VERITAS	Very Energetic Radiation Imaging Telescope Array System
VHE	Very High Energy
WCS	World Coordinate System

BIBLIOGRAPHY

Abdo, A. A., Ackermann, M., Ajello, M., et al. 2011, ApJ, 736, L11

Abdo, A. A., Ackermann, M., Ajello, M., et al. 2009, ApJ, 701, L123

Abeysekara, A. U., Alfaro, R., Alvarez, C., et al. 2013, Astroparticle Physics, 50, 26

Acharya, B. S., Actis, M., Aghajani, T., et al. 2013, Astroparticle Physics, 43, 3

Ackermann, M., Ajello, M., Ballet, J., et al. 2013, ApJ, 773, L35

Aharonian, F. A., Akhperjanian, A. G., Bazer-Bachi, A. R., et al. 2007, A&A, 469, L1

Aharonian, F. A., Bogovalov, S. V., & Khangulyan, D. 2012, Nature, 482, 507

Albert, J., Aliu, E., Anderhub, H., et al. 2009, ApJ, 693, 303

Aloy, M. A. 1999, PhD thesis, Universitat de València

Anderhub, H., Antonelli, L. A., Antoranz, P., et al. 2009, ApJ, 706, L27

Aragona, C., McSwain, M. V., Grundstrom, E. D., et al. 2009, ApJ, 698, 514

Archibald, A. M., Stairs, I. H., Ransom, S. M., et al. 2009, Science, 324, 1411

Astropy Collaboration, Robitaille, T. P., Tollerud, E. J., et al. 2013, A&A, 558, A33

Atwood, W. B., Abdo, A. A., Ackermann, M., et al. 2009, ApJ, 697, 1071

Bertin, E. & Arnouts, S. 1996, A&AS, 117, 393

Bogdanov, S., Archibald, A. M., Bassa, C., et al. 2015, ApJ, 806, 148

Bogovalov, S. V., Khangulyan, D., Koldoba, A. V., Ustyugova, G. V., & Aharonian, F. A. 2012, MNRAS, 419, 3426

Bogovalov, S. V., Khangulyan, D. V., Koldoba, A. V., Ustyugova, G. V., & Aharonian, F. A. 2008, MNRAS, 387, 63

Bongiorno, S. D., Falcone, A. D., Stroh, M., et al. 2011, ApJ, 737, L11

Bosch-Ramon, V. 2013, A&A, 560, A32

Bosch-Ramon, V., Barkov, M. V., Khangulyan, D., & Perucho, M. 2012, A&A, 544, A59

Bosch-Ramon, V., Barkov, M. V., & Perucho, M. 2015, A&A, 577, A89

Bosch-Ramon, V. & Khangulyan, D. 2009, International Journal of Modern Physics D, 18, 347

Bosch-Ramon, V., Paredes, J. M., Ribó, M., et al. 2005, ApJ, 628, 388

Broeg, C., Fernández, M., & Neuhäuser, R. 2005, AN, 326, 134

Cañellas, A., Joshi, B. C., Paredes, J. M., et al. 2012, A&A, 543, A122

Casares, J., Negueruela, I., Ribó, M., et al. 2014, Nature, 505, 378

Casares, J., Ribas, I., Paredes, J. M., Martí, J., & Allende Prieto, C. 2005, MNRAS, 360, 1105

Casares, J., Ribó, M., Ribas, I., et al. 2012, MNRAS, 421, 1103

Chandrasekhar, S. 1961, Hydrodynamic and hydromagnetic stability

Chernyakova, M., Abdo, A. A., Neronov, A., et al. 2014, MNRAS, 439, 432

Chernyakova, M., Neronov, A., Molkov, S., et al. 2012, ApJ, 747, L29

Cranmer, S. R. & Owocki, S. P. 1996, ApJ, 462, 469

de la Cita, V. M., Bosch-Ramon, V., Paredes-Fortuny, X., Khangulyan, D., & Perucho, M. 2016, ArXiv: 1604.02070

Dhawan, V., Mioduszewski, A., & Rupen, M. 2006, in VI Microquasar Workshop: Microquasars and Beyond

Donat, R., Font, J. A., Ibáñez, J. M., & Marquina, A. 1998, Journal of Computational Physics, 146, 58

Donat, R. & Marquina, A. 1996, Journal of Computational Physics, 125, 42

Dubus, G. 2013, A&A Rev., 21, 64

Dubus, G. & Cerutti, B. 2013, A&A, 557, A127

Font, J. A., Ibanez, J. M., Marquina, A., & Marti, J. M. 1994, A&A, 282, 304

Fors, O., Núñez, J., Muiños, J. L., et al. 2013, PASP, 125, 522

Frail, D. A. & Hjellming, R. M. 1991, AJ, 101, 2126

Gregory, P. C. 2002, ApJ, 575, 427

Gregory, P. C. & Taylor, A. R. 1978, Nature, 272, 704

Gregory, P. C., Taylor, A. R., Crampton, D., et al. 1979, AJ, 84, 1030

Gregory, P. C., Xu, H.-J., Backhouse, C. J., & Reid, A. 1989, ApJ, 339, 1054

Grundstrom, E. D., Caballero-Nieves, S. M., Gies, D. R., et al. 2007, ApJ, 656, 437

Halpern, J. P., Gaidos, E., Sheffield, A., Price-Whelan, A. M., & Bogdanov, S. 2013, The Astronomer's Telegram, 5514

Hanuschik, R. W. 1996, A&A, 308, 170

Hutchings, J. B. & Crampton, D. 1981, PASP, 93, 486

Kaper, L., Henrichs, H. F., Fullerton, A. W., et al. 1997, A&A, 327, 281

Khangulyan, D., Aharonian, F. A., Bogovalov, S. V., & Ribó, M. 2012, ApJ, 752, L17

Khangulyan, D., Bogovalov, S. V., & Aharonian, F. A. 2014, International Journal of Modern Physics Conference Series, 28, 60169

Lamberts, A., Dubus, G., Fromang, S., & Lesur, G. 2012a, in American Institute of Physics Conference Series, Vol. 1505, American Institute of Physics Conference Series, ed. F. A. Aharonian, W. Hofmann, & F. M. Rieger, 406–409

Lamberts, A., Dubus, G., Lesur, G., & Fromang, S. 2012b, A&A, 546, A60

Lamberts, A., Fromang, S., Dubus, G., & Teyssier, R. 2013, A&A, 560, A79

Landolt, A. U. 1992, AJ, 104, 340

Lang, D., Hogg, D. W., Mierle, K., Blanton, M., & Roweis, S. 2010, AJ, 139, 1782

Li, J., Torres, D. F., Zhang, S., et al. 2011, ApJ, 733, 89

Li, J., Torres, D. F., Zhang, S., et al. 2012, ApJ, 744, L13

Lobel, A. 2008, in Clumping in Hot-Star Winds, ed. W.-R. Hamann, A. Feldmeier, & L. M. Oskinova, 81

Longair, M. S. 2011, High Energy Astrophysics (Cambridge University Press)

Lucarelli, F., Verrecchia, F., Striani, E., et al. 2010, The Astronomer's Telegram, 2761

Lucy, L. B. & Solomon, P. M. 1970, ApJ, 159, 879

MAGIC Collaboration, Ahnen, M. L., Ansoldi, S., et al. 2016, ArXiv e-prints

Marcote, B., Ribó, M., Paredes, J. M., et al. 2016, MNRAS, 456, 1791

Martí, J., Luque-Escamilla, P. L., Casares, J., et al. 2015, Ap&SS, 356, 277

Martí, J. M. & Müller, E. 2003, Living Reviews in Relativity, 6, 7

Martí, J. M., Müller, E., Font, J. A., Ibáñez, J. M., & Marquina, A. 1997, ApJ, 479, 151

Martí, J. M. & Müller, E. 1996, Journal of Computational Physics, 123, 1

Massi, M., Ribó, M., Paredes, J. M., et al. 2004, A&A, 414, L1

Massi, M., Ribó, M., Paredes, J. M., Peracaula, M., & Estalella, R. 2001, A&A, 376, 217

Massi, M. & Torricelli-Ciamponi, G. 2016, A&A, 585, A123

McSwain, M. V., Ray, P. S., Ransom, S. M., et al. 2011, ApJ, 738, 105

Mendelson, H. & Mazeh, T. 1989, MNRAS, 239, 733

Mignone, A., Plewa, T., & Bodo, G. 2005, ApJS, 160, 199

Mirabel, I. F. 2012, Science, 335, 175

Moffat, A. F. J. 2008, in Clumping in Hot-Star Winds, ed. W.-R. Hamann, A. Feldmeier, & L. M. Oskinova, 17

Moldón, J. 2012, PhD thesis, Universitat de Barcelona

Negueruela, I., Reig, P., Coe, M. J., & Fabregat, J. 1998, A&A, 336, 251

Okazaki, A. T. 2001, PASJ, 53, 119

Okazaki, A. T., Nagataki, S., Naito, T., et al. 2011, PASJ, 63, 893

Paredes, J. M. 1987, PhD thesis, University of Barcelona, (1987) Paredes, J. M., Bednarek, W., Bordas, P., et al. 2013, Astroparticle Physics, 43, 301

Paredes, J. M. & Figueras, F. 1986, A&A, 154, L30

Paredes, J. M., Marti, J., Peracaula, M., & Ribó, M. 1997, A&A, 320, L25

Paredes, J. M., Marziani, P., Marti, J., et al. 1994, A&A, 288, 519

Paredes, J. M., Ribó, M., Bosch-Ramon, V., et al. 2007, ApJ, 664, L39

Paredes-Fortuny, X., Bosch-Ramon, V., Perucho, M., & Ribó, M. 2015a, A&A, 574, A77

Paredes-Fortuny, X., Ribó, M., Bosch-Ramon, V., et al. 2015b, A&A, 575, L6

Paredes-Fortuny, X., Ribó, M., Fors, O., & Núñez, J. 2012, in American Institute of Physics Conference Series, Vol. 1505, American Institute of Physics Conference Series, ed. F. A. Aharonian, W. Hofmann, & F. M. Rieger, 390–393

Paredes-Fortuny, X., Ribó, M., Fors, O., Núñez, J., & Bosch-Ramon, V. 2014, International Journal of Modern Physics Conference Series, 28, 60197

Perucho, M. 2005, PhD thesis, Universitat de València (Spain

Perucho, M. & Bosch-Ramon, V. 2012, A&A, 539, A57

Pittard, J. M. 2007, ApJ, 660, L141

Press, W. H., Teukolsky, S. A., Vetterling, W. T., & Flannery, B. P. 1992, Numerical recipes in Fortran 77. The art of scientific computing, 2nd edn. (Cambridge University Press)

Rea, N., Torres, D. F., van der Klis, M., et al. 2010, MNRAS, 405, 2206

Rieger, F. M., de Oña-Wilhelmi, E., & Aharonian, F. A. 2013, Frontiers of Physics, 8, 714

Rivinius, T., Carciofi, A. C., & Martayan, C. 2013, A&A Rev., 21, 69

Roberts, D. H., Lehar, J., & Dreher, J. W. 1987, AJ, 93, 968

Romero, G. E., Okazaki, A. T., Orellana, M., & Owocki, S. P. 2007, A&A, 474, 15

Runacres, M. C. & Owocki, S. P. 2002, A&A, 381, 1015

Saha, L., Chitnis, V. R., Shukla, A., Rao, A. R., & Acharya, B. S. 2016, ArXiv e-prints

Smith, A., Kaaret, P., Holder, J., et al. 2009, ApJ, 693, 1621

Stappers, B. W., Archibald, A. M., Hessels, J. W. T., et al. 2014, ApJ, 790, 39

Stellingwerf, R. F. 1978, ApJ, 224, 953

Takahashi, T., Kishishita, T., Uchiyama, Y., et al. 2009, ApJ, 697, 592

Takata, J., Okazaki, A. T., Nagataki, S., et al. 2012, ApJ, 750, 70

Tavani, M., Barbiellini, G., Argan, A., et al. 2009, A&A, 502, 995

Taylor, A. R. & Gregory, P. C. 1982, ApJ, 255, 210

Toro, E. F. 1999, Riemann Solvers and Numerical Methods for Fluid Dynamics (Springer)

Williams, S. J., Gies, D. R., Matson, R. A., et al. 2010, ApJ, 723, L93

Woodward, P. & Colella, P. 1984, Journal of Computational Physics, 54, 115

Zabalza, V., Paredes, J. M., & Bosch-Ramon, V. 2011, A&A, 527, A9

Zaitseva, G. V. & Borisov, G. V. 2003, Astronomy Letters, 29, 188

Zamanov, R., Martí, J., Stoyanov, K., Borissova, A., & Tomov, N. A. 2014, A&A, 561, L2

Zamanov, R., Stoyanov, K., Martí, J., et al. 2013, A&A, 559, A87

Zamanov, R. K., Martí, J., Paredes, J. M., et al. 1999, A&A, 351, 543

COLOPHON

This document was typeset using the typographical look-and-feel `classicthesis` developed by André Miede. The style was inspired by Robert Bringhurst's seminal book on typography *"The Elements of Typographic Style"*.

ACKNOWLEDGEMENT OF FUNDING

The author acknowledges support by the Spanish Ministerio de Economía y Competitividad (MINECO) under grants FPA2010-22056-C06-02, AYA2013-47447-C3-1-P, and MDM-2014-0369 of ICCUB (Unidad de Excelencia 'María de Maeztu'). This work has been supported by the Marie Curie Career Integration Grant 321520. The author also acknowledges financial support from Universitat de Barcelona and Generalitat de Catalunya under grants APIF and FI (2014FI_B 01017), respectively.